The Modeling of Laminar-to-turbulent Transition for Unsteady Integral Boundary Layer Equations with High-order Discontinuous Galerkin Method

Boyi Ye

Master of Science Thesis

TU Delft Delft University of Technology

The Modeling of Laminar-to-turbulent Transition for Unsteady Integral Boundary Layer Equations with High-order Discontinuous Galerkin Method

Master of Science Thesis

For the degree of Master of Science in Applied Mathematics at Delft University of Technology

Boyi Ye

May 27, 2015

Faculty of Electrical Engineering, Mathematics and Computer Science (EEMCS) · Delft University of Technology

The work in this thesis was done at Energy research Centre of the Netherlands (ECN).

Delft University of Technology
Department of
Applied Mathematics

The undersigned hereby certify that they have read and recommend to the Faculty of Electrical Engineering, Mathematics and Computer Science (EEMCS) for acceptance a thesis entitled

The Modeling of Laminar-to-turbulent Transition for Unsteady Integral Boundary Layer Equations with High-order Discontinuous Galerkin Method

by

Boyi Ye

in partial fulfillment of the requirements for the degree of

Master of Science Applied Mathematics

Dated: May 27, 2015

Supervisor(s):

Dr. H. Özdemir

Dr.ir. D.R. van der Heul

Reader(s):

Prof.dr.ir. C. Vuik

Dr. J.L.A. Dubbeldam

Acknowledgements

This thesis would not have been possible without the support of many people. First of all, I would like to acknowledge my supervisor at ECN, Dr. Huseyin Özdemir for your kindness and all the inspiring ideas during each of our meetings. Your tolerance and patience which allow me doing all those "nonsense" work at a first glance enables me to obtain so much knowledge not only on the topic of this thesis, but more importantly also the whole world of computational fluid dynamics. I would also like to thank my daily supervisor at TU Delft, Dr.ir. D.R. van der Heul, your carefulness and critical points of view help me avoid so many mistakes in my work, and more importantly let me know how a scientific researcher should treat his work. I would thank Prof.dr.ir. C. Vuik and Prof.dr. R. Nabben at TU Berlin for recommending me into the awesome Erasmus Mundus COSSE programme. It has been the most colorful and rewarding two and a half years in my life. Of course, I should not forget all those young and funny guys working in the wind energy unit at ECN, without them, I can hardly imagine to survive for seventeen months in a place two kilometers away from the nearest village. Finally, it is for my parents, as a person who always appears to be happy and positive as I am, you are the only ones I can talk to when I am down and blue.

(after missing the bus and have to wait for another one hour)
Boyi Ye at ECN, Petten

Contents

List of Figures

List of Tables

Chapter 1

Introduction

1.1 Background

With the fast development of the modern world we are living in, the need for energy is growing rapidly. Due to the fact that the traditional sources of energy, i.e. fossil fuels, are nonrenewable, developing new kinds of energy is of great importance. Wind energy, as one of these, is often called "green energy" because of its renewability and environmentally friendliness. Europe has been acting as a pioneer in the wind energy development for decades. The Energy research Center of the Netherlands (ECN) Wind Energy Unit is one of the main contributors to wind energy research in Europe.

Generally, large wind turbines are used to convert the mechanical energy of the wind into electric energy we can use. Designing "aerodynamically optimal" wind turbines to make the transformation of energy more efficient is no doubt one of the biggest challenges of wind energy research. This requires accurate modeling of the flow on the blades and in the wake of the wind turbine rotor. If better aerodynamic models are available during the design phase, technological improvements can be achieved that will affect the performance, control, production and maintenance during the entire life cycle of the turbine.

The challenges of designing larger rotors and dealing with multiple turbines require more accurate prediction of loading on blades and wake generation. *Unsteady aerodynamics* plays an inportant role in both problems. This includes the changing inflow conditions due to incident wakes, the effects on instantaneous blade loading conditions, and time history effects from the wake (such as dynamic stall). Therefore, it is of great importance and interest to get an insight in *unsteady flow*, in which the fluid properties at a point may change over time. Furthermore, unsteady flow solvers for engineering applications are rare, and computationally intensive.

ECN is currently developing an efficient aerodynamic flow solver for simulating the

unsteady flow over wind turbine blades. The model is based on a*viscous-inviscid splitting method*, which subdivides the flow region in a viscous part (*boundary layer*) and an inviscid part, with an implementation of a newly developed and very efficient *viscous-inviscid interation scheme* and using a high-order *Discontinuous Galerkin method* for discretisation in the viscous region. Many people have already contributed to this project including Seubers[43], Haciahmetoglu[23], van den Boogaard[48], and van Es[49], but up till now, only the model for laminar unsteady boundary layers is fully developed and implemented within the Discontinuous Galerkin framework.
This project will focus on extending the existing model for laminar boundary layers to turbulent boundary layers and more importantly to include the modeling of *transition* to turbulence in unsteady boundary layers. Successful prediction of *transition onset* and the flow inside the *transition region* would greatly help in improving the design of wind turbine blades.

1.2 Outline

The outline of this thesis is as follows:

- Chapter 2 starts with the introduction of the flow models. The reason for splitting the flow domain into a viscous boundary layer and an inviscid outer region is motivated. The governing equations are presented. The viscous flow model, including the boundary layer theory and the integral boundary layer equations are explained. In the second part, the integral boundary layer systems for both laminar and turbulent boundary layers are introduced. For turbulent boundary layers, two different integral boundary layer methods: the dissipation integral method and the entrainment integral method are presented in detail. In particular, for *non-equilibrium flows* which are strongly dependent on upstream history (e.g. *separated boundary layers*), an *unsteady shear-lag equation* is introduced and added to the system.

- Chapter 3 focuses on modeling of laminar-to-turbulent transition. The theoretical background of transition is explained. Two kinds of transition, *natural transition* and *bypass transition* are studied. The *simplified e^N method* based on the *linear stability theory* is introduced to model the onset of natural transition in steady boundary layers. It is then extended to model bypass transition as well as boundary layers with varying pressure gradient and free-stream turbulence level. The *intermittency model* for predicting the flow inside the transition region is also studied. Finally, the simplified e^N method for predicting transiton onset in unsteady flow is derived.

- The *space-time Discontinuous Galerkin method*, which is used to discretize the integral boundary layer equations is introduced in Chapter 4. Gaussian quadrature rules and Newton's method are used for the numerical integration and to solve the system of equations, respectively.
- Results of test cases for both fully turbulent boundary boundary layers and transitional boundary layers (steady and unsteady) are presented and discussed in Chapter 5.
- In Chapter 6 conclusions and recommendations for future work are given.

1.2.1 Main contributions of the present work

With respect to the modeling of turbulent boundary layers:

- Two integral boundary layer methods: the dissipation integral method and the entrainment integral method are studied and implemented.
- The closure relations for turbulent boundary layers are improved with small corrections.
- The unsteady shear-lag equation is re-derived and improvements are made to its formulation.
- A switch mechanism is designed to make the flow solver able to switch from an equilibrium model to a non-equilibrium model when the flow in the boundary layers approaches separation.

and with respect to the modeling of laminar-to-turbulent transition:

- A new correlation for the *critical momentum thickness Reynolds number* $Re_{\theta crit}$ is given.
- The simplified e^N method is extended based on Drela[13] to make it be able to predict onset of bypass transition. A new empirical relation for momentum thickness Reynolds number at transition onset $Re_{\theta onset}$ is given.
- The simplified e^N method is further extended and an effective free-stream turbulence level is defined so that the present model can treat varying free-stream turbulence level in the flow region.
- An intermittency model for predicting the length of transition regions is given and improvement is made for the correlations of two parameters used in the model.
- The unsteady simplified e^N method is derived and tested.

Chapter 2

Boundary layer modeling

2.1 Overview

Since the introduction of the Navier-Stokes (N-S) equations in the 1840s, traditional models of fluids have been mostly based on that set of partial differential equations (PDEs). However, although pursued by many great researchers, analytical solutions are still only known for a limited number of simple cases. Under that circumstance, numerical methods are developed to approximate the solutions of the N-S equations to get an insight in the dynamics of fluids. Due to the complexity thereof, for example in the case of turbulence, where the behavior of the flow is highly chaotic, discretisation with a very high resolution and huge amounts of simulation time are required to get an acceptable numerical solution. However, in engineering applications, e.g. the design of wind turbines, such requirements on computational resources can hardly be met. In order to decrease the computational intensity of these models and meet real world needs, researchers have made much effort to simplify the full N-S equations to come to simplified models that can be incorporated in fast and less computationally demanding design tools.

Current design tools for rotor aerodynamics are mainly based on the Blade Element-Momentum (BEM) approach which combines both blade element theory and momentum theory (see Kulunk[29] for details). The advantage of these methods is that they provide quick and efficient estimation of flow parameters. However, the range of applicability is limited, which means the approach is only applicable to simulate steady state, yaw aligned uniform flow, quasi-two-dimensional blade aerodynamics and spanwise independent induction without rotor cone angle. Although some empirical correlations can be applied to overcome those limitations and improve the model for some situations, the predictive confidence is still not satisfactory especially when load oscillations, dynamic stall, wake interference etc. have a profound influence

on the design [43].

Other approaches, such as the nonlinear lifting line method[50] which is based on non-linear lifting line vortex wake theory use less strict assumptions and can predict the influence of physical phenomena such as unsteadiness intrinsically, i.e. without using empirical corrections. Hence they can be applied to a wider range of rotor operating conditions. They are much faster than commercial computational fluid dynamics (CFD) software packages that solve for the entire flow field using low order Finite Volume Methods (FVM). This speedup is necessary in order to be able to make several design iterations in the process of optimizing turbine blades in a short time. However some physical information is lost due to the approximations and assumptions present in these engineering methods.

The viscous-inviscid splitting method is more accurate than the methods mentioned above because it includes a more complete model of the physics than the potential flow based models, but still maintains a reasonable computational time for design purposes. In 1904, Prandtl described the existence of the boundary layer [40]. He splits the flow field into a viscous inner layer (boundary layer) near the surface of the body dominated by viscous forces and creating the majority of drag on the surface of the body and an inviscid outer layer where inertia forces are dominant over viscous forces. The distinction is of great use since the Navier-Stokes equations can be significantly simplified in both regions, though in a different way (i.e. different flow models), due to the different characters of the two. So called *viscous-inviscid interaction schemes* can be used to couple the solutions in the two regions. Because of its efficiency and accuracy, the viscous-inviscid splitting method is used in the ECN in-house developed code for simulating the unsteady flow over wind turbine blades in the design phase.

The main aim of the present study is extending the modeling in boundary layers. A panel method for the inviscid region has been developed in ECN and details can be found in van Garrel[51]. Other contributions including the study of viscous-inviscid interaction schemes and numerical methods can be found in Haciahmetoglu[23] and Seubers[43]. The laminar boundary layer model is developed by van den Boogaard[48]. The present study therefore focuses on developing the turbulent and laminar-to-turbulent transition models fitting in the framework of ECN. For a more extensive discussion of the theoretical background of the boundary layer equations, please refer to the literature survey report of the present work[61].

2.2 Integral boundary layer equations

The fluid flow we are investigating can be considered as a continuous medium when the Knudsen number $K_n \gg 1$. The continuous model for fluid flow consists of three conservation laws: the conservation of mass, the conservation of momentum and the

conservation of energy. The equations in integral form are given as:

$$\frac{\partial}{\partial t}\int_V \rho dV + \int_S \rho \mathbf{u}\cdot d\mathbf{S} = 0, \tag{2.1a}$$

$$\frac{\partial}{\partial t}\int_V \mathbf{u} dV + \int_S (\rho\mathbf{u})\mathbf{u}\cdot d\mathbf{S} = \int_V \rho\mathbf{F} dv + \int_S \mathbf{P} dS, \tag{2.1b}$$

$$\frac{\partial}{\partial t}\int_V \rho E dV = \int_V \rho\mathbf{F}\cdot\mathbf{u} dV - \int_S \mathbf{P}\cdot\mathbf{u} dS - \int_S \rho E\mathbf{u}\cdot d\mathbf{S} + \int_V \rho q dV + W, \tag{2.1c}$$

where ρ is the density, $\mathbf{u}$ is the velocity vector, $\mathbf{F}$ is the body force, $\mathbf{P}$ is the surface force, $E = e + \frac{1}{2}u^2$ is the total energy, q is the volumetric rate of heat addition per unit mass and W is the viscous dissipation term, respectively. Recall that the present work mainly focuses on flows over wind turbines which are usually low speed (Mach number $M < 0.3$), the flow can be considered incompressible and the mass conservation equation reduces to the solenoidality constraint on the velocity field. If we further assume the density ρ to be constant, the governing equations can be written in tensor notation as:

$$\frac{\partial u_i}{\partial x_i} = 0, \tag{2.2a}$$

$$\frac{\partial u_i}{\partial t} + u_j\frac{\partial u_i}{\partial x_j} = \frac{\partial \sigma_{ij}}{\partial x_j} + \rho F_i, \tag{2.2b}$$

$$\frac{\partial E}{\partial t} + \frac{\partial u_i E}{\partial x_i} = \frac{\partial u_i\sigma_{ij}}{\partial x_j} + \rho u_i F_i - \frac{\partial q_i}{\partial x_i}, \tag{2.2c}$$

with

$$\text{total stress tensor:} \quad \sigma_{ij} = -P\delta_{ij} + \tau_{ij},$$

$$\text{viscous stress tensor:} \quad \tau_{ij} = \mu\left(\frac{\partial u_i}{\partial x_j} + \frac{\partial u_j}{\partial x_i}\right),$$

where μ is the dynamic viscosity.

We introduce the Reynolds number Re as a a non-dimensional quantity that denotes the ratio of inertial forces to viscous forces and consequently quantifies the relative importance of these two types of forces for given flow conditions.:

$$Re = \frac{\rho\mathbf{u}L}{\mu} = \frac{\mathbf{u}L}{\nu}, \tag{2.3}$$

where L is a characteristic linear dimension and ν is the kinematic viscosity, $\nu = \frac{\mu}{\rho}$.

When Re is very large (the inertial forces are dominating the viscous forces), applying dimensional analysis to the full N-S equations leads to the appearance of a factor of $1/Re$ as a coefficient of the viscous terms. It would seem that the viscous terms might be negligible. However, discarding those terms would lead to the inviscid flow equations which are obviously not applicable, because the solution would not be able to comply with the imposed boundary conditions. As mentioned before, Prandtl introduces the boundary layer theory where he states that the viscous effects would be confined to a very thin but non-negligible layer along a solid surface, namely the boundary layer, in the case where Re is large. The thickness of the boundary layer can be denoted by δ, which is defined as the distance from the wall where the magnitude of the velocity inside the boundary layer as attained a certain fraction of the external inviscid velocity. In principle the value is arbitrary but it is typically chosen as 99% which means the boundary layer stretches out in normal direction until the tangential velocity in the boundary layer reaches 99% of the outside velocity. See Figure 2-1 for an example of the boundary layer.

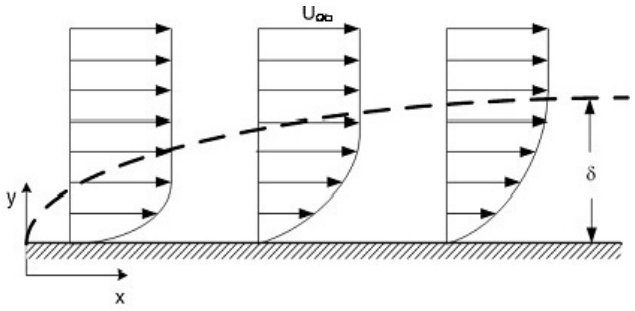

Figure 2-1: The boundary layer on a flate plate and the definition of the boundary layer thickness.

The displacement thickness δ^* is another important parameter of the boundary layer. It denotes the distance the wall needs to be displaced to obtain a similar "inviscid" flow rate. We have:

$$\int_0^{\delta} u dy = \int_0^{\delta^*} 0 dy + \int_{\delta^*}^{\delta} u_e dy = u_e(\delta - \delta^*) = \int_0^{\delta} u_e dy - u_e \delta^*, \tag{2.4}$$

where u_e is the edge velocity of the boundary layer. Thus:

$$\delta^* = \int_0^{\delta} \left(1 - \frac{u}{u_e}\right) dy. \tag{2.5}$$

Note that for the present work, in order to simplify the model, nonzero surface curvature is not taken into consideration. Thus, the edge velocity is equal to the free-stream

velocity:

$$u_e = U_\infty \tag{2.6}$$

and thus the upper limit of the integral can be extended to ∞:

$$\delta^* = \int_0^\infty \left(1 - \frac{u}{u_e}\right) dy. \tag{2.7}$$

Another important parameter is the momentum thickness θ. It is defined as the additional thickness (on top of the displacement thickness) needed for the outside flow to incorporate the same amount of linear momentum as present in the boundary layer. The momentum thickness can be found from:

$$\theta = \int_0^\infty \frac{u}{u_e}\left(1 - \frac{u}{u_e}\right) dy. \tag{2.8}$$

Although the boundary layer only occupies a very small portion of the flow domain, it cannot be simply neglected since all mass, momentum and heat transfer to and from the flow domain boundary must take place through this boundary layer. This concept is exploited by applying viscous-inviscid splitting methods: Different simplifications of the full Navier-Stokes equations are applied in different parts (or zones) of the flow domain. Outside the boundary layer, the flow can be considered inviscid and the viscous terms in equations (2.2) are neglected. For the flow inside the boundary layer, significant simplifications can also be made after applying a dimensional analysis and neglecting all the sufficiently small terms. For incompressible flow with constant density the energy equation is decoupled from the continuity equation and the momentum equation and does not have to be solved to find the flow field. It results in the boundary layer equations:

$$\frac{\partial u}{\partial x} + \frac{\partial v}{\partial y} = 0, \tag{2.9a}$$

$$\frac{\partial u}{\partial t} + u\frac{\partial u}{\partial x} + v\frac{\partial u}{\partial y} = -\frac{1}{\rho}\frac{\partial P}{\partial x} + \nu\frac{\partial^2 u}{\partial y^2}, \tag{2.9b}$$

$$\frac{\partial P}{\partial y} = 0. \tag{2.9c}$$

It is clear that the equations are parabolic as all the second derivatives with respect to x can be neglected. Furthermore, the component of the pressure gradient in the y direction is zero which makes the pressure P a known variable in boundary layer simulation as it is equal to the edge pressure P_e which can be obtained from an

inviscid flow calculation. The x-momentum equation (2.9a) at the edge of boundary layer can be rewritten as:

$$\frac{\partial u_e}{\partial t} + u_e \frac{\partial u_e}{\partial x} = -\frac{1}{\rho}\frac{\partial P_e}{\partial x}, \tag{2.10}$$

and we can then combine (2.9b), (2.9c) into one equation:

$$\frac{\partial u}{\partial t} + u\frac{\partial u}{\partial x} + v\frac{\partial u}{\partial y} = \frac{\partial u_e}{\partial t} + u_e\frac{\partial u_e}{\partial x} + \nu\frac{\partial^2 u}{\partial y^2}. \tag{2.11}$$

For turbulent boundary layers, a Reynolds time averaging process is applied. As a common way to describe turbulent flows, the Reynolds averaging process separates the flow variable into a mean value and a fluctuation, i.e. $f = \overline{f} + f'$. This is a valid decomposition as long as the following Reynolds conditions are satisfied:

$$\begin{cases} \overline{f+g} = \overline{f} + \overline{g}, \\ \overline{\alpha} = \alpha, \text{ where } \alpha \text{ is constant}, \\ \overline{\alpha f} = \alpha \overline{f}, \text{ where } \alpha \text{ is constant}, \\ \overline{\left(\frac{\partial f}{\partial s}\right)} = \frac{\partial \overline{f}}{\partial s}, \text{ where } s \text{ can be either a space or a time coordinate}, \\ \overline{\overline{f} g} = \overline{f} \cdot \overline{g}. \end{cases} \tag{2.12}$$

For Reynolds time averaging of a flow variable such as the velocity $u = \overline{u} + u'$, an example is given in Figure 2-2.

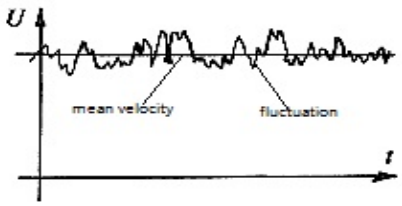

Figure 2-2: Decomposition of the velocity in turbulent flow in a mean value and a fluctuation to perform Reynolds averaging process.

The time-averaged value of u is defined as:

$$\overline{u} = \frac{1}{T}\int_{t_0}^{t_0+T} u \; dt. \tag{2.13}$$

Since the average of the fluctuation $\overline{u'} = 0$ by definition, we can study its mean-square

value:

$$\overline{u'^2} = \frac{1}{T}\int_{t_0}^{t_0+T} u'^2 \, dt. \tag{2.14}$$

Therefore, for turbulent flow, the boundary layer equations become:

$$\frac{\partial \overline{u}}{\partial x} + \frac{\partial \overline{v}}{\partial y} = 0, \tag{2.15a}$$

$$\frac{\partial \overline{u}}{\partial t} + \overline{u}\frac{\partial \overline{u}}{\partial x} + \overline{v}\frac{\partial \overline{u}}{\partial y} = \frac{\partial u_e}{\partial t} + \frac{1}{\rho}\frac{\partial \tau}{\partial y} + u_e\frac{du_e}{dx}, \tag{2.15b}$$

with the total shear stress defined as:

$$\tau = \mu\frac{\partial \overline{u}}{\partial y} - \rho\overline{u'v'}.$$

In practice, integral boundary layer (IBL) models are widely used if we have no interest in the the details of the flow *inside* the boundary layer. They greatly reduce the number of unknowns to define the boundary layer profiles at each surface point as the dimension of the problem is reduced by one. On the other hand, they also demonstrate good accuracy, for both attached flows and detached flows. One traditional way of obtaining these integral equations is assuming a (parameterized) velocity profile in the boundary layer and integrating over the height of the boundary layer at each point on the boundary of the domain where a boundary layer is present. The momentum integral equation (unsteady Von Kármán equation), used in most integral methods, can be written as:

$$\frac{\partial\left(u_e\delta^*\right)}{\partial t} + \frac{\partial\left(u_e^2\theta\right)}{\partial x} + u_e\frac{\partial u_e}{\partial x}\delta^* = \frac{C_f}{2}u_e^2, \tag{2.16}$$

where

$$\text{wall friction coefficient:} \quad C_f = \frac{2\tau_w}{\rho u_e^2}.$$

Most integral boundary layer models use a second equation which can be obtained in a variety of ways but always require a turbulent closure model. In the present work, two integral methods are considered:

1. the mean-flow-kinetic-energy integral method (or the dissipation integral method)[47],

2. the entrainment integral method[22].

For the dissipation integral method, the second equation is obtained by integrating the product of the stream-wise velocity and the stream-wise momentum equation in the boundary normal direction, given by:

$$\frac{\partial\left(u_e^2\theta\right)}{\partial t} + u_e^2\frac{\partial\delta^*}{\partial t} + \frac{\partial u_e^3\delta^k}{\partial x} = \frac{C_D}{2}u_e^3, \tag{2.17}$$

with:

$$\begin{aligned}
\text{viscous dissipation:} \quad D &= \int_0^\infty \tau\frac{\partial u}{\partial y}dy, \\
\text{viscous dissipation coefficient:} \quad C_D &= \frac{2D}{\rho u_e^3}, \\
\text{kinetic energy thickness:} \quad \delta^k &= \int_0^\infty \frac{u}{u_e}\left(1-\frac{u^2}{u_e^2}\right)dy.
\end{aligned}$$

The second equation for the entrainment method is simply the integrated form of the continuity equation:

$$\frac{\partial\delta}{\partial t} + \frac{\partial(u_e(\delta-\delta^*))}{\partial x} = C_E u_e, \tag{2.18}$$

with

$$\text{entrainment coefficient:} \quad C_E = \frac{1}{u_e}\frac{d}{dx}\int_0^\delta u dy \tag{2.19}$$

The momentum integral equation and the two secondary equations are dependent on three variables: δ^*, θ and u_e. The *direct formulation* of these equations corresponds to a boundary-layer solution with u_e prescribed while the *inverse formulation* treats u_e as an unknown variable with prescribed θ. Closure relations of other quantities such as C_f and C_D are required to make the system uniquely solvable and will be introduced in later sections.
For discretisation of these equations, the Discontinuous Galerkin method (DG) is used (see Chapter 4). Therefore, it is preferable to write equation (2.16), (2.17), (2.18) in conservation form:

$$\frac{\partial \delta^*}{\partial t} + \frac{\partial \left(u_e \theta\right)}{\partial x} = \frac{C_f}{2} u_e - \left(\delta^* + \theta\right) \frac{\partial u_e}{\partial x} - \delta^* \frac{1}{u_e} \frac{\partial u_e}{\partial t}, \tag{2.20}$$

$$\frac{\partial \left(\delta^* + \theta\right)}{\partial t} + \frac{\partial \left(u_e \delta^k\right)}{\partial x} = C_D u_e - 2\delta^k \frac{\partial u_e}{\partial x} - 2\theta \frac{1}{u_e} \frac{\partial u_e}{\partial t}, \tag{2.21}$$

$$\frac{\partial \delta}{\partial t} + \frac{\partial (u_e(\delta - \delta^*))}{\partial x} = C_E u_e. \tag{2.22}$$

Summarizing, the dissipation integral method system is the combination of equation (2.20) and (2.21):

$$\boxed{\begin{aligned} \frac{\partial \delta^*}{\partial t} + \frac{\partial \left(u_e \theta\right)}{\partial x} &= \frac{C_f}{2} u_e - \left(\delta^* + \theta\right) \frac{\partial u_e}{\partial x} - \delta^* \frac{1}{u_e} \frac{\partial u_e}{\partial t}, && (2.20) \\ \frac{\partial \left(\delta^* + \theta\right)}{\partial t} + \frac{\partial \left(u_e \delta^k\right)}{\partial x} &= C_D u_e - 2\delta^k \frac{\partial u_e}{\partial x} - 2\theta \frac{1}{u_e} \frac{\partial u_e}{\partial t}. && (2.21) \end{aligned}}$$

The entrainment integral method system is given by:

$$\boxed{\begin{aligned} \frac{\partial \delta^*}{\partial t} + \frac{\partial \left(u_e \theta\right)}{\partial x} &= \frac{C_f}{2} u_e - \left(\delta^* + \theta\right) \frac{\partial u_e}{\partial x} - \delta^* \frac{1}{u_e} \frac{\partial u_e}{\partial t}, && (2.20) \\ \frac{\partial \delta}{\partial t} + \frac{\partial (u_e(\delta - \delta^*))}{\partial x} &= C_E u_e. && (2.22) \end{aligned}}$$

Introducing the following shape factors:

$$H = \frac{\delta^*}{\theta}, \quad H^* = \frac{\delta^k}{\theta}, \quad H_1 = \frac{\delta - \delta^*}{\theta},$$

we obtain the final formulation of the system of the dissipation integral method as:

$$\boxed{\begin{aligned} \frac{\partial (H\theta)}{\partial t} + \frac{\partial \left(u_e \theta\right)}{\partial x} &= \frac{C_f}{2} u_e - \theta \left(H + 1\right) \frac{\partial u_e}{\partial x} - \frac{H\theta}{u_e} \frac{\partial u_e}{\partial t}, && (2.23) \\ \frac{\partial \left(\theta(H + 1)\right)}{\partial t} + \frac{\partial \left(u_e H^* \theta\right)}{\partial x} &= C_D u_e - 2H^* \theta \frac{\partial u_e}{\partial x} - 2\frac{\theta}{u_e} \frac{\partial u_e}{\partial t}. && (2.24) \end{aligned}}$$

And the system of the entrainment integral method as:

$$\boxed{\begin{aligned} \frac{\partial (H\theta)}{\partial t} + \frac{\partial \left(u_e \theta\right)}{\partial x} &= \frac{C_f}{2} u_e - \theta \left(H + 1\right) \frac{\partial u_e}{\partial x} - \frac{H\theta}{u_e} \frac{\partial u_e}{\partial t}, && (2.23) \\ \frac{\partial \left(\theta(H + H_1)\right)}{\partial t} + \frac{\partial u_e H_1 \theta}{\partial x} &= C_E u_e. && (2.25) \end{aligned}}$$

Note that recently new integral boundary layer models have been developed such as by Drela[14] and also at ECN by Seubers[43]. The derivation of the model by Seubers is started from the integral form of the flow governing equations (2.1) and an averaging procedure over a control volume is applied (see Figure 2-3 for an example of the control volume). This approach basically avoids most of the approximations used in the boundary layer equations and can be applied more generally such as in separated boundary layer and surfaces with curvature. However, this approach is not yet fully developed and the focus of the current study is not on the development of this new model, thus it is not used in the present work.

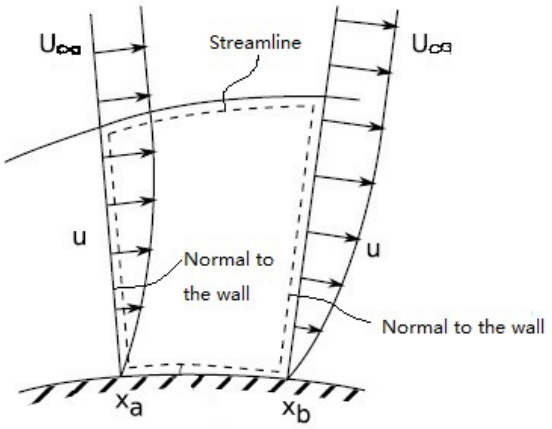

Figure 2-3: The control volume used to derive the boundary integral method of Seubers [43].

2.3 System of equations for the laminar boundary layer

For modeling the flow in laminar boundary layers, either of the two integral boundary layer methods can be used. In ECN's in-house developed IBL-DG code, van den Boogaard[48] applies the dissipation integral method and reports good results for attached flow. The system can be written as:

$$\boxed{\frac{\partial \mathbf{F}(\mathbf{u})}{\partial t} + \frac{\partial \mathbf{G}(\mathbf{u})}{\partial x} = \mathbf{S}(\mathbf{u})}\,, \tag{2.26}$$

with:

$$\mathbf{u} = \begin{bmatrix} H \\ \theta \end{bmatrix}, \quad \mathbf{F}(\mathbf{u}) = \begin{bmatrix} H\theta \\ \theta(H+1) \end{bmatrix}, \quad \mathbf{G}(\mathbf{u}) = \begin{bmatrix} u_e\theta \\ u_e H^*\theta \end{bmatrix}, \tag{2.27a}$$

$$\mathbf{S}(\mathbf{u}) = \begin{bmatrix} \frac{C_f}{2}u_e - \theta\,(H+1)\,\frac{\partial u_e}{\partial x} - \frac{H\theta}{u_e}\frac{\partial u_e}{\partial t} \\ C_D u_e - 2H^*\theta\frac{\partial u_e}{\partial x} - 2\frac{\theta}{u_e}\frac{\partial u_e}{\partial t} \end{bmatrix}. \tag{2.27b}$$

For the present work, the edge velocity u_e is prescribed. Thus, closure relations for H^*, C_f and C_D are still needed. Closure relations can be derived by modeling the particular unknowns in terms of other variables using experimental data or analytical solutions of representative test cases under certain assumptions. Within this study, the closure relations given by Drela[11] are used:

$$C_f = \overline{C_f}\frac{2\nu}{u_e\theta}, \tag{2.28}$$

$$C_D = \overline{C_D}H^*\frac{\nu}{u_e\theta}, \tag{2.29}$$

with:

$$H^* = \begin{cases} 1.528 + 0.0111\frac{(H-4.34)^2}{H+1} - 0.0278\frac{(H-4.35)^3}{H+1} & \\ -0.0002[(H-4.35)H]^2, & H < 4.35\,, \\ 1.528 + 0.015\frac{(H-4.35)^2}{H}, & H \geq 4.35 \end{cases} \tag{2.30}$$

$$\overline{C_f} = \begin{cases} \frac{1}{2}\left[-0.07 + 0.0727\frac{(5.5-H)^3}{H+1}\right], & H < 5.5 \\ \frac{1}{2}\left[-0.07 + 0.015\left(1 - \frac{1}{H-4.5}\right)^2\right], & H \geq 5.5 \end{cases}, \tag{2.31}$$

$$\overline{C_D} = \begin{cases} 0.207 + 0.00205(4-H)^{5.5}, & H < 4 \\ 0.207 - 0.0016\frac{(H-4)^2}{1+0.02(H-4)^2}, & H \geq 4 \end{cases}. \tag{2.32}$$

For steady incompressible cases without pressure gradient, nearly every laminar velocity profile is very close to the Falkner-Skan profile with the same shape factor. This makes the above relations very accurate. Although these closure relations are obtained from the solutions of steady models, they will also be applied on unsteady

cases. Because the development of closure relations is outside the scope of the current work, no further investigation will be done on the accuracy of these closure relations and the selected ones are accepted unaltered and assumed to be accurate for the present study. Details of validity of different closure relations can be found in van Garrel[50] and van Es[49].

It is necessary to point out that the current system is unable to treat separated flow due to the existence of the *Goldestein sigularity*[20]. Note that system (2.26) is a system of hyperbolic conservation laws with a source term. Rewriting the spatial flux vector $\mathbf{G}$ in terms of the temporal flux vector $\mathbf{F}$ gives:

$$\mathbf{G} = u_e \begin{bmatrix} \theta(H+1) - H\theta \\ (\theta(H+1) - H\theta)H^*(H\theta, \theta(H+1)) \end{bmatrix} = u_e \widetilde{\mathbf{G}}(\mathbf{F}). \tag{2.33}$$

Substituting equation (2.33) into (2.26) gives the convective formulation:

$$\frac{\partial \mathbf{F}}{\partial t} + u_e \frac{\partial \widetilde{\mathbf{G}}}{\partial \mathbf{F}} \frac{\partial \mathbf{F}}{\partial x} = \mathbf{S} + \widetilde{\mathbf{G}} \frac{\partial u_e}{\partial x}, \tag{2.34}$$

with:

$$u_e \frac{\partial \widetilde{\mathbf{G}}}{\partial \mathbf{F}} = u_e \begin{bmatrix} -1 & 1 \\ -H^* + (H+1)\frac{\partial H^*}{\partial H} & H^* - H\frac{\partial H^*}{\partial H} \end{bmatrix} = A. \tag{2.35}$$

At the point $\dfrac{\partial H^*}{\partial H} = 0,\ H \approx 4.198$, around which separation of laminar boundary layer is considered to be triggered, the operating matrix A is singular and the computation of the solution is not straightforward anymore. As the method to compute a steady solution in the current implementation of the IBL equations requires the inversion of this matrix to find the unknown $\mathbf{F}$, the solution procedure will eventually blow up as the solution reaches the separation point. Although the inversion of the matrix is not needed for the computation of the unsteady solution, the correct steady solution for separated flows cannot be reached as the singularily is not removed at finite time[48]. One way to avoid the problem is to formulate the equations in terms of the unknown H^* rather than H . However, due to the character of the current closure relation for H^*, the fact that $H^*(H)$ is not an explicit function again makes that the solution cannot be found in a straightforward manner. Another widely accepted way to resolve the singularity is to couple the boundary layer solver with the inviscid flow solver using a viscous-inviscid interaction scheme. One more equation will be added to the current system and this will make the system nonconservative. Currently, a quasi-simultaneous interaction scheme for integral boundary layer equations is under

development at ECN ([23], [43]) but not yet coupled in the present work.
In order to model laminar to turbulent transition, one more equation has to be added to the system. This will be discussed in detail in Chapter 3.

2.4 System of equations for the turbulent boundary layer

The extension of the model to describe turbulent boundary layers is one of the main focuses of the present work. Currently no turbulence model is implemented in ECN's in-house developed IBL-DG code. Therefore, both of the two IBL methods with corresponding closure relations are investigated. A third equation, namely the shear-lag equation is added to the system for non-equilibrium turbulence model which also takes the upstream history effects (i.e. flow with an adverse pressure gradient such as separated flow) into consideration.

2.4.1 Turbulent integral boundary layer equations

The dissipation integral method is the same for the turbulent boundary layer as for the laminar system (2.26) but for the closure relations. Due to the fact that turbulent boundary layers have a two-layer structure where the thickness of each layer scales differently with the local Reynolds number Re_θ, a one-parameter velocity profile family is simply not adequate to describe all turbulent boundary layers and the dependency on Re_θ must be considered. Closure sets can be found in literature ([47], [11], [33], etc.). For the present work, the closure set from Nishida[33] is taken, which originates from Drela[11] and several small corrections have been made. For incompressible flow, the skin friction coefficient C_f is given by:

$$C_f = \frac{0.3e^{-1.33H}}{\left(\log_{10} Re_\theta\right)^{1.74+0.31H}} + 0.00011\left[\tanh\left(4 - \frac{H}{0.875}\right) - 1\right]. \tag{2.36}$$

The energy thickness shape factor H^* is defined as:

$$H^* = \begin{cases} 1.505 + \frac{4}{Re_\theta} + \left(0.165 - \frac{1.6}{\sqrt{Re_\theta}}\right)\frac{(H_0-H)^{1.6}}{H}, & H < H_0 \\ 1.505 + \frac{4}{Re_\theta} + (H-H_0)^2\left[\frac{0.04}{H} + 0.007\frac{\ln Re_\theta}{\left(H-H_0+\frac{4}{\ln Re_\theta}\right)^2}\right], & H \geq H_0 \end{cases}, \tag{2.37}$$

with:

$$H_0 = \begin{cases} 3 + \frac{400}{Re_\theta}, & H_0 \geq 400 \\ 4, & H_0 < 400 \end{cases}.$$

The dissipation coefficient C_D is the most difficult correlation to derive in the turbulent case as it depends on the Reynolds stress distribution across the boundary layer[11]. There are two distinct approaches to formulate the closure relation. Thomas[47] splits the turbulent boundary layer into two parts, the wall layer and the outer layer, both of which contribute to the definition of the dissipation coefficient. He employs the slip velocity concept for the wall layer which has nearly constant total shear stress and an eddy viscosity hypothesis for the outer layer where the wake velocity profile and an effective eddy viscosity are assumed to determine the total shear stress. It is given by:

$$\begin{aligned} C_D &= \underbrace{C_f \frac{u_s}{u_e}}_{C_{Di}} + \underbrace{\frac{\pi^2 K}{8}\left(1 - \frac{u_s}{u_e}\right)^3}_{C_{Do}} \\ &= \frac{\sqrt{2}}{2} C_f^{\frac{3}{2}} \frac{\pi}{0.18} + \frac{\pi^2 K}{8}\left(\frac{4}{3}\frac{H-1}{H}\right)^3, \end{aligned} \tag{2.38}$$

where $K = 0.0168$ is the eddy viscosity coefficient. Alternatively, a method is proposed by Green[22] and Drela[11] which combines the experimentally determined $G - \beta$ locus for equilibrium flow with the momentum and mean-flow-kinetic-energy equation, and thus the dissipation can be determined in terms of local properties, i.e. Re_θ and H. Equilibrium flow means that the turbulent boundary layer profile is analogous to the Falkner-Skan profile for the laminar boundary layer and thus is self-preserving (or similar). In particular, the pressure gradient parameter β is given by:

$$\beta \equiv \frac{\delta^*}{\tau_w}\frac{dP}{dx} = -\frac{2}{C_f}\frac{\delta^*}{u_e}\frac{du_e}{dx}. \tag{2.39}$$

This parameter is constant, and the modified shape factor G is given by:

$$G = \frac{H-1}{H}\frac{1}{\sqrt{\frac{C_f}{2}}}, \tag{2.40}$$

which is also constant. Hence, for equilibrium flow, G is only a function of β:

$$G(\beta) = 6.7\sqrt{1 + 0.75\beta}. \tag{2.41}$$

Note that C_f and H^* are primarily dependent on H (their dependency on Re_θ is weak), and H is nearly constant, leading to the formulation of C_D:

$$C_D = C_f \frac{H^*}{6}\left(\frac{4}{H} - 1\right) + 0.03H^*\left(\frac{H-1}{H}\right)^3. \tag{2.42}$$

Comparing equations (2.42) and (2.38), we can see a close resemblance. It should not be surprising because the eddy viscosity hyphothesis used in Thomas's correlation (2.38) is also based on the experimental work from Clauser which determines the equilibrium flow. As (2.42) is from the same author who gives (2.36) and (2.37), and the fact that it is drawn directly from the experimental data rather than using the eddy viscosity hyphothesis based on this set of data, equation (2.42) is used in the present work to complete the closure set.

Alternatively, the entrainment integral method can be formulated for turbulent cases. The system (2.26) then becomes:

$$\frac{\partial \mathbf{F}(\mathbf{u})}{\partial t} + \frac{\partial \mathbf{G}(\mathbf{u})}{\partial x} = \mathbf{S}(\mathbf{u}), \tag{2.26}$$

with:

$$\mathbf{u} = \begin{bmatrix} H \\ \theta \end{bmatrix}, \quad \mathbf{F}(\mathbf{u}) = \begin{bmatrix} H\theta \\ \theta(H + H_1) \end{bmatrix}, \quad \mathbf{G}(\mathbf{u}) = \begin{bmatrix} u_e\theta \\ u_e H_1 \theta \end{bmatrix}, \tag{2.43a}$$

$$\mathbf{S}(\mathbf{u}) = \begin{bmatrix} \frac{C_f}{2}u_e - \theta\,(H+1)\,\frac{\partial u_e}{\partial x} - \frac{H\theta}{u_e}\frac{\partial u_e}{\partial t} \\ C_E u_e \end{bmatrix}. \tag{2.43b}$$

with H_1:

$$H_1 = \begin{cases} \frac{(0.5H+1)H}{H-1} & H \leq 4, \\ 1.75 - \frac{5.22273H}{H+5.818181} & H > 4, \end{cases}$$

The closure set from Green[22] is used in the present work but a modification is made to the formulation of the skin friction coefficient C_f to make it the same as equation

(2.36). The entrainment coefficient C_E is given by:

$$C_E = H_1 \left[\frac{C_f}{2} - (H+1) \left(\frac{\theta}{u_e} \frac{du_e}{dx} \right)_{EQ} \right], \tag{2.44}$$

with

$$\left(\frac{\theta}{u_e} \frac{du_e}{dx} \right)_{EQ} = \frac{1.25}{H} \left[\frac{C_f}{2} - \left(\frac{H-1}{6.432H} \right)^2 \right], \tag{2.45}$$

and the subscript EQ stands for equilibrium flow.

Both of the IBL methods are validated for turbulent boundary layers. The results and discussion of the validation process are presented in Chapter 5.

2.4.2 Non-equilibrium model: the shear-lag equation

As stated in the previous section, the turbulent dissipation coefficient C_D and the entrainment coefficient C_E depend only on local parameters H and Re_θ. This assumption is reasonably accurate in boundary layers whose turbulence production and dissipation mechanisms are in near equilibrium. Actually, almost all algebraic turbulence models make the assumption of a local equilibrium[11]. However, experimental results (e.g. Goldberg[19]) show that there are significant upstream history effects on Reynolds stresses for flows with an adverse pressure gradient increasing severely downstream or flows where an adverse pressure gradient is suddenly removed. A common example is the flow in separated boundary layers.

One of the first attempts to introduce upstream history effects is made by Bradshaw and Ferriss[6]. They treat the Reynolds stress as an additional unknown and introduce a stress-transport equation, which is derived from the exact turbulent kinetic energy transport equation, into the system of turbulent boundary layers:

$$u \frac{\partial}{\partial x} \frac{-\overline{u'v'}}{2a_1} + v \frac{\partial}{\partial y} \frac{-\overline{u'v'}}{2a_1} = -\overline{u'v'} \frac{\partial u}{\partial y} - \frac{(-\overline{u'v'})^{\frac{3}{2}}}{L} - \frac{\partial \mathcal{D}}{\partial y}, \tag{2.46}$$

where a_1 is defined to be a constant equaling 0.15, L is the dissipation length and $\mathcal{D}$ is the diffusion term. An integral form can also be obtained without losing its physical content. Green[22] assumes the point of maximum Reynolds stress being representative of the Reynolds stress level for the entire boundary layer. A non-

dimensional quantity, the shear stress coefficient C_τ is then introduced:

$$C_\tau = \frac{1}{u_e^2}(-\overline{u'v'})_{\max} \tag{2.47}$$

Green also assumes that at the maximum shear stress point, L is equal to the conventional mixing length. Hence, the velocity gradient at the maximum shear stress point is given by:

$$\frac{\partial u}{\partial y} = \frac{1}{L}(-\overline{u'v'})^{\frac{1}{2}}_{\max}. \tag{2.48}$$

Equation (2.46) becomes:

$$\frac{\delta}{C_\tau}\frac{dC_\tau}{dx} = 2a_1\frac{u_e}{u}\frac{\delta}{L}(C_{\tau_{EQ}}^{\frac{1}{2}} - C_\tau^{\frac{1}{2}}) - \frac{\partial \mathcal{D}}{\partial y} - \frac{2\delta}{u_e}\frac{du_e}{dx}, \tag{2.49}$$

where $C_{\tau_{EQ}}$ is the shear stress coefficient value if the local boundary layer is assumed to be in equilibrium. Thomas[47] and Drela[11] further simplify the equation by neglecting the last two terms in equation (2.49). However, the present author feels that it is not appropriate to neglect the last term in case of considerable pressure gradient. Thus, equation (2.49) is formulated as:

$$\frac{\delta}{C_\tau}\frac{dC_\tau}{dx} = 2a_1\frac{u_e}{u}\frac{\delta}{L}(C_{\tau_{EQ}}^{\frac{1}{2}} - C_\tau^{\frac{1}{2}}) - \frac{2\delta}{u_e}\frac{du_e}{dx}. \tag{2.50}$$

The unsteady form of (2.50) can be found in Fenno[16] or Özdemir[38] and is rederived by the present author with modifications made (A detailed derivation is presented in Appendix A):

$$\frac{\partial(\frac{u_e}{u}C_\tau)}{\partial t} + \frac{\partial(u_e C_\tau)}{\partial x} = \frac{C_\tau u_e}{\delta}K_c\left(C_{\tau_{EQ}}^{\frac{1}{2}} - C_\tau^{\frac{1}{2}}\right) - \frac{u_e}{u}\frac{2C_\tau}{u_e}\frac{\partial u_e}{\partial t} - C_\tau\frac{\partial u_e}{\partial x}, \tag{2.51}$$

with

$$K_c = 2a_1\frac{u_e}{u}\frac{\delta}{L}. \tag{2.52}$$

The commonly used values are $\frac{u_e}{u} = 1.5$ and $\frac{\delta}{L} = 12.5$ but Thomas[47] takes into account the dependency on the shape factor and gives $\frac{u_e}{u} = \frac{3H}{H+2}$, which is more accurate for separated flow profile and accepted by the present author.

Equation (2.50) or (2.51) is called the shear-lag equation. The interpretation of the equations is as follows: The dissipation coefficient is composed of a contribution of the wall and the outer layer. The wall shear coefficient (skin friction coefficient) C_f is unaffected by the upstream history effect and thus is only dependent on local parameters. The Reynolds stress of the outer layer represented by C_τ does not respond as quickly as the wall layer to the local conditions and tends to lag behind its local equilibrium value $C_{\tau_{EQ}}$. The rate of the lagging is therefore governed by the shear-lag equation.
Adding the shear-lag equation to the system (2.26), it becomes:

$$\mathbf{u} = \begin{bmatrix} H \\ \theta \\ C_\tau \end{bmatrix}, \quad \mathbf{F}(\mathbf{u}) = \begin{bmatrix} H\theta \\ \theta(H+1) \\ \frac{u_e}{u} C_\tau \end{bmatrix}, \quad \mathbf{G}(\mathbf{u}) = \begin{bmatrix} u_e\theta \\ u_e H^*\theta \\ u_e C_\tau \end{bmatrix}, \tag{2.53a}$$

$$\mathbf{S}(\mathbf{u}) = \begin{bmatrix} \frac{C_f}{2}u_e - \theta\left(H+1\right)\frac{\partial u_e}{\partial x} - \frac{H\theta}{u_e}\frac{\partial u_e}{\partial t} \\ C_D u_e - 2H^*\theta\frac{\partial u_e}{\partial x} - 2\frac{\theta}{u_e}\frac{\partial u_e}{\partial t} \\ \frac{C_\tau u_e}{\delta}K_c\left(C_{\tau_{EQ}}^{\frac{1}{2}} - C_\tau^{\frac{1}{2}}\right) - C_\tau\frac{\partial u_e}{\partial x} - \frac{u_e}{u}\frac{2C_\tau}{u_e}\frac{\partial u_e}{\partial t} \end{bmatrix}, \tag{2.53b}$$

for the dissipation integral method with the additional closure relations given by Drela[11]:

$$\delta = \theta\left(3.15 + \frac{1.72}{H-1}\right) + \delta^*, \tag{2.54}$$

$$U_s = \frac{H^*}{6}\left(\frac{4}{H} - 1\right), \tag{2.55}$$

$$C_{\tau_{EQ}} = \frac{H^*}{2}\frac{0.03}{1-U_s}\left(\frac{H-1}{H}\right)^3, \tag{2.56}$$

$$C_D = C_f U_s + 2C_\tau(1-U_s), \tag{2.57}$$

where U_s is the non-dimensional slip velocity.

For the entrainment integral method, the system becomes:

$$\mathbf{u} = \begin{bmatrix} H \\ \theta \\ C_E \end{bmatrix}, \quad \mathbf{F}(\mathbf{u}) = \begin{bmatrix} H\theta \\ \theta(H + H_1) \\ \frac{u_e}{u} C_\tau \end{bmatrix}, \quad \mathbf{G}(\mathbf{u}) = \begin{bmatrix} u_e\theta \\ u_e H_1 \theta \\ u_e C_\tau \end{bmatrix}, \tag{2.58a}$$

$$\mathbf{S}(\mathbf{u}) = \begin{bmatrix} \frac{C_f}{2} u_e - \theta\,(H+1)\,\frac{\partial u_e}{\partial x} - \frac{H\theta}{u_e}\frac{\partial u_e}{\partial t} \\ C_E u_e \\ \frac{C_\tau u_e}{\delta} K_c \left(C_{\tau_{EQ}}^{\frac{1}{2}} - C_\tau^{\frac{1}{2}} \right) - C_\tau \frac{\partial u_e}{\partial x} - \frac{u_e}{u}\frac{2C_\tau}{u_e}\frac{\partial u_e}{\partial t} \end{bmatrix}, \tag{2.58b}$$

with additional closure relations given by Green[22]:

$$C_{f0} = \frac{0.01013}{\log_{10}^{Re_\theta} - 1.02} - 0.00075 \tag{2.59}$$

$$1 - \frac{1}{H_0} = 6.55\sqrt{\frac{C_{f0}}{2}}, \tag{2.60}$$

$$0.9 = \left(\frac{C_f}{C_{f0}} + 0.5 \right) \left(\frac{H}{H_0} - 0.4 \right), \tag{2.61}$$

$$C_\tau = 0.024 C_E + 1.2 C_E^2 + 0.32 C_{f0}, \tag{2.62}$$

$$C_{\tau_{EQ}} = 0.024 (C_E)_{EQ} + 1.2 (C_E)_{EQ}^2 + 0.32 C_{f0}. \tag{2.63}$$

$(C_E)_{EQ}$ is given by (2.44) and δ is given by (2.54). For the present work, C_{f0} is substituted by a more recent closure relation based on equation (2.36):

$$C_{f0} = \frac{0.3 e^{-1.33H}}{(\log_{10} Re_\theta)^{1.74+0.31H}}. \tag{2.64}$$

In the code developed for the present work, users can decide whether to use the non-equilibrium model or not and a switch criterion is set as an input parameter based on the value of skin friction coefficient C_f (C_f reaches 0 as flow become separated). Results for a variety of test cases can be found in Chapter 5.

Chapter 3

Laminar-to-turbulent transition in the boundary layer

Although in the past few decades significant progress has been made in the development of reliable turbulence models, the research on laminar to turbulent flow transition does not follow up quickly, especially for flow simulation. First of all, several different kinds of transition have to be considered, which causes difficulties in modeling. A distinction is made among natural transition resulting from a flow instability, bypass transition caused by a high turbulence level in the free-stream and separated flow transition where a laminar boundary layer separates under the influence of a pressure gradient. Furthermore, a turbulent boundary layer can re-laminarize under a strong favorable pressure gradient. Secondly, since transitional flow possesses both linear and nonlinear effects, the RANS procedure which eliminates linear disturbance growth has difficulty to describe such flows. Transition in a boundary layer can be affected by many factors, the most important ones being the pressure distribution in the external flow, (the nature of the) wall roughness and (the nature of the) disturbances in the free flow.

In this chapter, two of the most important transition modes, natural transition and bypass transition will be reviewed. Following will be the transition prediction methods studied for the present work. The extended e^N envelop method which can predict transition onset for both natural transition and bypass transition and the intermittency model which predicts the behavior of the flow in the transition region will be explained in detail.

3.1 Modeling of laminar-to-turbulent transition

Due to the fact that the current code is not able to treat boundary layer separation, for the present work, only natural transition and bypass transition are investigated. The modeling of separated flow transition will be left for further research.

3.1.1 Natural transition and the linear stability theory

The theoretical investigation of natural transition is based on the assumption that the laminar flow is affected by certain small disturbances and how the evolution of these disturbances leads to a change of the flow regime. If the disturbances decay with time, the mean flow remains laminar and is considered stable. On the other hand, if the disturbances increase with time, the flow is considered unstable and transition to turbulent flow may happen. In 1930, Prandtl stated that all types of laminar boundary layers could become unstable by the presence of viscous instability waves at some finite Reynolds number and predicted that particular value. Later, this was confirmed through experiments by Schubauer and Skramstadt[42], and made into a complete theory by Tollmien and Schlichting[40]. The instability waves seen in flows inside the boundary layer are called Tollmien-Schlichting (TS) waves. It is now generally accepted that when the free-stream turbulence level is low (normally $< 1\%$), a laminar boundary layer becomes linearly unstable beyond a certain limit (i.e. the critical momentum Reynolds number $Re_{\theta crit}$) at which TS waves start to grow. Here the turbulence level (for two-dimensional cases) is defined as (in percent):

$$Tu = \frac{\sqrt{\frac{1}{2}(\overline{u'^2} + \overline{v'^2})}}{u} \times 100. \tag{3.1}$$

Natural transition can thus be modeled by the linear stability theory.

Similar to the analysis of turbulent flow, the linear stability theory of laminar flows is based on a decomposition of the motion into a mean value and a disturbance superimposed on it. In order to distinguish the linearizing process in transitional boundary layer from the Reynolds averaging process in turbulent boundary layers (though the ideas behind both are the same), we use subscript m for the mean value, i.e. $u = u_m + u'$ and $P = P_m + P'$. Considering a two-dimensional incompressible mean flow with constant density, the disturbance can also be assumed to be two-dimensional because the onset of instability is mainly determined by the two-dimensional disturbances rather than the three-dimensional ones[54], both of which satisfy the Navier-Stokes equations. Furthermore, we can assume that $P_m = P_m(x)$ and $\partial u_m/\partial x = 0$ (*parallel flow assumption*), and thus, $v_m = 0$ according to the

continuity equation. For steady mean flow, we have:

$$u(x,y,t) = u_m(y) + u'(x,y,t), \tag{3.2a}$$

$$v(x,y,t) = \quad v'(x,y,t), \tag{3.2b}$$

$$P(x,y,t) = P_m(x) + P'(x,y,t). \tag{3.2c}$$

Recall Figure 2-1, here x is the stream-wise direction and y is the stream-normal direction.

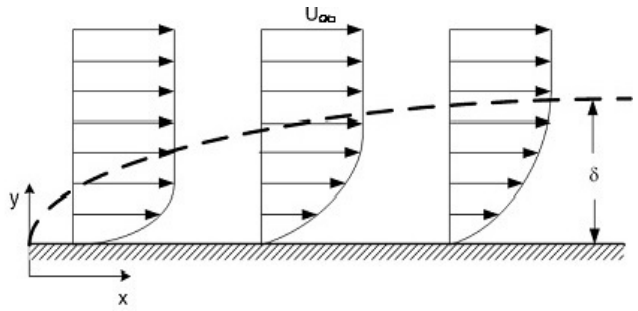

Figure 3-1: Definition of the reference system to describe the boundary layer on a flat plate.

Introducing this decomposition into the governing equations and linearizing, we get:

$$\frac{\partial u'}{\partial x} + \frac{\partial v'}{\partial y} = 0, \tag{3.3a}$$

$$\frac{\partial u'}{\partial t} + u_m\frac{\partial u'}{\partial x} + v'\frac{du_m}{dy} + \frac{1}{\rho}\frac{\partial P'}{\partial x} = \nu\nabla^2 u', \tag{3.3b}$$

$$\frac{\partial v'}{\partial t} + u_m\frac{\partial v'}{\partial x} + \frac{1}{\rho}\frac{\partial P'}{\partial y} = \nu\nabla^2 v', \tag{3.3c}$$

with the no-slip boundary condition such that $u' = v' = 0$ on the wall. The pressure disturbance can be easily eliminated and equations (3.3) become:

$$\frac{\partial u'}{\partial x} + \frac{\partial v'}{\partial y} = 0, \tag{3.4a}$$

$$\frac{\partial^2 u'}{\partial t\partial y} - \frac{\partial^2 v'}{\partial t\partial x} + u_m\left(\frac{\partial^2 u'}{\partial x\partial y} - \frac{\partial^2 v'}{\partial x^2}\right) + v'\frac{d^2 u_m}{dy^2} = \nu\left(\frac{\partial^3 u'}{\partial x^2\partial y} + \frac{\partial^3 u'}{\partial y^3} - \frac{\partial^3 v'}{\partial x^3} - \frac{\partial^3 v'}{\partial x\partial y^2}\right). \tag{3.4b}$$

We can then introduce a streamfunction $\psi(x,y,t)$ and use the assumption that the

disturbance amplitude function ϕ only depends on y to factorize it as:

$$\psi(x, y, t) = \phi(y)e^{i(\alpha x - \beta t)}, \tag{3.5}$$

where

$$u' = \frac{\partial \psi}{\partial y}, \quad v' = -\frac{\partial \psi}{\partial x},$$
$$\alpha = \alpha_r + i\alpha_i, \quad \beta = \beta_r + i\beta_i.$$

α_r is the wave number, β_r is the frequency and α_i and β_i are the spatial and temporal amplification rates. The two cases of most interest are those in which either α or β is real. If α is real, we have a temporal mode in which the disturbances only change with time and if β is real, we have a spatial mode in which the distubances change spatially. A relation between the two modes can be obtained[18]. Traditionally, in applications for steady mean flows, the temporal mode is used[40]. However, currently the spatial mode is more accepted especially for airfoil applications because for the temporal mode integration still has to be done in space and it cannot take into account the effects of nonparallel flow in the boundary layer. For example, Drela[11] uses the spatial mode for the simplified e^N envelop method which we will discuss in Section 3.2.

For the temporal form,

$$\alpha = \alpha_r, \quad \beta = \beta_r + i\beta_i,$$
$$\psi(x, y, t) = \phi(y)e^{\beta_i t}e^{i(\alpha_r x - \beta t)}, \tag{3.6}$$

and the spatial form:

$$\alpha = \alpha_r + i\alpha_i, \quad \beta = \beta_r,$$
$$\psi(x, y, t) = \phi(y)e^{-\alpha_i x}e^{i(\alpha_r x - \beta t)}. \tag{3.7}$$

We introduce the ratio:

$$c = \frac{\beta}{\alpha} = c_r + ic_i. \tag{3.8}$$

From (3.5) we can get the values of u' and v' and their derivatives. Introducing them into (3.4) together with (3.8), we get the following fourth-order ordinary differential

equation for the amplitude $\phi(y)$:

$$(u^* - c^*)(\phi'' - \alpha^{*2}\phi) - (u^*)''\phi = -\frac{i}{\alpha^* Re_\theta}(\phi'''' - 2\alpha^{*2}\phi'' + \alpha^{*4}\phi), \tag{3.9}$$

with the dimensionless variables:

$$u^* = \frac{u_m}{U_\infty}, \quad y^* = \frac{y}{\theta}, \quad \alpha^* = \alpha\theta, \quad c^* = \frac{c}{U_\infty}, \quad \phi = \frac{\phi}{U_\infty \theta},$$

and primes denote differentiation with respect to y^*. All the superscripts "$*$" are dropped for consiseness.

This equation is known as the Orr-Sommerfeld equation. For a detailed derivation please refer to van Ingen[52]. The trivial solution $\phi = 0$ obviously represents the original undisturbed flow. The problem of assessing the stability has now been reduced to the solution of an eigenvalue problem with the boundary conditions:

$$\begin{cases} y = 0 \quad : \quad \phi(0) = \phi'(0) = 0; \\ y \to \infty : \quad \phi(\infty) = \phi'(\infty) = 0. \end{cases}$$

Note that for very high Reynolds numbers, the right hand side of equation (3.9) may be neglected and the order of the equation reduces to two. The resulting differential equations is known as Rayleigh's equation.

Finding the eigenfunction ϕ together with the corresponding eigenvalue c or β (for the temporal form with real values of Re_θ and α given) or eigenvalue α (for the spatial form with real values of Re_θ and β given) of (3.9) under the certain boundary conditions forms the eigenvalue problem of the Orr-Sommerfeld equation. A plethora of methods for the solution of the eigenvalue problem for different flows is presented in literature (Orszag[35], Jordinson[27], etc.). The results of stability calculations are normally presented in a so called stability diagram. Figure 3-2 is an example of a stability diagram of the spatial mode[53] ($\omega = \beta_r$ representing the frequency in the figure):

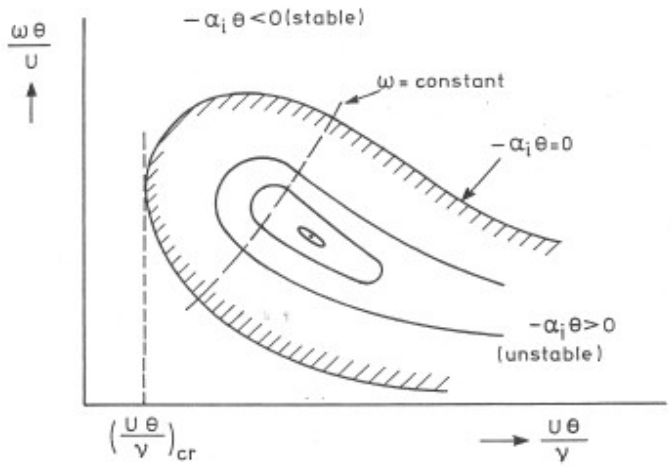

Figure 3-2: Stability diagram.

The disturbances grow, remain constant or decrease with x for $\alpha_i < 0, = 0, \; and \; > 0$, meaning that the given flow is unstable, neutrally stable or stable for the disturbance. The stability diagram may depends on the velocity profile, the frequency and the momentum thickness Reynolds number Re_θ. From the diagram, we can see that below $Re_{\theta crit}$ the boundary layer must be stable for small disturbances while at higher Reynolds numbers there is a range of frequencies for which instability occurs. Thus, $Re_{\theta crit}$ is defined as the lowest value of Re_θ for which one or more frequencies become unstable.

Note that the $Re_{\theta crit}$ obtained from a stability calculation cannot be expected to be equal to the experimentally observed value at the onset of transition ($Re_{\theta onset}$) since the calculated one indicates the point where instability is initiated. It may take some time and distance in the downstream direction before the instabilities transform to turbulence. The linear stability theory is in fact used to bridge the (sometimes large) distance between the point of first instability and the real transition in a way the onset of transition can be predicted. In Figure 3-3 the process of the development of natural transition[40] is visualized.

Many factors can affect transition, among which the pressure gradient is one of the most important and will be taken into account in this work. Favorable pressure gradients usually delay transition and adverse pressure gradients promote transition, but transition zone lengths are shorter in favorable pressure gradient. More details will be given in Section 3.2. Other effects such as suction/blowing, body forces, heat transfer and wall roughness on transition can be found in Schlichting[40].

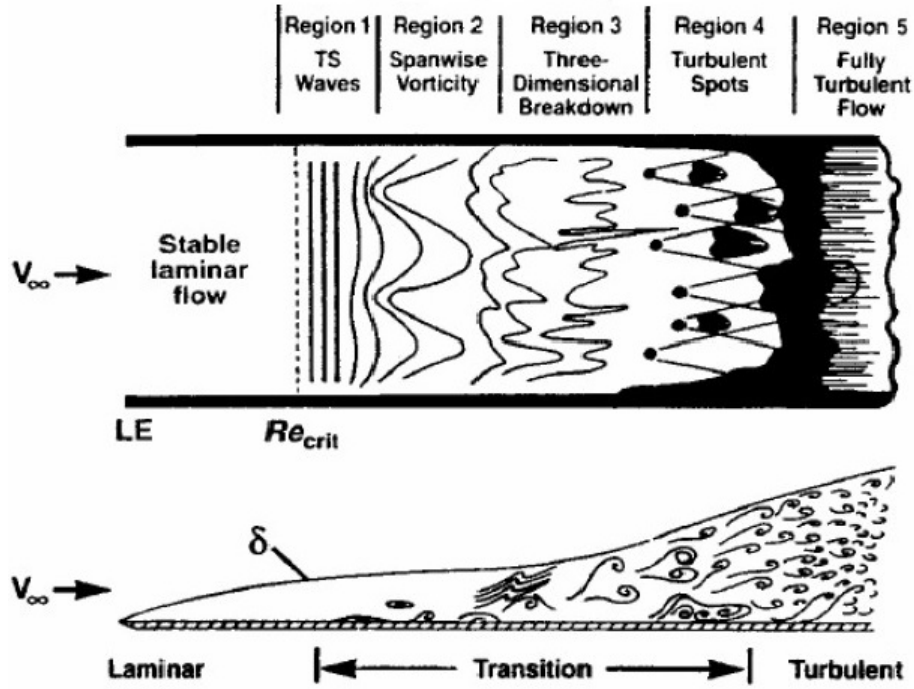

Figure 3-3: Visualization of the natural transition process in a boundary layer [40].

3.1.2 Bypass transition

For transition at high free-stream turbulence levels ($> 1\%$), the first and possibly the second and third regions in Figure 3-3 are bypassed by the influence of free-stream disturbances. It is often argued that the linear stability theory is no longer relevant for bypass transition as no single T-S wave frequency is observed in flows at free-stream turbulence level higher than 1%. However, experiments by Boiko et al[4] indicate that in fact T-S waves play a role in the transition process even with large free-stream turbulence levels, though they are difficult to distinguish from the externally imposed "noise". This makes bypass transition even more difficult to identify. Bypass transition can also occur due to surface roughness where the disturbances originate from the perturbations at the wall or when turbulent flow is injected directly into the boundary layer. It is the main transition phenomenon that generally occurs in turbomachinery applications. One very important example of bypass transition in turbomachinery is wake induced transition where the blade rows are subjected to each others periodically passing turbulent wakes. It is still not clear whether the transition is caused by the enhanced turbulence in the wake or the free-stream momentum deficit and its interaction with the boundary layer. In order to predict the onset of transition, we need to calculate the pre-transition laminar disturbances. The mechanism of bypass transition of course can be studied using direct numerical simulation (DNS)[60] or

large eddy simulation (LES)[31], but the prohibitive computational cost really limits the use of both. Therefore, numerical models based on the solution of the RANS equations are needed. Recent research aims at developing transition models based either on non-linear eddy viscosity methods and Reynolds-stress transport equations, or on the concept of intermittency, which represents the fraction of time the flow is turbulent. Especially single-point models are considered. The first type of approach provides accurate results for some test cases but fails to be "entirely satisfactory"[7]. Single-point models by Walters and Leylek[55] and some intermittency models (i.e. Langtry[30]) try to overcome the disadvantage of many previous models which rely on integral or non-local parameters, requiring only local variables such as the local velocity u and the distance from the nearest wall y and often related to other turbulence models such as the $k-\varepsilon$ model. Those approaches can treat geometrically complicated configurations better and they are more suitable for modern CFD applications. However, they cannot fit in the framework of the present study. Therefore, the intermittency model based on empirical algebraic correlations is eventually chosen here to model bypass transition. More details will be given in the Section 3.2.

3.2 Transition prediction methods

A variety of transition prediction methods have been studied for the present work, among which the e^N method is considered the most suitable one. Therefore this model will be further investigated. More details on the different transition prediction methods can be found in the literature review report for the present work[61]. In this section, the e^N envelop method will be firstly introduced to predict the onset of natural transition. It will be further extended to predict the onset of bypass transition as well. Its suitability for handling the pressure gradient as well as varying free-stream turbulence level will be discussed and improvement will be made to the model. An intermittency model will also be introduced to model the transition region.

3.2.1 The extended e^N envelope method

The e^N (originally e^9) method was firstly introduced by van Ingen[52] and Smith[44] more than 50 years ago. Based on the linear stability theory, it is widely accepted to semi-empirically provide good practical prediction of natural transition onset of incompressible two-dimensional boundary layers. Recall the Orr-Sommerfeld equation (3.9) and the definition of the streamfunction (3.5), only the real part of the streamfunction is physically significant. The amplitude of a disturbance a can be computed as a function of stream-wise distance x. Considering the ratio of the amplitudes a

and $a + da$, we have:

$$\frac{a+da}{a} = \frac{e^{\beta_i(t+dt)}}{e^{\beta_i t}} = e^{\beta_i dt}, \quad \text{temporal form} \tag{3.10}$$

$$\frac{a+da}{a} = \frac{e^{-\alpha_i(x+dx)}}{e^{-\alpha_i x}} = e^{-\alpha_i dx}. \quad \text{spatial form} \tag{3.11}$$

As it is extremely difficult to specify the initial disturbances a_0, the amplification rate n is introduced:

$$n = \ln\left(\frac{a}{a_0}\right) = \int_{t_0}^{t} \beta_i dt, \quad \text{temporal form} \tag{3.12}$$

$$= \int_{x_0}^{x} -\alpha_i dx. \quad \text{spatial form} \tag{3.13}$$

In practice, for general steady cases we use the spatial form and it can be written as:

$$n(x) = \int_{x_0}^{x} -\alpha_i dx = \frac{U_\infty \tilde{c}}{\nu} \cdot 10^{-6} \int_{\tilde{x}_0}^{\tilde{x}} T\tilde{U} d\tilde{x}, \tag{3.14}$$

with:

$$T(x) = \frac{-\alpha_i \theta}{Re_\theta} \cdot 10^6, \quad \tilde{x} = \frac{x}{\tilde{c}}, \quad \tilde{U} = \frac{u}{U_\infty}$$

The factor 10^6 have been introduced for convenience. Here $\tilde{c}$ is a constant reference length and $\tilde{x}_0$ denotes the value of $\tilde{x}$ at which the disturbance starts.
If we calculate T (and n as well) as a function of x for a range of frequencies (to do so the velocity profile and $Re_\theta = \frac{U\theta}{\nu}$ should be known functions of x) we get a set of n-curves. The envelope of these curves gives the maximum amplification rate N (N will be called the amplification factor in the remaining of the thesis) which occurs at any x. This is where the N in the name of e^N method comes from. If N reaches some critical value N_{crit}, transition is considered to be onset. In the first version of the method, N_{crit} is fixed and equals to 9. Later, it is found that each time when one of the components in the e^N method is changed (new boundary layer calculation method, improved stability diagrams, new experimental data etc.) the whole method will have to be re-calibrated and the N value may be changed. Van Ingen[54] later relates the N value at the onset of transition and the end of transition to the free-stream turbulence level based on various transition experiments on flat plates (also see Figure 3-4):

$$N_1 = 2.13 - 6.18 \log_{10} Tu, \tag{3.15}$$

$$N_2 = 5 - 6.18 \log_{10} Tu. \tag{3.16}$$

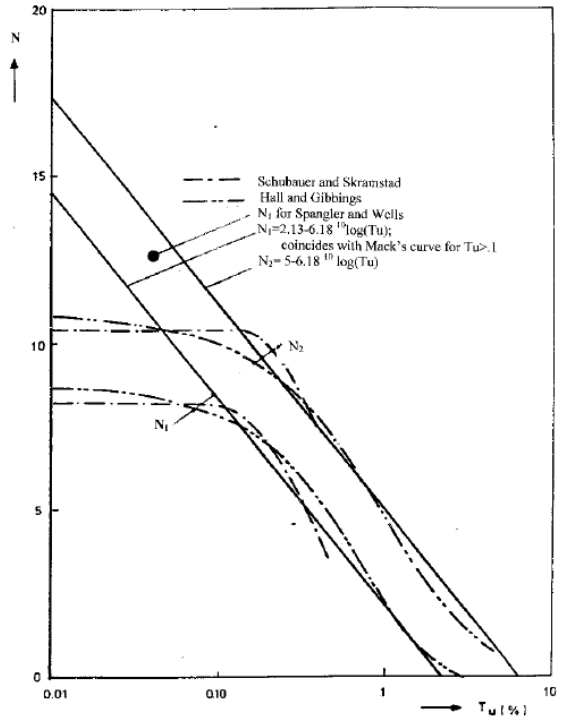

Figure 3-4: The amplification factor N for various flat plate experiments[54].

Mack[13] also gives his correlation for N_{crit} based on the same experimental data and this formulation will be used in the present work:

$$N_{crit} = -8.43 - 2.4 \ln(\frac{Tu}{100}). \tag{3.17}$$

Figure 3-5 shows an example of the n-curves and their envelop for the flat plate boundary layer without suction.

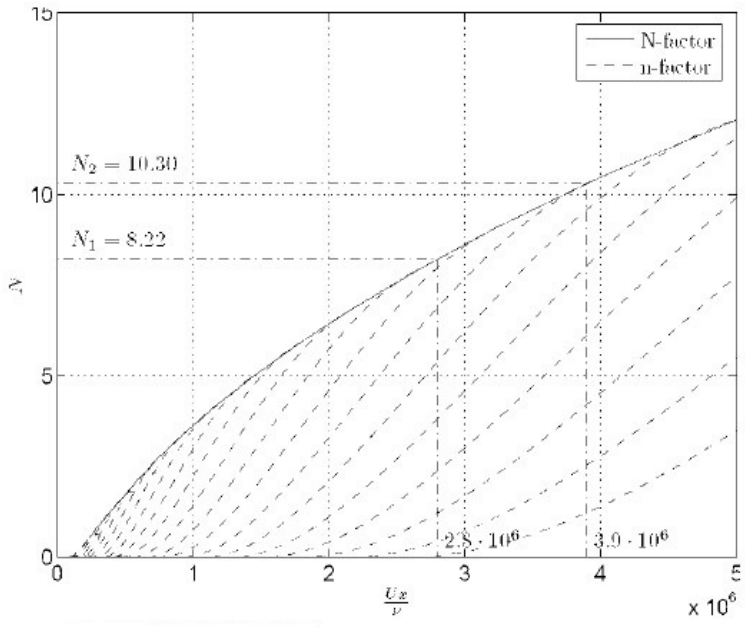

Figure 3-5: The amplification factor N for a flat plate[54].

From Figure 3-4 we can see that the correlations are only valid when the free-stream turbulence level $Tu \geq 0.1$. It is also possible to use these results for $Tu < 0.1$ but in those cases an "effective" value for Tu should be used. This effective value can only be determined through a comparison of measured transition positions with calculated amplification ratios. Normally, for cases of flat plates with low free-stream turbulence levels, the value of N_{crit} varies from 7 to 8.

Because of the relatively large computational effort required for solving the Orr-Sommerfeld equation for all velocity profiles at a large series of x-stations, the model needs to be simplified. The newest version of van Ingen's e^N method[54] is based on a database of pre-computed solutions for a standard series of velocity profiles at a number of Re_θ values. It is assumed that all stability diagrams form a one-parameter family with $Re_{\theta crit}$ as the single independent parameter. $Re_{\theta crit}$ can be related to the velocity profiles using some specific formulation and a characteristic parameter (i.e. the shape factor H) is sought to correlate an arbitrary boundary layer to this critical Reynolds number in order to find the corresponding stability diagram. The stability diagrams for the specific velocity profile will be used to calculate T. Nevertheless, considering the availability of resources and the efficiency and robustness of the model, Drela's simplified e^N method[11] is used for the present work. Drela uses a linear approximation of the envelopes of the spatial amplification curves of the Orr-Sommerfeld solutions for the Falkner-Skan profile family. This approximation of the curves by straight lines is shown in Figure 3-6. Any influence on the different behavior of individual frequencies is eliminated by only approximating the envelopes.

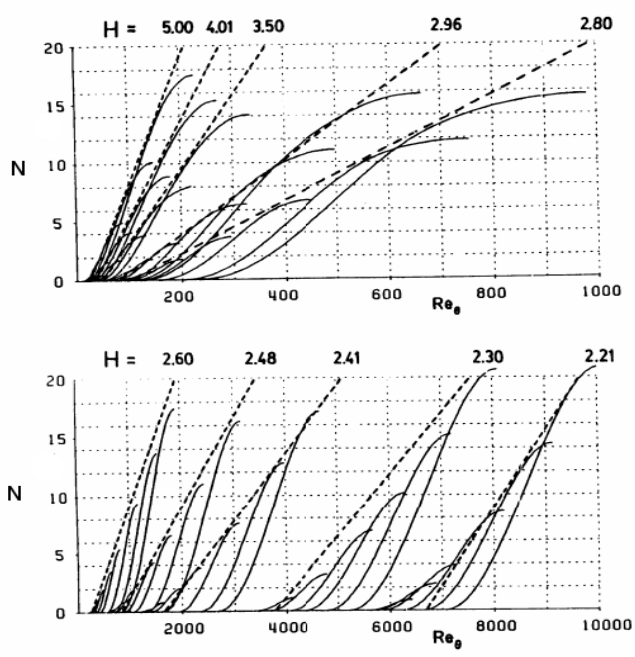

Figure 3-6: The envelope approximation to the stability region that forms the basis of Drela's method[11].

As the amplification factor N is given by:

$$N = \frac{dN}{dRe_\theta}\left(Re_\theta - Re_{\theta crit}\right). \tag{3.18}$$

The slope and critical momentum thickness Reynolds number are given by Drela[11]:

$$\frac{dN}{dRe_\theta} = 0.028(H-1) - 0.0345e^{-(3.87\frac{1}{H-1}-2.52)^2}, \tag{3.19}$$

$$\log_{10}(Re_{\theta_{crit}}) = 2.492\left(\frac{1}{H-1}\right)^{0.43} + 0.7\left(\tanh(14(\frac{1}{H-1}) - 9.24) + 1\right). \tag{3.20}$$

For the present work, a more realistic correlation for $Re_{\theta crit}$ is given by the author based on Arnal's experimental data[54] (see Table 3.1):

$$\log_{10}(Re_{\theta_{crit}}) = (\frac{0.267659}{H-1} + 0.394429)\tanh(\frac{12.7886}{H-1} - 8.57463) + \frac{3.04212}{H-1} + 0.6660931. \tag{3.21}$$

Note that when doing the data fitting, an asymptotic suction profile is added to the data set while the last data point with $H = 35.944$ is omitted.

Case	H	$\log_{10} Re_{\theta crit}$	Description
0	2.000	4.3643	asymptotic suction
1	2.216	3.7514	stagnation point
2	2.297	3.5279	
3	2.411	3.0738	
4	2.481	2.7479	
5	2.529	2.5371	
6	2.591	2.3024	flat plate
7	2.676	2.0711	
8	2.802	1.8487	
9	3.023	1.6198	
10	3.378	1.4179	
11	4.029	1.2174	separated flow
12	6.752	0.8352	
13	10.056	0.6019	
14	16.467	0.3455	
15	35.944	−0.0378	omitted

Table 3.1: Summary of data from Arnal[5].

Figure 3-7 gives the comparison of the two correlations.

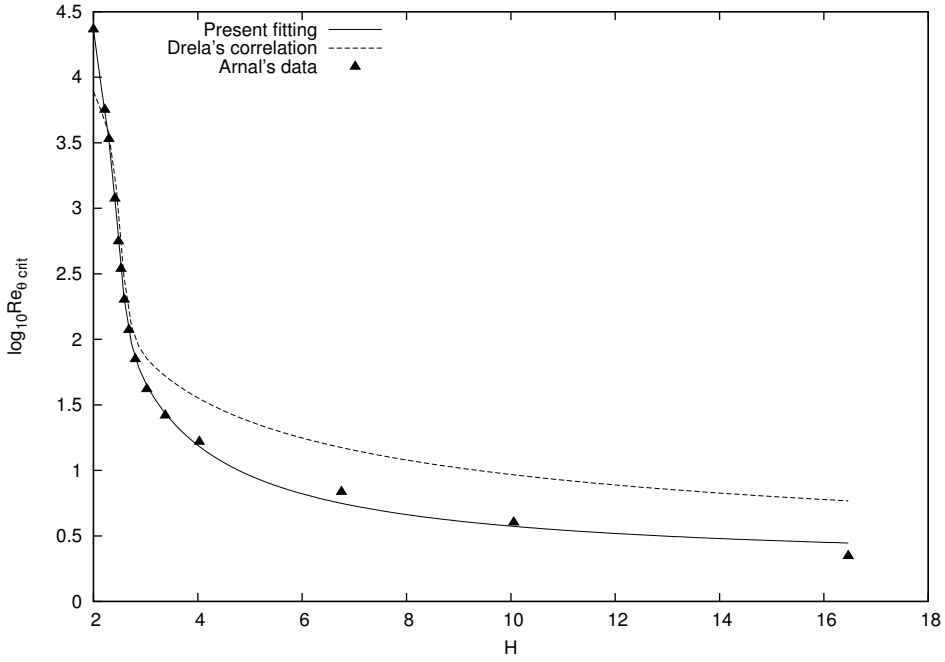

Figure 3-7: Correlations for $Re_{\theta crit}$.

For similar flow, H is constant and Re_θ is uniquely related to the stream-wise coordinate x. Equation (3.18) immediately gives the amplification factor N as a unique

function of x. For non-similar flow, it is better to use x as the spatial amplification coordinate rather than Re_θ. Thus, it becomes:

$$\frac{dN}{dx} = \frac{dN}{dRe_\theta}\frac{dRe_\theta}{dx} \times RFAC, \tag{3.22}$$

where $RFAC$ is a factor for numerical smoothness given by Drela[11]:

$$RFAC = \begin{cases} 0, & RNORM \leq 0 \\ 3RNORM^2 - 2RNORM^3, & 0 < RNORM < 1 \\ 1, & RNORM \geq 1 \end{cases} \tag{3.23}$$

with:

$$RNORM = \frac{\log_{10} Re_\theta - (\log_{10}(Re_{\theta_{crit}}) - 0.08)}{2 \times 0.08}. \tag{3.24}$$

$\frac{dRe_\theta}{dx}$ is given by empirical relation:

$$\frac{dRe_\theta}{dx} = -0.05 + 2.7\left(\frac{1}{H-1}\right) - 5.5\left(\frac{1}{H-1}\right)^2 + 3\left(\frac{1}{H-1}\right)^3. \tag{3.25}$$

For steady flow, equation (3.22) can be inserted into the global system (2.26) and solved together with the IBL equations.
The current formulation does take into account the pressure gradient as it correlates the growth rate of N with Re_θ and thus the edge velocity u_e. However, in practice it is also very possible that the free-stream turbulence level changes in the streamwise direction, such as in the case of the well known T3 series flat plate test cases[1]. Therefore, in the present work, the free-stream turbulence level Tu is introduced as the second parameter for the amplification rate N. Equation (3.22) becomes:

$$\frac{dN}{dx} = (\frac{\partial N}{\partial Re_\theta}\frac{dRe_\theta}{dx} + \frac{\partial N}{\partial Tu}\frac{dTu}{dx}) \times RFAC, \tag{3.26}$$

where $\frac{\partial N}{\partial Tu}$ is referred from equation (3.17):

$$\frac{\partial N}{\partial Tu} = \frac{C}{(-8.43 - 2.4\ln(\frac{Tu}{100}))^2 Tu}, \tag{3.27}$$

with the constant C determined by the results of T3 series test cases.

For a flat plate case with varying free-stream turbulence level in stream-wise direction, there is a lag between changes in the free-stream value of $Re_{\theta onset}$ and that inside the boundary layer (see Figure 3-8). The lag is desirable, as the onset of transition is primarily affected by the past history of pressure gradient and turbulence level and not the local value at transition[30]. Therefore, an "effective free-stream turbulence level" at every "x-station" in the stream-wise direction is also defined by the present author based on T3 series test cases:

$$Tu(x) = Tu(x-1) + 0.85\frac{dTu}{dx}dx, \tag{3.28}$$

with the initial value equaling to the free-stream turbulence level at the leading edge:

$$Tu(0) = Tu_{LE} \tag{3.29}$$

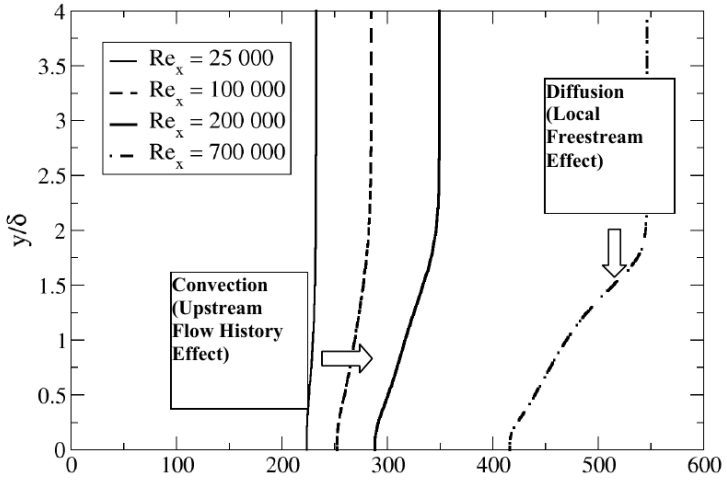

Figure 3-8: $Re_{\theta onset}$ with decaying free-stream turbulence level (T3A test case)[30].

Due to the fact that the e^N method is based on the growth of T-S waves, it can only predict the onset of natural transition. Bypass transition may onset even before the T-S waves starting to grow. In order to account for bypass transition, the current e^N method should be extended. This can be done by adding another term to equation

(3.26) based on the idea of Drela[13]:

$$\frac{dN}{dx} = (\frac{\partial N}{\partial Re_\theta}\frac{dRe_\theta}{dx} + \frac{\partial N}{\partial Tu}\frac{dTu}{dx}) \times RFAC + \frac{g(H, Re_\theta)}{\theta}. \tag{3.30}$$

Before introducing the new term, the free-stream turbulence level Tu in relation (3.17) needs to be modified because it produces negative N_{crit} values when $Tu > 2.98$ which makes no physical sense. The modification is given by:

$$Tu' = 2.7 \tanh(\frac{Tu}{2.7}), \tag{3.31}$$

$$N_{crit} = -8.43 - 2.4 \ln(\frac{Tu'}{100}). \tag{3.32}$$

This results in N_{crit} asymptotically approaches zero for large values of Tu, and becomes equivalent to Mack's original relation[13] for small values of Tu. Hence, $\frac{\partial N}{\partial Tu}$ results in:

$$\frac{\partial N}{\partial Tu} = \frac{43}{(-8.43 - 2.4 \ln(\frac{Tu}{100}))^2 Tu}, \tag{3.33}$$

The new contribution g is then defined as:

$$g(H, Re_\theta) = \begin{cases} 0, & r \leq 0 \\ A(3r^2 - 2r^3), & 0 < r < 1 \\ A, & r \geq 1 \end{cases} \tag{3.34}$$

$$r = \frac{1}{B}\left(\frac{Re_\theta}{Re_{\theta onset}} - 1\right) + \frac{1}{2}, \tag{3.35}$$

$$A = 0.1,$$

$$B = 0.3.$$

A very large fictitious growth rate g is introduced as Re_θ approaches $Re_{\theta onset}$. A smooth procedure is also applied to alleviate potential numerical problems. Once this "rapid" growth rate activates, transition onset will occur within 10 boundary layer thicknesses. In Drela[13], $Re_{\theta onset}$ is given based on the empirical relation from Abu-Ghannam and Shaw[2], while in the present work a more recent and better

empirical relation from Langtry[30] is used:

$$Re_{\theta onset} = \begin{cases} \left(1173.51 - 589.428Tu + \frac{0.2196}{Tu^2}\right) F(\lambda_\theta), & Tu \leq 1.3 \\ 331.5(Tu - 0.5658)^{-0.671} F(\lambda_\theta), & Tu > 1.3 \end{cases} \tag{3.36}$$

where λ_θ is another pressure gradient parameter:

$$\lambda_\theta = \frac{\theta^2}{\nu} \frac{du_e}{dx}, \tag{3.37}$$

and

$$F(\lambda_\theta) = \begin{cases} 1 - (-12.986\lambda_\theta - 123.66\lambda_\theta^2 - 405.689\lambda_\theta^3)\, e^{-\left(\frac{Tu}{1.5}\right)^{1.5}}, & \lambda_\theta \leq 0 \\ 1 + 0.275(1 - e^{-35\lambda_\theta}) e^{-\frac{Tu}{0.5}}, & \lambda_\theta > 0 \end{cases} \tag{3.38}$$

Figure 3-9 shows the predicted $Re_{\theta onset}$ by different empirical relations.

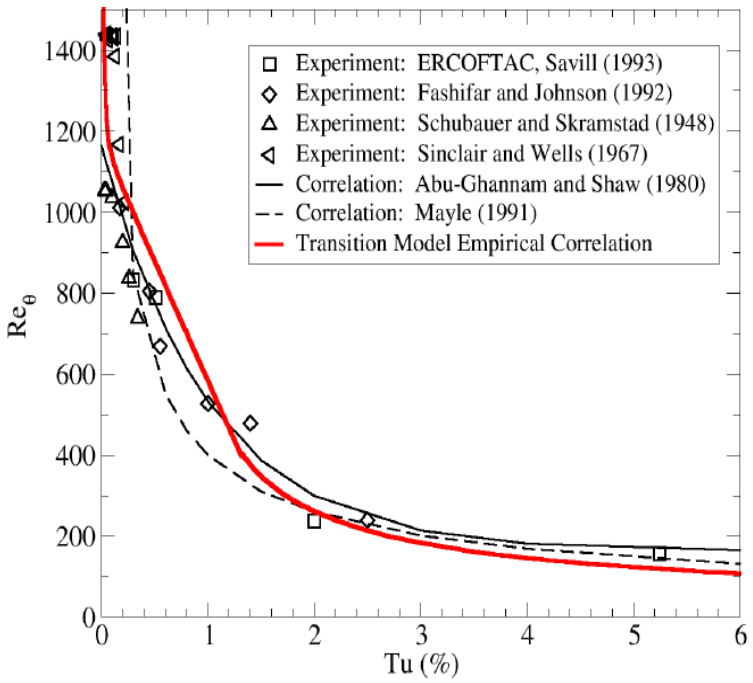

Figure 3-9: Comparison of different empirical relations for $Re_{\theta onset}$ with experiments[30].

For numerical robustness the pressure gradient parameter, the free-stream turbulence

level and $Re_{\theta onset}$ should be limited as follows:

$$\begin{aligned} -0.1 \leq & \lambda_\theta \leq 0.1, \\ & Tu \geq 0.027, \\ & Re_{\theta onset} \geq 20. \end{aligned}$$

In adverse pressure gradients and/or small Tu, the g function does not activate before the original amplification function which causes a growth in N, while in favorable pressure gradients and/or large Tu, the g function dominates. This mimics the dominance of the bypass transition mechanism in the former situation, and the T-S-wave mechanism in the latter situation. Nevertheless, in the former situation, the g function cannot be exactly zero and moves the transition onset point upstream. In order to reduce the effect of double counting, g is set to be zero when $Tu < 0.8$.
Drela[13] argues that it is better to let the empirical relation of $Re_{\theta onset}$ be dependent on H as the dependency on λ_θ may lead to diverging Re_θ and $Re_{\theta onset}$ towards the transition location and the onset of transition will jump downstream during iteration. No significant effect is observed by the present author. It is probably because in the present work the edge velocity u_e is prescribed. If a viscous-inviscid interaction scheme is coupled and u_e is resolved together with other integral parameters, the empirical relation could be ill-posed and changes have to be made. It can be done by using Thwaites $H - \lambda_\theta$ relation:

$$\lambda_\theta = \frac{0.058(H-4)^2}{H-1} - 0.068. \tag{3.39}$$

Equation (3.30) completes the system of equations for steady laminar boundary layer. It becomes:

$$\frac{\partial \mathbf{G}(\mathbf{u})}{\partial x} = \mathbf{S}(\mathbf{u}), \tag{3.40}$$

with:

$$\mathbf{u} = \begin{bmatrix} H \\ \theta \\ N \end{bmatrix}, \quad \mathbf{G}(\mathbf{u}) = \begin{bmatrix} u_e\theta \\ u_e H^*\theta \\ N \end{bmatrix}, \tag{3.41a}$$

$$\mathbf{S}(\mathbf{u}) = \begin{bmatrix} \frac{C_f}{2}u_e - \theta\,(H+1)\,\frac{\partial u_e}{\partial x} \\ C_D u_e - 2H^*\theta\frac{\partial u_e}{\partial x} \\ (\frac{\partial N}{\partial Re_\theta}\frac{dRe_\theta}{dx} + \frac{\partial N}{\partial Tu}\frac{dTu}{dx}) \times RFAC + \frac{g(H,Re_\theta)}{\theta} \end{bmatrix}. \tag{3.41b}$$

When $N = N_{crit}$, the onset of transition is triggerd and the equations will switch to the intermittency model. The unsteady formulation will be introduced in Section 3.2.3.

3.2.2 The intermittency model

The intermittency model is used to predict the flow in the transition region. Emmons(1951) first characterized transition as an eruption of turbulent spots[30]. Since then, others have investigated the intermittent behavior of the flow across the transitional region as the turbulent spots convect downstream in the boundary layer. This has led to the concept of "intermittency" which is a measure of the probability that a given point is located inside the turbulent region. The intermittency factor is the fraction of time during which the flow over any particular point P on the surface is turbulent and given by Emmons[15] as:

$$\gamma(P) = 1 - \exp\left(-\int\int\int_R g(P_0)dx_0dy_0dt_0\right). \tag{3.42}$$

The integral represents the sum of turbulent spot production, $g(P_0)$, over a volume defined by all points P_0 in an $x-y-t$ space that are sources of turbulent spots that will pass over the point P. γ varies between zero and one. When $\gamma = 0$, the flow is completely laminar and when $\gamma = 1$, the flow is fully turbulent. For intermediate values, the flow is transitional. For a boundary layer flow related quantity f, we can write:

$$f = (1-\gamma)f_L + \gamma f_T, \tag{3.43}$$

where f_L is its local laminar value and f_T is its local fully turbulent value.
Over the years, many intermittency models have been proposed. They can be put

into two main categories: algebraic (prescribed) intermittency models and intermittency models based on additional transport equations. Although more recent efforts are mainly focused on models based on additional transport equations for intermittency (such as Suzen and Huang[46], Langtry[30] and Walters and Cokljat[56]), as argued by Praisner and Clark[39], it is inadvisable to stack any intermittency model for transitional region upon another correlation for transition onset since each relation must have its own attendant uncertainty. The present author still feels that a separate algebraic intermittency model is more suitable for this particular work for a number of reasons. First of all, as far as the author knows, almost all the universal intermittency models more or less affect the fully laminar boundary layer before and the fully turbulent boundary layer after the transition region (results can be seen in Chapter 5). Secondly, van Ingen[54] states that in practice, many two-dimensional incompressible airfoil cases for example, which are the eventual focus of the present work, the transition length is very narrow so that even a "transition point" can be defined rather than a transition region. Drela[11] also argues that the transition region itself does not appear to significantly affect the overall development of the boundary layer. While in many turbomachinery applications, transition may affect the whole boundary layer significantly, the author believes in the present framework, it is more appropriate to focus more on the laminar and turbulent region. Last but not least, almost all intermittency models based on universal transport equations at present require some boundary layer parameters which are not able to get in integral boundary layer formulation and the separate intermittency model is more easy to implement.

Therefore, the algebraic intermittency model from Solomon et al[45] is chosen. It is also based on the turbulent spot theory of Emmons[15] and the concentrated breakdown hypothesis of Dhawan and Narasimaha[10] which assumes that all the turbulent spots are generated at the onset of transition x_t. The intermittency factor γ is defined by:

$$\gamma = \begin{cases} 1 - \exp\left(\frac{-(x-x_t)^2 n_s \sigma}{U_\infty}\right), & x \geq x_t \\ 0 \qquad\qquad\qquad\qquad\quad , & x < x_t \end{cases}, \tag{3.44}$$

where n_s is the spot generation rate (the number of spots per unit length, per unit time generated at x_t) and σ is the spot propagation parameter. It is appropriate to introduce a nondimensional breakdown parameter N_s:

$$N_s = \frac{n_s \sigma \theta_t^3}{\nu}, \tag{3.45}$$

where θ_t is the momentum thickness at the onset of transition. The present model is

based on experimental data from Gostelow et al[21]. The correlations for the variation of spot spreading angle α and propagation parameter σ with pressure gradient parameter λ_θ given by Gostelow are:

$$\sigma = 0.03 + (0.37/(0.48 + 3.0\exp(52.9\lambda_\theta))), \tag{3.46}$$

$$\alpha = 4 + (22.14/(0.79 + 2.72\exp(47.63\lambda_\theta))), \tag{3.47}$$

which clearly shows that both parameters vary markedly with the pressure gradient, especially when $\lambda_\theta < 0$. In this study, more realistic correlations for both of the parameters are given by the present author with some odd data points omitted:

$$\sigma = 0.0346116 + (0.341481/(0.48 + 2.95154\exp(64.729\lambda_\theta))), \tag{3.48}$$

$$\alpha = 3.62473 + (22.14/(0.79 + 1.95965\exp(65.4597\lambda_\theta))), \tag{3.49}$$

See Figure 3-10 and 3-11 for the comparison of Gostelow's correlations with the present ones.

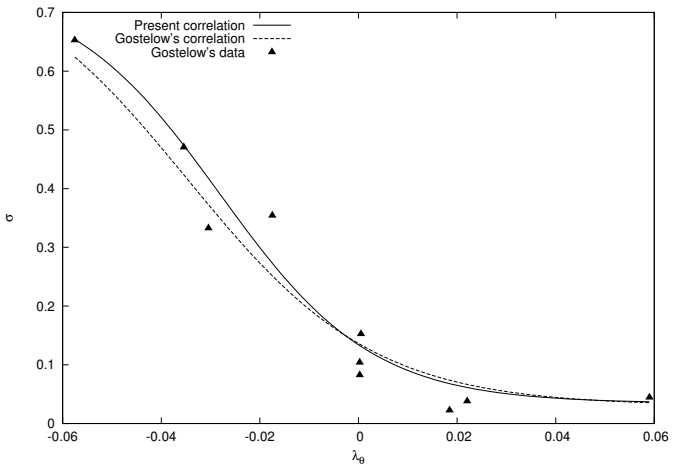

Figure 3-10: Turbulent spot propagation correlation compared with Gostelow's data[21].

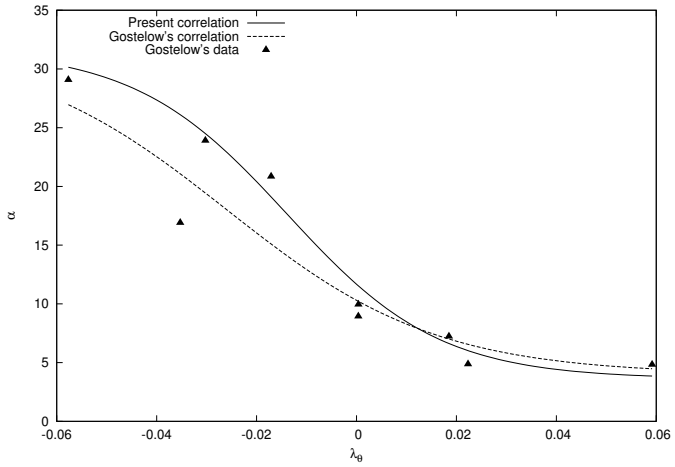

Figure 3-11: Turbulent spot spreading angle correlation compared with Gostelow's data[21].

Ideally the correlations should also take into account the free-stream turbulence level gradient and Re_θ. However, the available data are too sparse to make a meaningful correlation. This causes unsatisfactory prediction of the transition regions for some cases with rather complex flow conditions (see Chapter 5 for the results). The intermittency factor can be written as:

$$\gamma = 1 - \exp\left[-n_s \int_{x_t}^{x} \frac{\sigma}{\tan(\alpha)} \left(\frac{dx}{u_e}\right) \int_{x_t}^{x} \tan(\alpha) dx\right], \tag{3.50}$$

with α and σ obtained from equation (3.48) and (3.49) using the local value of λ_θ inside the transition region and n_s given by the correlations of N_s at the onset point of transition:

$$N_s = \begin{cases} 0.86 \times 10^{-3} \exp(2.134\lambda_{\theta_t} \ln(Tu_t) - 59.23\lambda_{\theta_t} - 0.564 \ln(Tu_t)), & \lambda_{\theta_t} \leq 0 \\ N_0 \times \exp(-10\sqrt{\lambda_{\theta_t}}), & \lambda_{\theta_t} > 0 \end{cases}, \tag{3.51}$$

where N_0 is the value of N_s at $\lambda_{\theta_t} = 0$. This formulation allows variations both in spot convection velocities and spot inception rate with pressure gradient. It can be seen from Figure 3-12 and 3-13 that this method provides better results than a variety of previous models.

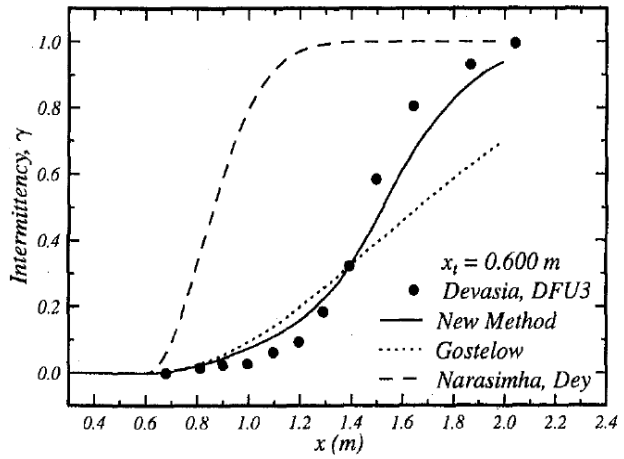

Figure 3-12: Devasia case DFU3: intermittency distributions[45].

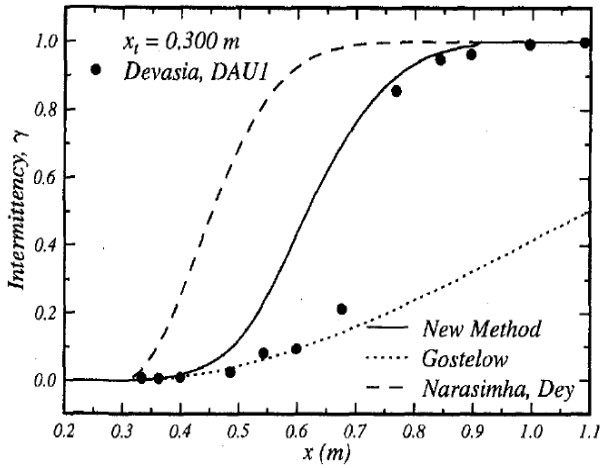

Figure 3-13: Devasia case DAU1: intermittency distributions[45].

In practice, as the amplification factor N reaches its critical value N_{crit}, the intermittency model is switched on. The system of equations for laminar boundary layers does not change but the integral boundary layer parameters are given by:

$$H^* = (1-\gamma)H_L^* + \gamma H_T^*, \tag{3.52}$$

$$C_f = (1-\gamma)C_{fL} + \gamma C_{fT}, \tag{3.53}$$

$$C_D = (1-\gamma)C_{DL} + \gamma C_{DT}. \tag{3.54}$$

When γ reaches 1 (in practice 0.9999 is used to avoid numerical problems), the intermittency model is switched off and the boundary layer is considered fully turbulent.

3.2.3 Unsteady transition modeling

For unsteady boundary layers, the starting mind is that N becomes dependent on time too:

$$N(x,t) = N(Re_\theta(x,t), Tu(x,t)), \tag{3.55}$$

$$\frac{\partial N}{\partial x} = (\frac{\partial N}{\partial Re_\theta}\frac{\partial Re_\theta}{\partial x} + \frac{\partial N}{\partial Tu}\frac{\partial Tu}{\partial x}) \times RFAC, \tag{3.56}$$

$$\frac{\partial N}{\partial t} = (\frac{\partial N}{\partial Re_\theta}\frac{\partial Re_\theta}{\partial t} + \frac{\partial N}{\partial Tu}\frac{\partial Tu}{\partial t}) \times RFAC. \tag{3.57}$$

As neither analytical formulation nor empirical relation for $\frac{\partial Tu}{\partial t}$ is available in literature, this term will be neglected in the present work. Therefore, the third governing equation (3.30) in the laminar system becomes:

$$\frac{\partial N}{\partial t} + \frac{\partial N}{\partial x} = \left(\frac{\partial N}{\partial Re_\theta}(\frac{\partial Re_\theta}{\partial x} + \frac{\partial Re_\theta}{\partial t}) + \frac{\partial N}{\partial Tu}\frac{dTu}{dx}\right) \times RFAC + \frac{g(H, Re_\theta)}{\theta}. \tag{3.58}$$

As far as known by the present author, most models predicting transition onset for unsteady boundary layers in literature are purely based on empirical relations for $Re_{\theta onset}$ (i.e.[30], [39]). Other researchers such as Drela[14] directly modify the steady transition models for unsteady boundary layers. All of those methods enjoy success to some extent. The only effort in developing a real unsteady transition model is reported in a series of publications from DLR and TU Braunschweig (Windte et al.[59], Krumbein et al.[28]), where an unsteady version of the full e^N method is presented.

Recall equation (3.2), here we have the unsteady mean flow:

$$u(x,y,t) = u_m(y,t) + u'(x,y,t), \tag{3.59a}$$

$$v(x,y,t) = v'(x,y,t), \tag{3.59b}$$

$$P(x,y,t) = P_m(x,t) + P'(x,y,t). \tag{3.59c}$$

It is assumed that u_m is weakly dependent on t which means that it only changes slowly with time. Furthermore, the frequency of a single disturbance wave is much larger than frequencies in the time-dependent mean flow u_m, $T_{mean} \gg T_{disturb}$. The streamfunction $\psi(x,y,t)$ remains unchanged:

$$\psi(x,y,t) = \phi(y)e^{i(\alpha x - \beta t)}, \tag{3.5}$$

However, it is not suitable any more to assume β to be real for unsteady flow because both temporal and spatial amplification exist. From Gaster[18], the relation between temporal amplification and spatial amplification is given by:

$$-\alpha_i = \frac{\beta_i}{v_g}, \tag{3.60}$$

where the group velocity v_g:

$$v_g = \frac{\partial \beta_r}{\partial \alpha_r} = \frac{dx}{dt}, \tag{3.61}$$

representing the velocity of energy transport of a single wave mode. Although this relation is strictly valid only in the vicinity of the curve of neutral stability given by $\beta_i = 0$ because it was derived for very small amplification rates, it could be shown by numerical experiments that it yields sufficiently good approximations also for larger amplification rates[28]. Recall the definition of spatial amplification rate (3.14), together with equation (3.61) we have:

$$n(x) = \int_{x_0}^{x} -\alpha_i(\tilde{x})d\tilde{x} = \int_{x(t_0)}^{x(t)} \beta_i(\tilde{x}(t))\frac{d\tilde{x}}{v_g(\tilde{x}(\tilde{t}))} = \int_{t_0}^{t} \beta_i(\tilde{t})d\tilde{t} = n(x(t)) = n(t), \tag{3.62}$$

for the spatial interval $\Delta x = x - x_0$ or the time interval $\Delta t = t - t_0$. Then, it can be further derived as:

$$\begin{aligned} n(x(t+\Delta t)) &= n(x(t)) + \Delta n(x(t+\Delta t)) = n(x) + \Delta n(x(t) + \Delta x) \\ &= n(x) + \Delta n(x + v_g \Delta t) = n(x) + \int_{t}^{t+\Delta t} \beta_i(\tilde{t})d\tilde{t} \\ &\approx n(x) + \beta_i(t+\Delta t)\Delta t + \mathcal{O}((\Delta t)^2), \end{aligned} \tag{3.63}$$

where the integral is replaced by a simple approximation which is considered accurate enough for small time steps Δt. Figure 3-14 shows the distribution of amplification rate n of an unstable disturbance that experiences a time-dependent change while it is convected in stream-wise direction by the group velocity. Therefore, this scheme can be used for the computation of n in an unsteady mean flow[28].

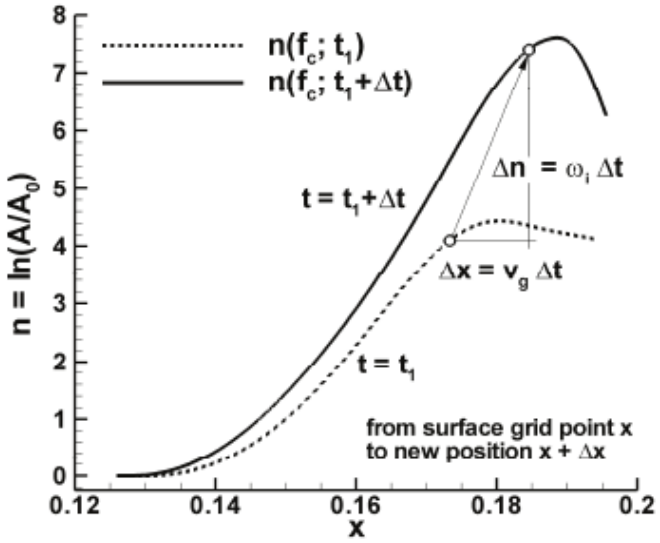

Figure 3-14: Time evolution of an amplification rate in an unsteady mean flow while the flow passes the stream-wise distance Δx during the time interval Δt. [28]

In order to obtain the new value of n at time $t + \Delta t$, it should be interpolated back to the surface grid points. This can be done by a simple linear interpolation (see Figure 3-15).

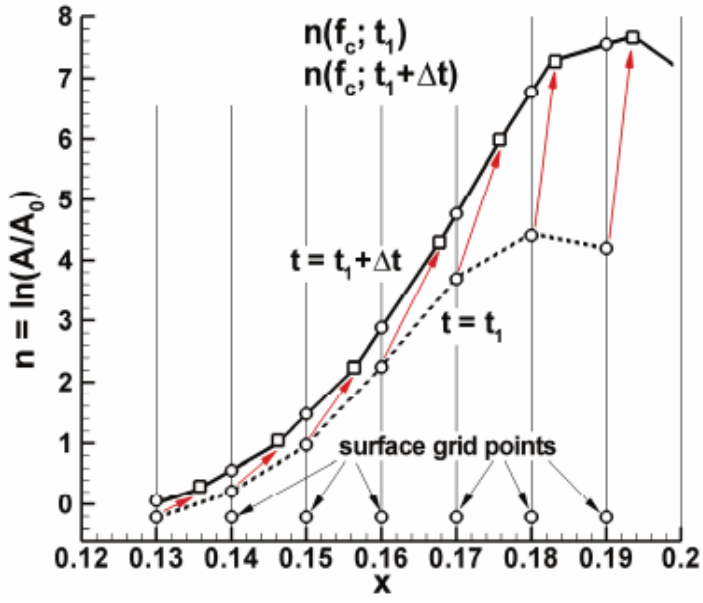

Figure 3-15: Interpolation of the new amplification rate curve back to the surface grid points. [28]

For unsteady boundary layer flow simulations, not only the locally most amplified wave mode for every fixed frequency but also all the other waves need to be taken

into consideration because they can become dominant during the progress of the unsteady flow. Therefore, at every physical time step, a new range of frequencies needs to be adapted and for every frequency in this range, the most amplified wave mode is determined and the amplification factor N can be calculated.
Due to the limit of resource, and the fact that we need a computationally robust algorithm in an design code, the full e^N method is not used for the present work. However, equation (3.63) and equation (3.58) strongly resemble each other. Rearranging (3.63) gives:

$$\frac{n(x(t+\Delta t)) - n(x(t))}{\Delta t} = \beta_i = -\alpha_i v_g = -\alpha_i \frac{dx}{dt}. \tag{3.64}$$

For the simplified e^N method, $-\alpha_i$ can be denoted by $\frac{\partial N}{\partial x}$. That means for unsteady flow, equation (3.58) actually simplifies the temporal amplification rate in the same way as the original simplified e^N method simplifying the spatial amplification rate. Therefore, the author believes that the use of equation (3.58) to predict unsteady transition is justified. However, it is pointed out by Bongers[5] that the simplified e^N method is unable to cope with damping of the T-S waves which is very likely to occur in unsteady boundary layers. Therefore, the current model has limited applicability and the use of the full unsteady e^N method is necessary to have generally applicable model. This evaluation is left as a recommendation for future research.
In practice, if we directly use $\frac{\partial Re_\theta}{\partial t}$, it will lead to a nonconservative system, which is unable to be solved within the framework of the present study. Empirical relations for $\frac{\partial Re_\theta}{\partial t}$ are also unavailable. It is therefore approximated in the following way:

$$\frac{\partial Re_\theta}{\partial t} = \frac{Re_\theta(t+\Delta t) - Re_\theta(t)}{\Delta t} + \mathcal{O}((\Delta t)^2). \tag{3.65}$$

The system of equations for laminar unsteady boundary layer is finally given by:

$$\frac{\partial \mathbf{F}(\mathbf{u})}{\partial t} + \frac{\partial \mathbf{G}(\mathbf{u})}{\partial x} = \mathbf{S}(\mathbf{u}), \tag{2.26}$$

with:

$$\mathbf{u} = \begin{bmatrix} H \\ \theta \\ N \end{bmatrix}, \quad \mathbf{F}(\mathbf{u}) = \begin{bmatrix} H\theta \\ \theta(H+1) \\ N \end{bmatrix}, \quad \mathbf{G}(\mathbf{u}) = \begin{bmatrix} u_e\theta \\ u_e H^*\theta \\ N \end{bmatrix}, \tag{3.66a}$$

$$\mathbf{S}(\mathbf{u}) = \begin{bmatrix} \frac{C_f}{2}u_e - \theta\,(H+1)\,\frac{\partial u_e}{\partial x} - \frac{H\theta}{u_e}\frac{\partial u_e}{\partial t} \\ C_D u_e - 2H^*\theta\frac{\partial u_e}{\partial x} - 2\frac{\theta}{u_e}\frac{\partial u_e}{\partial t} \\ \left(\frac{\partial N}{\partial Re_\theta}(\frac{\partial Re_\theta}{\partial x} + \frac{\partial Re_\theta}{\partial t}) + \frac{\partial N}{\partial Tu}\frac{dTu}{dx}\right) \times RFAC + \frac{g(H,Re_\theta)}{\theta} \end{bmatrix}. \tag{3.66b}$$

The unsteady transition model is used to simulate several simple unsteady cases, the results will be shown in Chapter 5.

Chapter 4

Numerical method

Traditionally IBL equations have been discretised using the Finite Difference Method (FDM) (e.g. Drela[11]) or the Finite Element Method (FEM) (e.g. Nishida[33]). However, since the governing equations are hyperbolic, it is a natural choice to use the Discontinuous Galerkin method (DG). With this approach a solution can be obtained with high order of spatial and temporal accuracy, especially for geometrically complex domains. In this chapter, the idea of the space-time DG method and the procedure for discretization will be introduced. Gaussian quadrature rules are used for numerical integration and will also be explained.

4.1 Space-time Discontinuous Galerkin method

The DG method is a type of FEM with relaxed continuity requirements on the source and test space. It can be seen as a combination of the classical FEM and the Finite Volume Method (FVM), where the space basis functions and test functions are close to that of the classical FEM but it also shares the local conservation property of a FVM. The DG method has several favorable properties (see Özdemir[37], Atkins and Shu[3]). First of all, it is a local method, which means the discretisation in each element in the computational domain is only dependent on the direct neighbors irrespective of the order of accuracy of the approximation, giving much more freedom in meshing complex domains comparing to FDM. Furthermore, the DG method allows for local grid and (more importantly) order refinement. This property, which is very difficult to realize in continuous FEM, improves the accuracy and efficiency to a great extent. On the other hand, it can be noted that the DG method with constant basis functions is in fact the FVM. For higher order DG the accuracy of the method is nearly completely determined by the accuracy of the expansion of the solution in each element and only very mildly on the approximation of the numerical fluxes.

Therefore, use can be made of very simple approximations to the numerical fluxes that would not lead to acceptable results for the FVM.

The IBL equations are a set of non-linear hyperbolic equations including source terms. However, explicit time integration methods such as the Runge-Kutta (RK) multi-stage method lead to a singularity problem at initialization for unsteady IBL systems. This singularity problem at initialization is caused by the fact that the boundary layer thickness is initially equal to zero, which leads to infinite C_f and C_D and thus an infinite initial source vector. The problem can of course be solved by giving a very small but non-zero initial condition for the boundary layer thickness but this introduces an error in solution. Additionally, the time step for explicit integration of the system is bounded by a stability condition which is very restrictive for higher order basis functions. For these reasons, an implicit time-integration method is preferred. More details can be found in van den Boogaard[48]. The implicit space-time DG method (STDG) takes the time as an additional dimension, using the same discretization technique for the approximation of both spatial and temporal derivatives. This makes the unsteady one-dimensional IBL equations actually resemble a physical two-dimensional system. Effectively a steady two-dimensional problem in a space-time coordinate system is solved.

Implicit numerical methods commonly solve for all spatial degrees of freedom (DOF) in a single vector for every instant of time. The resulting numerical system will require inversion of matrices of large dimension, which is computationally expensive. An upwind flux and a stepping approach in temporal direction is used since time is one-directional. A similar approach for the spatial direction is highly favorable but can not be applied if the flow is multi-directional such as two-dimensional separated flows and general three-dimensional flows with cross-flow. Nevertheless, as mentioned in Section 2.3, the present work is not able to solve separated flow due to the absence of an external inviscid flow solver. This allows the upwind flux to be used also in the spatial domain as attached flow is one-directional. For multi-directional flows, a higher order numerical flux is required. Details can also be found in van den Boogaard[48].

4.1.1 Discretization

Recall the IBL system (both laminar and turbulent) (2.26)

$$\frac{\partial \mathbf{F}(\mathbf{u})}{\partial t} + \frac{\partial \mathbf{G}(\mathbf{u})}{\partial x} = \mathbf{S}(\mathbf{u}). \tag{2.26}$$

Assuming the number of PDEs in the system is P, all elements $u^d(x,t)$ with $d \in (1,P)$ in the solution vector $\mathbf{u}$ are part of the function space $\mathcal{U} \equiv \mathcal{V} \times \mathcal{T}$ with x-dependent

function space $\mathcal{V}$ and t-dependent function space $\mathcal{T}$ and $\mathbf{u} \in \mathcal{U}^P$.

For a space-time DG discretization, both space and time domain are tessellated, resulting in space-time elements $\omega_{k,n}$, where k is the index of elements in spatial direction and n is the index of elements in temporal direction. Transforming all elements to a more convenient computational element $\mathcal{K} : \{\xi \in (-1,1), \tau \in (-1,1)\}$ in the computational space-time domain with ξ and τ representing the computational space domain and the computational time domain, and mapping the solution to a function space on this domain:

$$\xi = f^{\mathcal{K}}(x), \tag{4.1}$$

$$J_x^{\mathcal{K}} = \frac{\partial \xi}{\partial x} = \frac{\partial f^{\mathcal{K}}(x)}{\partial x}, \tag{4.2}$$

$$\tau = g^{\mathcal{K}}(t), \tag{4.3}$$

$$J_t^{\mathcal{K}} = \frac{\partial \tau}{\partial t} = \frac{\partial g^{\mathcal{K}}(t)}{\partial t}, \tag{4.4}$$

$$u^d(x,t) \in \mathcal{U} \rightarrow u^d(\xi,\tau) \in \hat{\mathcal{U}}, \tag{4.5}$$

where f is a linear transformation for the spatial coordinates with a positive constant Jacobian J_x and g is a linear transformation for the temporal coordinates with a positive constant Jacobian J_t. All the elements $\mathcal{K}$ are attached to their neighboring elements which means the flux exiting the element $\mathcal{K}_{k,s}$ through the boundary ($\xi = 1, \tau$) will enter element $\mathcal{K}_{k+1,s}$ through the boundary ($\xi = -1, \tau$).

Introducing the operator $\mathbf{L}$ gives:

$$\mathbf{L}(\mathbf{u}) = J_t \frac{\partial \mathbf{F}(\mathbf{u})}{\partial \tau} + J_x \frac{\partial \mathbf{G}(\mathbf{u})}{\partial \xi} - \mathbf{S}(\mathbf{u}) = 0. \tag{4.6}$$

A weak formulation can be obtained, by multiplying the operator $\mathbf{L}$ with a test function vector, $\mathbf{V} \in \hat{\mathcal{U}}^P$, followed by an integration over the computational space-time element:

$$\mathbf{R}(\mathbf{u}) = \int_{\mathcal{K}} \mathbf{L}(\mathbf{u}) \mathbf{V} d\mathcal{K} = 0. \tag{4.7}$$

Introducing local finite element approximations, $u_h^d \in \hat{\mathcal{U}}_h$ for all unknown variables

$u^d \in \hat{\mathcal{U}}$ for each element $\mathcal{K}$, where:

$$\hat{\mathcal{U}}_h = B_i \subset \hat{\mathcal{U}}, \tag{4.8}$$

$$u_h^d(\xi,\tau) = \sum_{i=0}^{M_p-1} u_i^d B_i(\xi,\tau), \quad \forall d \in (1,P), \tag{4.9}$$

where B_i are a combinaton of ξ-dependent basis functions and τ-dependent basis functions and M_p is the total number of linear independent basis function projections used in the approximation of u^d, given by[38]:

$$M_p = \frac{1}{dim}\prod_{i=1}^{dim}(p+i), \tag{4.10}$$

where dim is the number of dimension in the basis functions (i.e. for two-dimensional problem $dim = 2$) and p is the maximum degree of the polynomials used for the basis functions for each dimension. The test functions can also be written as:

$$v_h^e(\xi,\tau) = \sum_{i=0}^{M_p} v_i^e B_i(\xi,\tau), \quad \forall e \in (1,P), \tag{4.11}$$

where e is the index for the different equations in the PDE set and therefore also the index for the elements in the test function vector. A total of M_p+1 linear independent test functions are required to project u_h^d on the basis functions. Therefore, taking the v_i^e in equation (4.11) to be the Kronecker delta function will lead to the most obvious linear independent test functions:

$$(v_h^e)_j = B_j(\xi,\tau), \quad \forall e \in (1,P), \forall j \in (0,M_p). \tag{4.12}$$

The residual vector defined in (4.7) has $(M_p+1)\times P$ elements R_j^e:

$$\begin{aligned} R_j^e(\mathbf{u}) &= \int_{\mathcal{K}} \mathbf{L}^e(\mathbf{u}) B_j d\mathcal{K} \\ &= \int_{\mathcal{K}} \left(J_t \frac{\partial \mathbf{F}^e}{\partial \tau} + J_x \frac{\partial \mathbf{G}^e}{\partial \xi} - \mathbf{S}^e) \right) B_j d\mathcal{K} = 0. \end{aligned} \tag{4.13}$$

Using chain rule to differentiate $\mathbf{L}^e B_j$ gives:

$$\begin{aligned} R_j^e = & \int_{\mathcal{K}} \left(\frac{\partial \mathbf{F}^e J_t B_j}{\partial \tau} - \mathbf{F}^e \frac{\partial J_t B_j}{\partial \tau} \right) d\mathcal{K} \\ & + \int_{\mathcal{K}} \left(\frac{\partial \mathbf{G}^e J_x B_j}{\partial \xi} - \mathbf{G}^e \frac{\partial J_x B_j}{\partial \xi} \right) d\mathcal{K} \\ & - \int_{\mathcal{K}} \mathbf{S}^e B_j d\mathcal{K} = 0, \quad \forall \mathcal{K}. \end{aligned} \tag{4.14}$$

Applying Green's theorem gives a system without any differential term depending on the solution vector:

$$\begin{aligned} R_j^e = & \int_{\widehat{\Omega}} \int_{\partial \widehat{I}} \widehat{\mathbf{F}}^e \widehat{n}_\tau J_t B_j da d\xi \\ & + \int_{\widehat{I}} \int_{\partial \widehat{\Omega}} \widehat{\mathbf{G}}^e \widehat{n}_\xi J_x B_j da d\tau \\ & - \int_{\mathcal{K}} \left(\mathbf{F}^e \frac{\partial J_t B_j}{\partial \tau} + \mathbf{G}^e \frac{\partial J_x B_j}{\partial \xi} + \mathbf{S}^e B_j \right) d\mathcal{K} = 0, \quad \forall \mathcal{K}, \end{aligned} \tag{4.15}$$

where the function spaces $\widehat{\Omega} : \xi \in (-1, 1)$, $\widehat{I} : \tau \in (-1, 1)$ and a is the coordinate along the boundary $\partial\mathcal{K}$ of element $\mathcal{K}$. $\widehat{\mathbf{F}}^e$ and $\widehat{\mathbf{G}}^e$ are respectively the temporal and spatial numerical fluxes for the e-th equation. Recall the size of the computational domain, it leads to:

$$\begin{aligned} R_j^e = & \int_{-1}^{1} \left[\left(\widehat{\mathbf{F}}^e J_t B_j \right)_{\tau=1} - \left(\widehat{\mathbf{F}}^e J_t B_j \right)_{\tau=-1} \right] d\xi \\ & + \int_{-1}^{1} \left[\left(\widehat{\mathbf{G}}^e J_x B_j \right)_{\xi=1} - \left(\widehat{\mathbf{G}}^e J_x B_j \right)_{\xi=-1} \right] d\tau \\ & - \int_{-1}^{1} \int_{-1}^{1} \left(\mathbf{F}^e \frac{\partial J_t B_j}{\partial \tau} + \mathbf{G}^e \frac{\partial J_x B_j}{\partial \xi} + \mathbf{S}^e B_j \right) d\tau d\xi = 0, \end{aligned} \tag{4.16}$$

which is the general definition for the residuals in every element of the space-time domain.

The upwind numerical flux is chosen to solve element by element. Assuming upwind directions in space and time are in positive direction, the numerical traces in equation (4.16) are:

$$\widehat{\mathbf{F}}^{k,n}|_{\tau=-1} = \mathbf{F}^{k,n-1}|_{\tau=1}, \tag{4.17}$$

$$\widehat{\mathbf{F}}^{k,n}|_{\tau=1} = \mathbf{F}^{k,n}|_{\tau=1}, \tag{4.18}$$

$$\widehat{\mathbf{G}}^{k,n}|_{\xi=-1} = \mathbf{F}^{k-1,n}|_{\xi=1}, \tag{4.19}$$

$$\widehat{\mathbf{G}}^{k,n}|_{\xi=1} = \mathbf{F}^{k,n}|_{\xi=1}. \tag{4.20}$$

Since the space-time system is first order in space and first order in time, one boundary condition for each dimension is needed, which leads to a boundary condition and a initial condition. In practice, flux boundary conditions $\mathbf{F}_0$ and $\mathbf{G}_0$ for both dimensions are used.

4.1.2 Numerical integration

The integral in equation (4.16) can actually be integrated exactly, the scheme is currently under development at ECN[43]. However, for the present work, a simpler numerical integration method, namely Gaussian quadrature rules (GQR) is used. For the integration of a function $f(\xi)$ in the domain $\xi \in (-1, 1)$, using the GQR method based on Legendre polynomials, with n positions ξ_i on the interval of ξ are taken. These evaluations are given a weight, ω_i, representing the range of ξ for which this value is constant. The approximation of the integral is given by:

$$\int_{-1}^{1} f(\xi) d\xi \simeq \sum_{i=1}^{n} f(\xi_i)\omega_i. \tag{4.21}$$

The discrete sum has $2n$ unknowns ξ_i, ω_i, which can be solved by taking f to be a polynomial of degree $d = 2n - 1$. GQR method works with the inverse principle by given ξ_i and ω_i and the integration can be approximated as accurate as if $f(\xi)$ is a polynomial of degree $2n - 1$. Quadrature points ξ_i and quadrature weights ω_i are given in Table 4.1

For integration over a surface, it can be given by:

$$\int_{-1}^{1}\int_{-1}^{1} f(\xi, \tau) d\xi d\tau \simeq \sum_{i=1}^{n}\sum_{j=1}^{n} f(\xi_i, \tau_j)\omega_i\omega_j. \tag{4.22}$$

See Figure 4-1 for the quadrature points for 2D integrations. In order to have an approximation to the integral of the required accuracy, the choice of quadrature points

n should result in an integration that is exact for polynomials of at least order $2p$:

$$2p \leq d = 2n - 1 \rightarrow n \geq p + \frac{1}{2}. \tag{4.23}$$

Thus $p + 1$ points are chosen for each integration. Equation (4.16) becomes:

$$\begin{aligned} R_j^e = &\sum_{p=1}^{n_\xi} \left[\left(\widehat{\mathbf{F}}^e J_t B_j \right)_{\tau=1} - \left(\widehat{\mathbf{F}}^e J_t B_j \right)_{\tau=-1} \right] \Bigg|_{\xi_p} \omega_p \\ &+ \sum_{q=1}^{n_\tau} \left[\left(\widehat{\mathbf{G}}^e J_x B_j \right)_{\xi=1} - \left(\widehat{\mathbf{G}}^e J_x B_j \right)_{\xi=-1} \right] \Bigg|_{\tau_q} \omega_q \\ &- \sum_{p=1}^{n_\xi} \sum_{q=1}^{n_\tau} \left(\mathbf{F}^e \frac{\partial J_t B_j}{\partial \tau} + \mathbf{G}^e \frac{\partial J_x B_j}{\partial \xi} + S^e B_j \right) \Bigg|_{\xi_p, \tau_q} \omega_p \omega_q = 0, \end{aligned} \tag{4.24}$$

n	ξ_i	ω_i
1	0	2
2	−0.577350269189626	1
	0.577350269189626	1
3	−0.774596669241483	0.555555555555556
	0	0.888888888888889
	0.774596669241483	0.555555555555556
4	−0.861136311594053	0.347854845137454
	−0.339981043584856	0.652145154862546
	0.861136311594053	0.652145154862546
	0.861136311594053	0.347854845137454

Table 4.1: Points and weights for the Gaussian quadrature rule used by Boogaard[48].

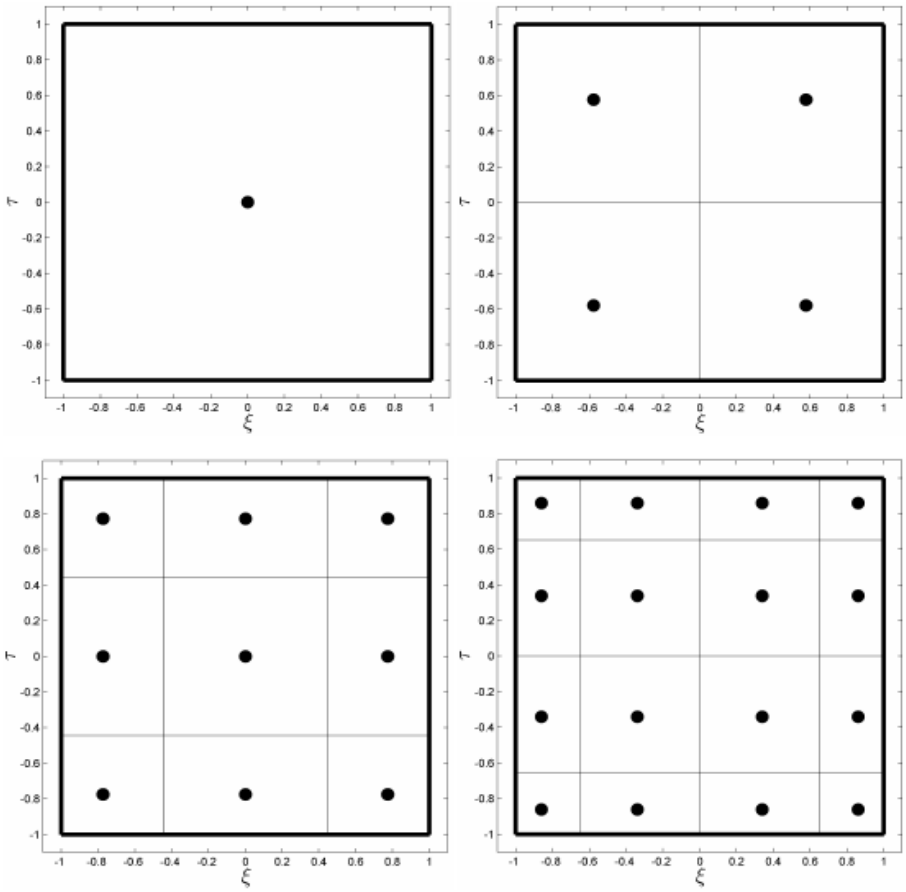

Figure 4-1: Quadrature points for 2D integration as used by Boogaard[48].

4.1.3 Iteration

Newton iteration is used to solve the nonlinear system (4.24). The residual R_j^e is expanded over the ranges of e and j, giving a vector of residual, $\mathbf{R}$. If a Taylor expansion of order 2 is used, then:

$$\mathbf{R}(\mathbf{u}_{it+1}) = \mathbf{R}(\mathbf{u}_{it}) + J(\mathbf{u}_{it})(\mathbf{u}_{it+1} - \mathbf{u}_{it}) + \mathcal{O}\left((\mathbf{u}_{it+1} - \mathbf{u}_{it})^2\right), \tag{4.25}$$

where it is the index of the iterations and the Jacobian matrix J is defined as:

$$J = \frac{\partial \mathbf{R}}{\partial \mathbf{u}} = \frac{\partial \mathbf{R}}{\partial \mathbf{U_h}} \frac{\partial \mathbf{U_h}}{\partial \mathbf{u}} = \frac{\partial \mathbf{R}}{\partial \mathbf{U_h}} B_i. \tag{4.26}$$

The objective is to reduce the norm of the residual vector as much as possible per iteration. In each step the following system is solved:

$$\mathbf{R}(\mathbf{u}_{it}) + J(\mathbf{u}_{it})(\mathbf{u}_{it+1} - \mathbf{u}_{it}) = 0, \tag{4.27}$$

which gives the new approximation of the unknowns $\mathbf{u}_{it+1}$:

$$\mathbf{u}_{it+1} = \mathbf{u}_{it} - J^{-1}(\mathbf{u}_{it})\mathbf{R}(\mathbf{u}_{it}), \tag{4.28}$$

and the error norm of the new iteration is:

$$\epsilon_{it+1} = |\mathbf{R}(\mathbf{u}_{it+1})| = |\mathcal{O}\left((\mathbf{u}_{it+1} - \mathbf{u}_{it})^2\right)|. \tag{4.29}$$

The method will have quadratic convergence if the initial guess is close enough to the solution. For example, if $P = 2$, $M_p = 2$, the Jacobian matrix is given by the following block matrix:

$$J = \begin{bmatrix} \dfrac{\partial R^1}{\partial u^1} & \dfrac{\partial R^1}{\partial u^2} \\ \dfrac{\partial R^2}{\partial u^1} & \dfrac{\partial R^2}{\partial u^2} \end{bmatrix}, \tag{4.30}$$

where each block is given as:

$$\frac{\partial R^e}{\partial u^d} = \begin{bmatrix} \dfrac{\partial R^e_0}{\partial u^d_0} & \dfrac{\partial R^e_0}{\partial u^d_1} & \dfrac{\partial R^e_0}{\partial u^d_2} \\ \dfrac{\partial R^e_1}{\partial u^d_0} & \dfrac{\partial R^e_1}{\partial u^d_1} & \dfrac{\partial R^e_1}{\partial u^d_2} \\ \dfrac{\partial R^e_2}{\partial u^d_0} & \dfrac{\partial R^e_2}{\partial u^d_1} & \dfrac{\partial R^e_2}{\partial u^d_2} \end{bmatrix}. \tag{4.31}$$

4.1.4 Conclusions

Implicit space-time DG requires both an initial condition and boundary conditions to evaluate the fluxes. In fact, application of Newton iteration to find the result in the space-time domain requires an appropriate guess to start the iterative process. If this guess is not chosen wisely the iteration might not converge. A separate iterative

process to find a proper initial guess itself is used to relieve this problem.
The Jacobian matrix presented in this chapter has to be defined every iteration step for every element in both space and time direction and the solution of the next iteration is found using a Gaussian elimination procedure which makes the computation very expensive in terms of CPU time. However, the larger matrix will be extremely sparse, allowing for more efficient solving techniques to be used.
An upwind spatial flux with an implicit time discretization method, like STDG, is recommended for at least the first time-step in calculation boundary layer flow using the IBL equations. However, as mentioned before, the upwind scheme is used for the whole flow domain in the present work becauce of first-order fluxes and inability to solve separation for the present code.
A more detailed description of the numerical method utilized in the present work is present in references [37] and [48].

Chapter 5

Results and discussions

In this chapter results for a number of test cases are presented. The cases considered include boundary layers over flat plates and airfoils for attached flow conditions. Both the modeling of fully turbulent flow and laminar-to-turbulent transition for the IBL equations are validated. Steady flow (by setting the time derivatives in the system to 0) as well as unsteady flow are considered.

It is necessary to point out that the convergence of the numerical method has been assessed before (see Figure 5-1 as an example). More results can be found in van den Boogaard[48]. As the present work does not change the structure of the algorithm or the discretisation, the investigation of convergence is not repeated in the present study and the polynomial order of basis functions P and the amount of cells N are chosen to be high enough to secure accurate results.

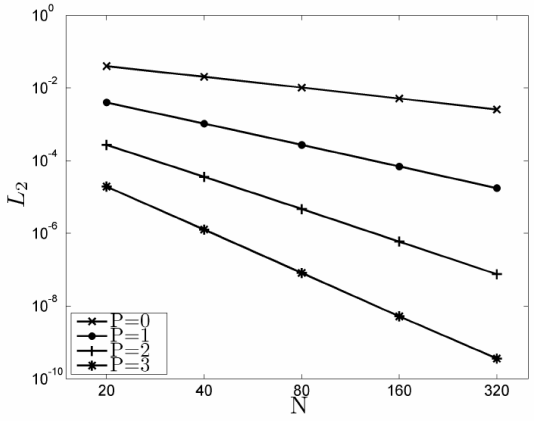

Figure 5-1: L_2 error norms for the steady state solution of the stagnation test case, using laminar IBL. The solution on a mesh with N = 320 and 6th order polynomial basis functions is used as reference solution. Taken from [48].

5.1 Turbulent boundary layers

Test cases are carefully selected such that the whole boundary layer can be considered as turbulent. Simulations are conducted only using turbulent models while laminar IBL model and transition model are skipped. Both IBL methods, the dissipation integral method and the entrainment integral method, as well as the equilibrium model and the non-equilibrium model are assessed.

5.1.1 Flat plate

One of the most straightforward test cases for a boundary layer flow to be modeled with the IBL equations is a boundary layer over a flat plate. The edge velocity for a flat plate is $u_e = U_\infty$, where U_∞ is the free-stream velocity. A variety of experimental data for boundary layers over flat plates can be found in Coles[8], originally presented on the Stanford Conference in 1968. Two test cases are selected for the present study: Flow 1400 with zero pressure gradient from Wieghardt and Tillmann[58] and Flow 1100 with adverse pressure gradient from Ludwieg and Tillmann[32]. See Table 5.1 for the detailed configurations of these two test cases.

Test	u_e	Length(L)	Re_L	Pressure gradient
Flow 1400	33.0m/s	5m	1.0927×10^7	Zero
Flow 1100	$(-3.11645x + 36.1652)$m/s	5m	1.16662×10^7	Adverse

Table 5.1: Flat plate test cases for turbulent models.

Note that for Flow 1100, the edge velocity is a linear fit (see Figure 5-2) to the experimental data presented in [32]. A higher order fit is of course possible but the present author believes that problems will be caused by the possibly too large velocity gradient near the leading edge of the flat plate.
The input for the Flow 1400 simulation is as follows:

Input	Value
Polynomial Order(P)	2
Amount of Cells(N)	200
H_{bound}	1.5
θ_{bound}	1×10^{-4}
$C_{\tau_{bound}}$	1×10^{-3}
$C_{E_{bound}}$	1×10^{-3}

Table 5.2: Input for Flow 1400 simulation.

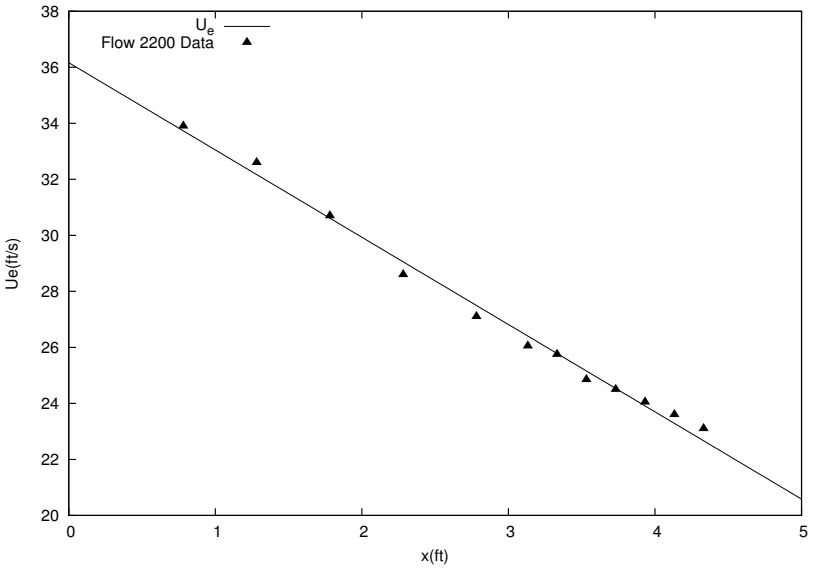

Figure 5-2: Edge velocity of Flow 1100.

The equilibrium model, the non-equilibrium model and the switching model of the two integral methods are tested. The skin friction coefficient C_f can well indicate the properties of the boundary layer and is thus chosen to present the results of the simulations. The complete numerical results of the simulations such as the momentum thickness θ and the shape factor H can be found in Appendix B. The switch criterion is set to $C_f = 0.0015$. However, in this case the critical C_f value is not reached during the simulation. Thus, only the results of the equilibrium model and the non-equilibrium model are presented in Figures 5-3 and 5-4. Note that the simulation time in the unsteady simulation is chosen to be long enough so that the boundary layer may be considered as reaching a steady state. Predictions from Head[24], Ferziger et al.[17] and Das[9] are presented for comparison while data are digitized from White[57].
It can be observed from Figures 5-3 and 5-4 that the equilibrium models indeed perform better for attached flow with low shape factor and zero pressure gradient (or equilibrium flow). In particular, the dissipation integral method with the shear-lag equation provides most unsatisfactory results due to the fact that the $C_{\tau_{EQ}}$ term in the shear-lag equation is calculated by empirical relations and thus the right hand side can hardly vanish.
The input for the Flow 1100 simulation is given by:

Input	Value
Polynomial Order(P)	2
Amount of Cells(N)	200
H_{bound}	1.2
θ_{bound}	1×10^{-3}
$C_{\tau_{bound}}$	5×10^{-4}
$C_{E_{bound}}$	1×10^{-2}

Table 5.3: Input for Flow 1100 simulation.

Only the results of steady simulations are presented in Figure 5-5.
From the results it can be concluded that none of the methods gives a good prediction. This case is rated as one of the "most difficult" in the Stanford Conference (1968) because it is categorized as an equilibrium flow with an adverse pressure gradient and thus none of the models implemented in the current code is suitable for predicting it. The boundary layer is relatively thick and almost certainly contains three-dimensional effects. The pressure gradient parameter β is meant to be constant but the measured value varies significantly. It is noticed that the model which includes the most original differential form of the stress-transport equation (2.46) by Bradshaw and Ferris[6] gives a rather good prediction compared to other methods which should not be too surprising as not many simplifications are applied.

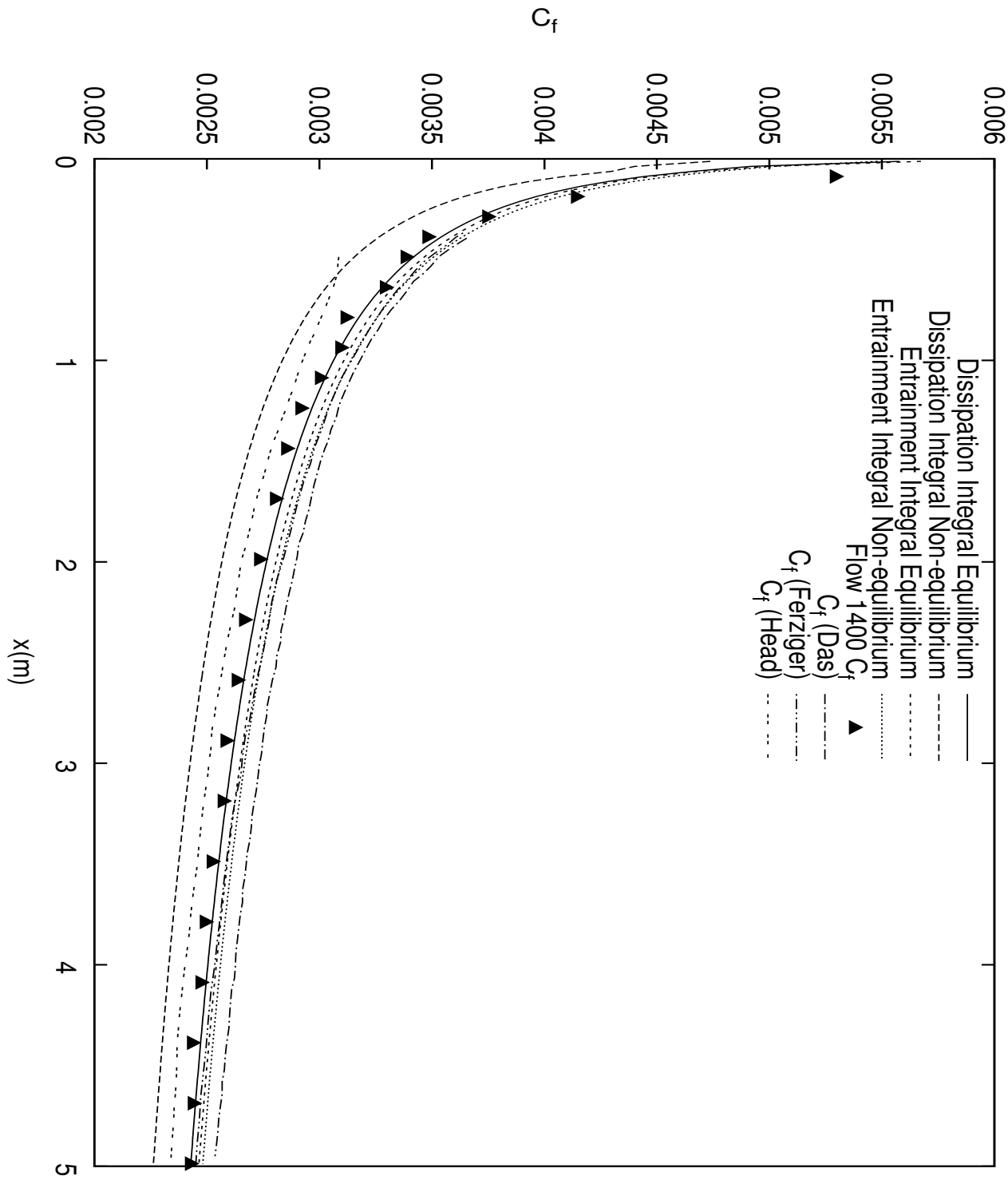

Figure 5-3: Steady simulation of the Flow 1400 (skin friction coefficient).

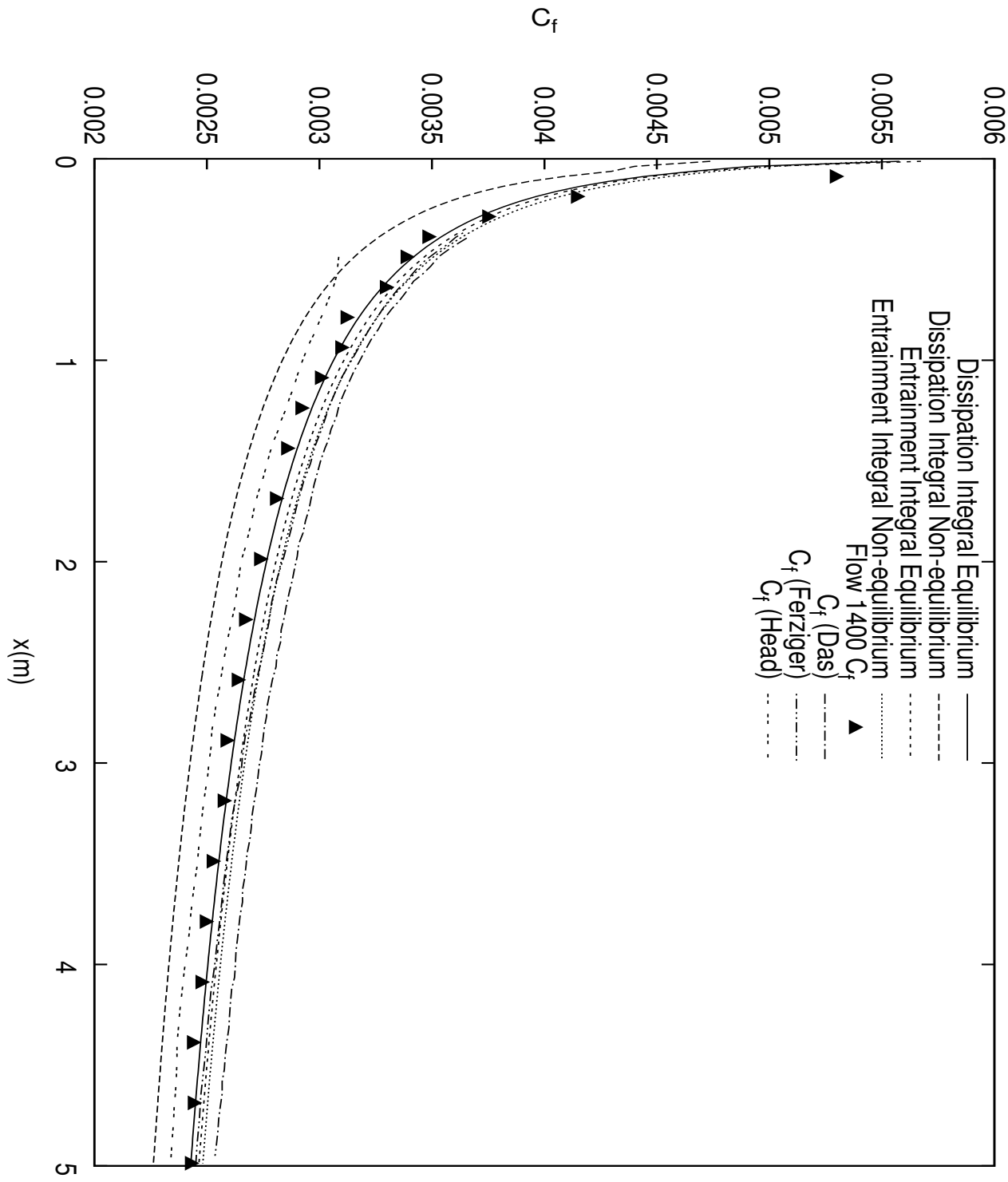

Figure 5-4: Steady simulation of the Flow 1400 (skin friction coefficient).

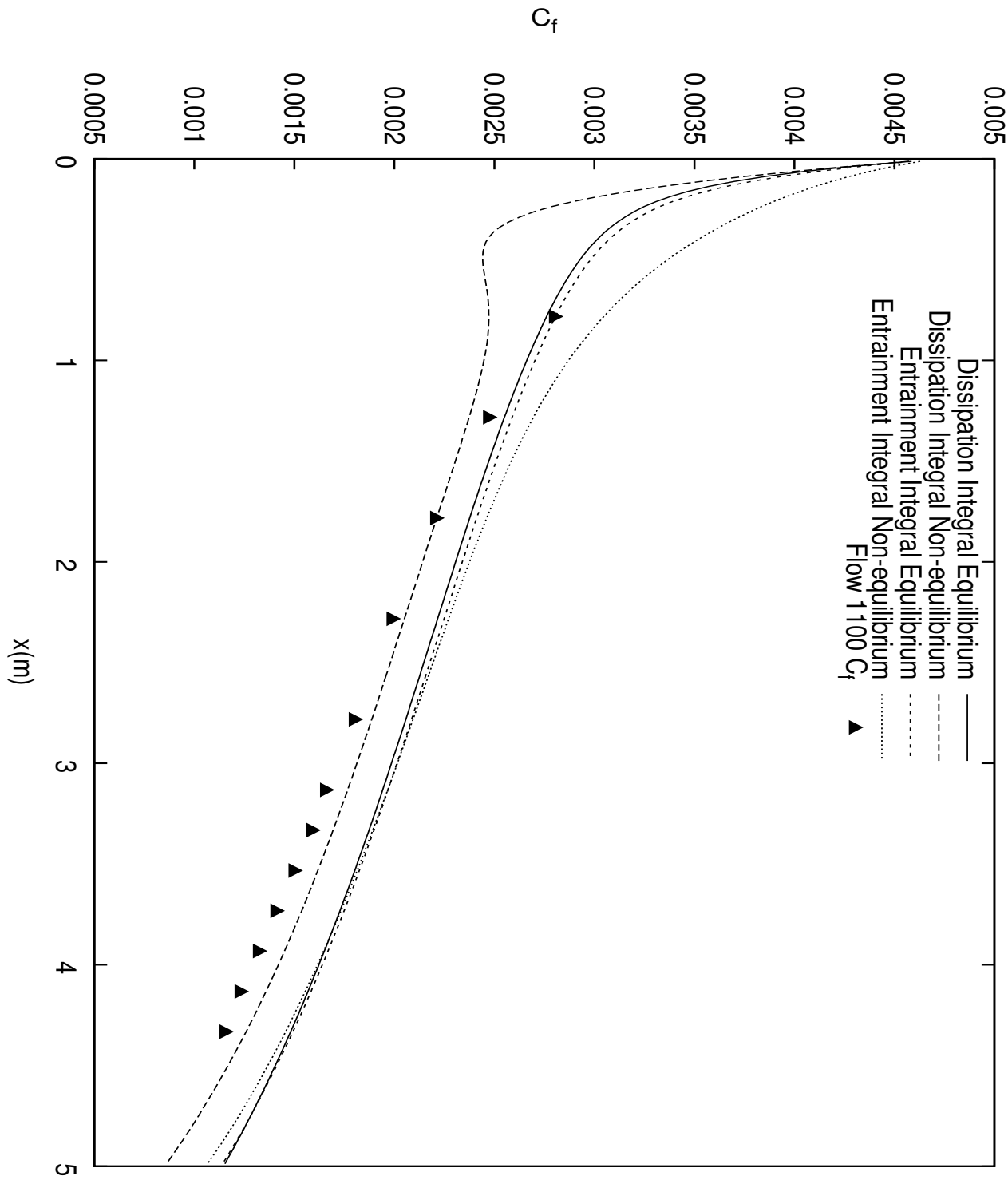

Figure 5-5: Steady simulation of the Flow 1100 (skin friction coefficient).

5.1.2 NACA 0012 Airfoil

In this section, results for the simulation of the boundary layer flow on an airfoil are presented. The well-studied NACA 0012 airfoil with maximum thickness of 12 percent of the chord is chosen. See Table 5.4 for the configuration.

Test case	Airfoil	Chord length(L)	Re_L	Angle of attack(α)
1	NACA 0012	1	6×10^6	0°
2	NACA 0012	1	6×10^6	10°

Table 5.4: NACA 0012 airfoil test cases for turbulent models.

The present code is only able to resolve one side of the airfoil and it is treated as a flat plate by manipulating the prescribed edge velocity u_e. The edge velocity distribution is obtained by running a steady simulation for the particular test case in the widely used airfoil design tool XFOIL[12]. The resulting boundary layer parameters are compared. The set of data obtained from XFOIL for comparison is carefully chosen to make sure the flow is turbulent over the entire computational domain (i.e. the small region near the leading edge is skipped). See Figure 5-6 as an example for the actual simulation region (indicated by the thick red line).

Figure 5-6: Example of the actual simulation region of airfoil test cases.

The input for the two test cases is presented in Table 5.5:

Input	Case 1	Case 2
Polynomial Order(P)	2	2
Amount of Cells(N)	200	200
H_{bound}	1.8	1.8
θ_{bound}	1×10^{-5}	$1(2) \times 10^{-5}$
$C_{\tau_{bound}}$	1×10^{-3}	1×10^{-3}
$C_{E_{bound}}$	1×10^{-2}	1×10^{-2}
Length(L)	0.99121	0.96723

Table 5.5: Input for NACA 0012 turbulent simulation.

Note that in the simulation for Case 2 using the entrainment integral method with the non-equilibrium model, the boundary layer momentum thickness θ_{bound} needs to be reset to 2×10^{-5} due to its boundary value sensitivity. The critical skin friction coefficient is again set to $C_f = 0.00015$. Use of the switch model is optional. Results of steady and unsteady simulations are presented in Figures 5-7 to 5-10.
These airfoil test cases can be considered as flow over a flat plate with a pressure gradient. From the results, we can conclude that the present turbulent model can predict the turbulent boundary layer quite well overall. It is justified to say that although the equilibrium models perform better for attached boundary layers with low shape factor, the non-equilibrium models provide better results for those cases in which the boundary layer is approaching separation.

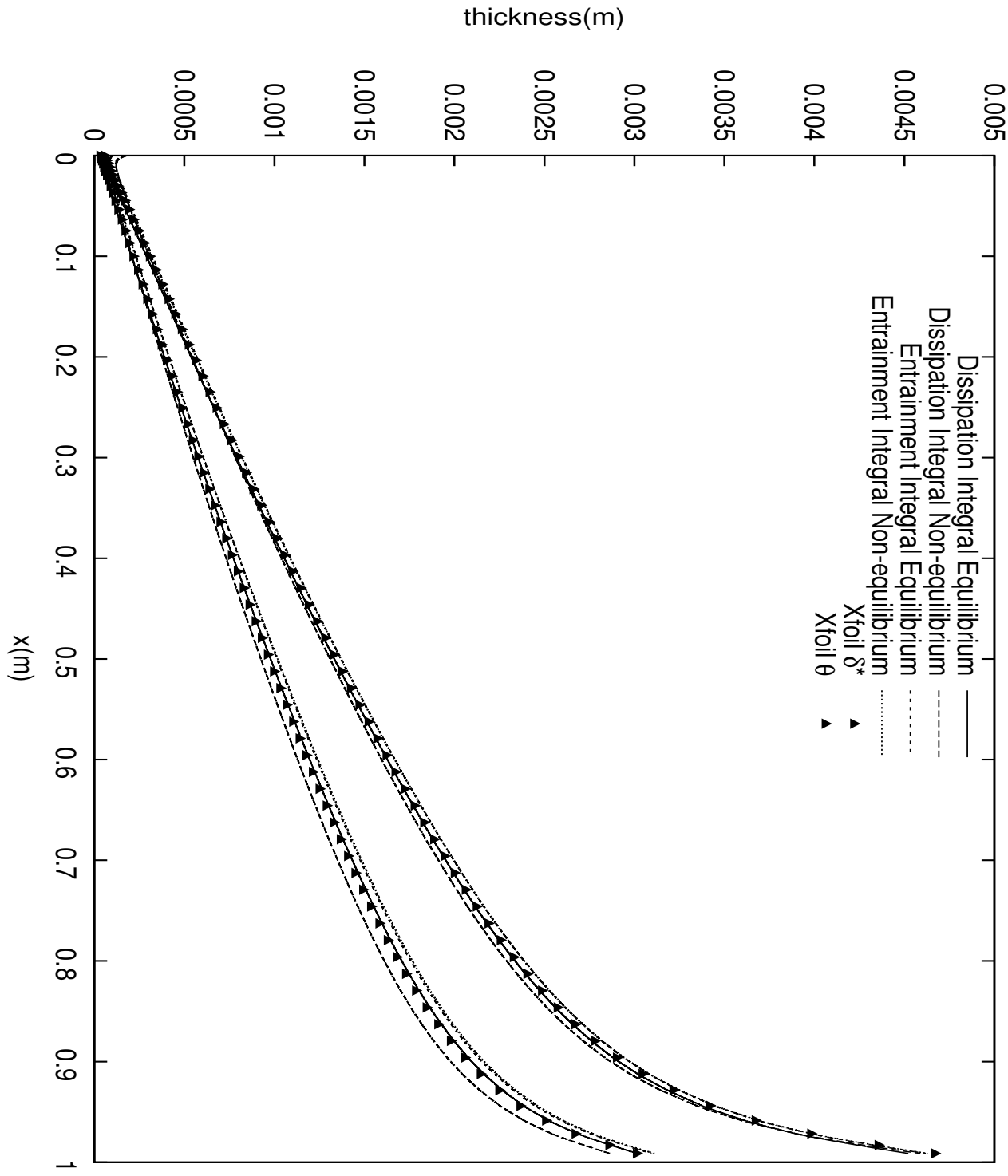

Figure 5-7: Steady simulation of the NACA 0012 $\alpha = 0°$ (momentum thickness and displacement thickness).

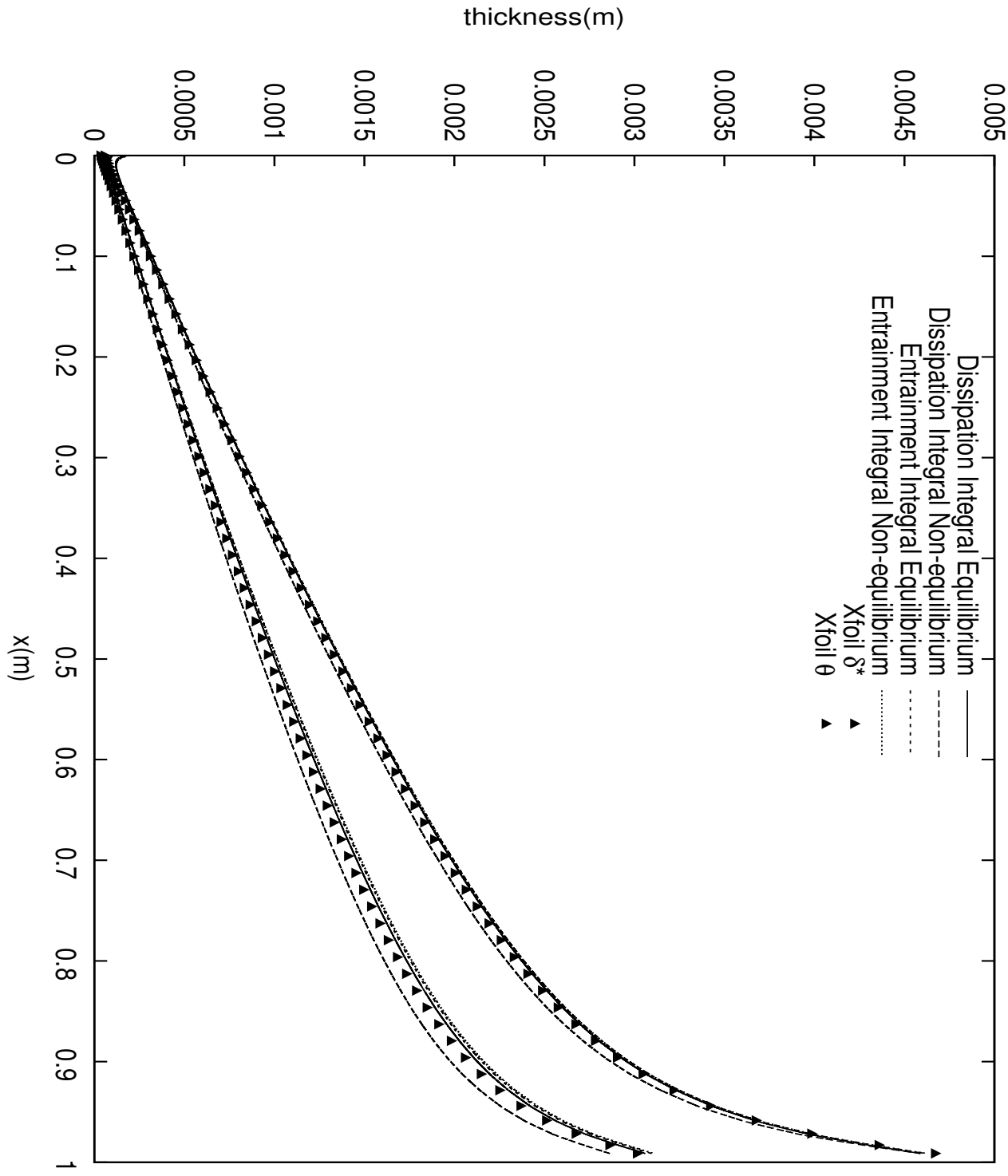

Figure 5-8: Unsteady simulation of the NACA 0012 $\alpha = 0°$ (momentum thickness and displacement thickness).

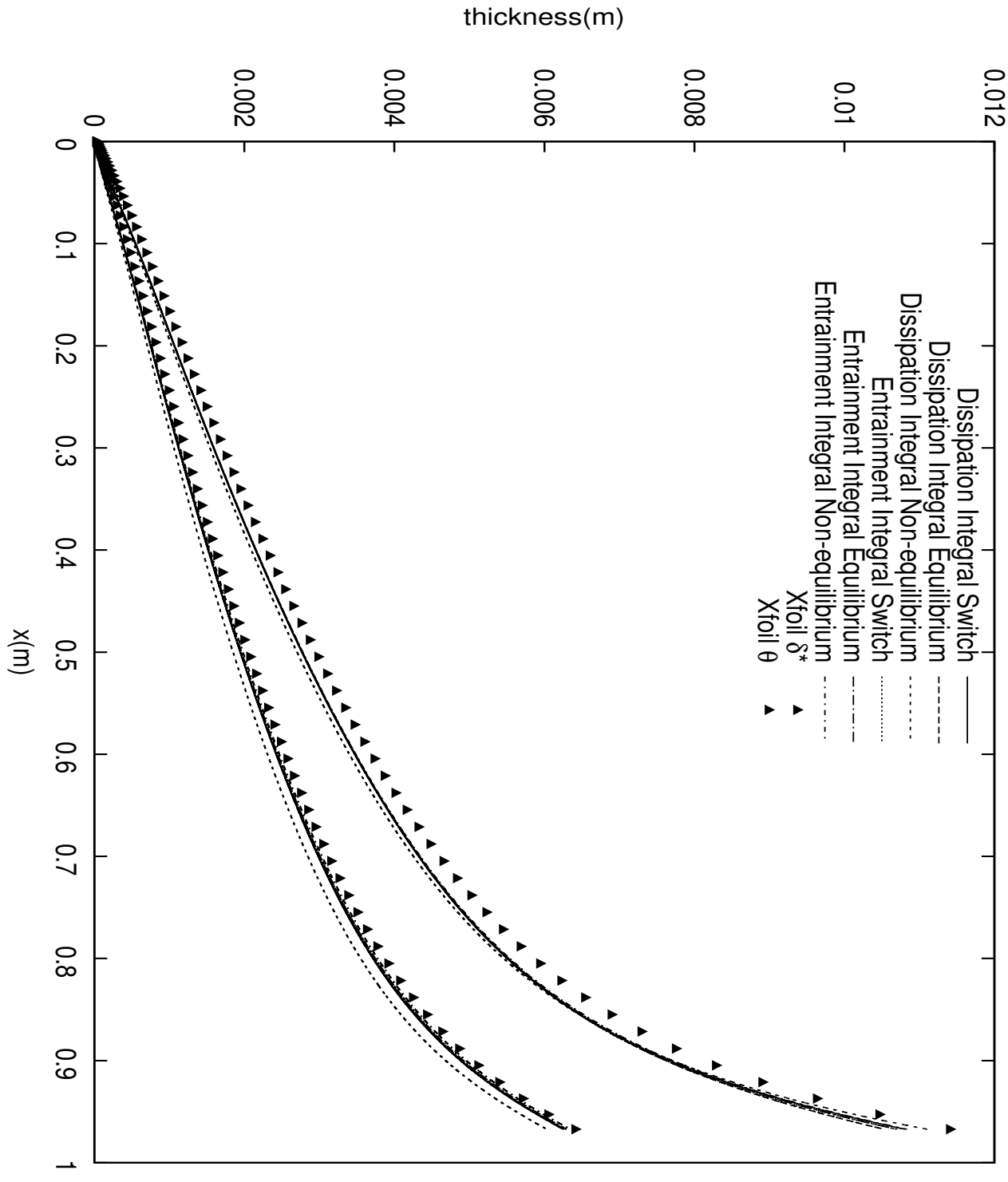

Figure 5-9: Steady simulation of the NACA 0012 $\alpha = 10°$ (momentum thickness and displacement thickness).

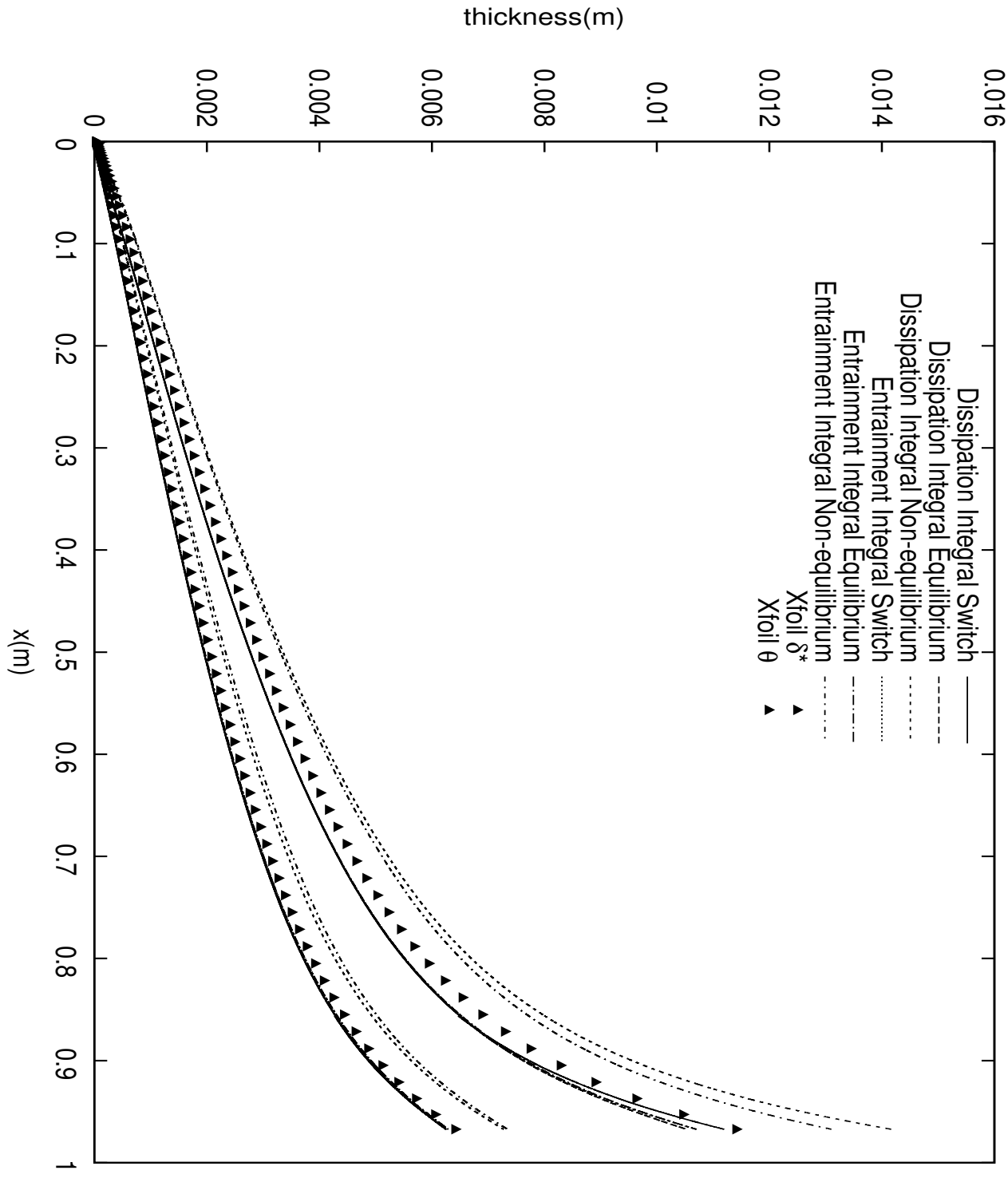

Figure 5-10: Unsteady simulation of the NACA 0012 $\alpha = 10°$ (momentum thickness and displacement thickness).

5.2 Transitional boundary layers

The complete algorithm, including the models of laminar boundary layers, the laminar-to-turbulent transition and the fully turbulent boundary layers, is tested for various cases of transitional flow. Note that for all the test cases below, the equilibrium model with dissipation integral method is used to model the turbulent part of the boundary layer.

5.2.1 Steady models

First of all, a NACA 0012 test case is presented in order to verify the prediction of the correct position of the transition onset and the intermittency model. Still note that only one side of the airfoil is simulated and it is treated as a flat plate with a pressure gradient. Then, the model for predicting the transition onset is further tested by a NLF(1)-046 airfoil case with different angles of attack. After that, several flat plate test cases of natural transition or bypass transition, with/without pressure gradient and varying free-stream turbulence level are validated. All the results are compared with results from simulations and experimental data presented in literature.

NACA 0012 airfoil

The configuration of the test case is given in Table 5.6.

Test case	Airfoil	Chord length(L)	Re_L	Angle of attack(α)
1	NACA 0012	1	1×10^6	0°

Table 5.6: NACA 0012 airfoil test case for transition models.

The input is presented in Table 5.7:

Input	Case 1
Polynomial Order(P)	3
Amount of Cells(N)	400
H_{bound}	2.6
θ_{bound}	1×10^{-4}
$C_{\tau_{bound}}$	1×10^{-3}
Length(L)	0.99121
N_{crit}	9

Table 5.7: Input for NACA 0012 transitional simulation.

Rather than determining N_{crit} by the free-stream turbulence level, here it is directly set as $N_{crit} = 9$ so that results can be compared with results from simulations using XFOIL whose default N_{crit} is 9. Results from Bongers[5] using an improved XFOIL code coupled with the full e^N method are also presented. See Figure 5-11.
We note that the present transition model predicts the transition onset slightly upstream of the prediction from XFOIL but downstream from the location predicted by Bongers. However, the result is still well within the transition prediction uncertainties of e^N method itself. The deviation seen in Figure 5-11b is probably a result of the fact that the present transition model uses a different separate intermittency model and does not apply any techniques for smoothness when switching from the laminar model to the intermittency model. Note that both XFOIL and Bongers use exactly the same intermittency model which is a mathematical smoothing procedure without steady physical background. It can be seen from the XFOIL result in Figure 5-11a that the growth of the momentum thickness near onset of transition actually slows down which is obviously not the case in reality when the boundary layer is approaching separation. Furthermore, there is a discontinuity in the intermittency factor (Figure 5-12d) because the integrals in the intermittency model are approximated rather than evaluated exactly. Above all, the author believes that the transition region itself does not play a very significant role in the whole flow region and the present model is able to well capture the mechanism of the laminar, transitional and turbulent boundary layer.

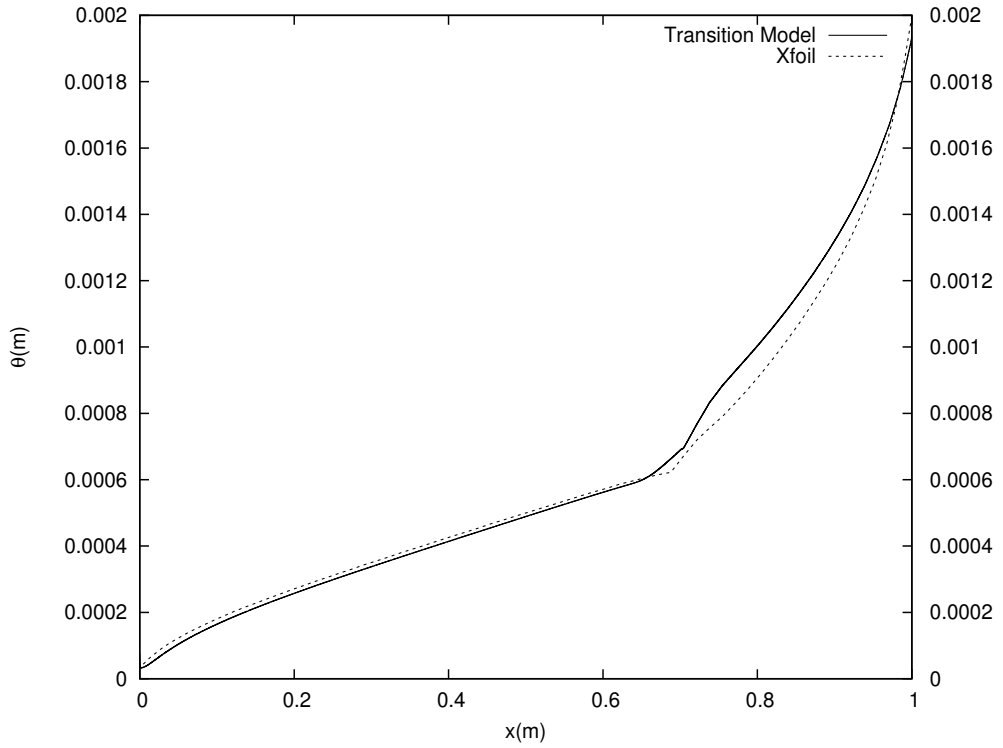

(a) Momentum thickness

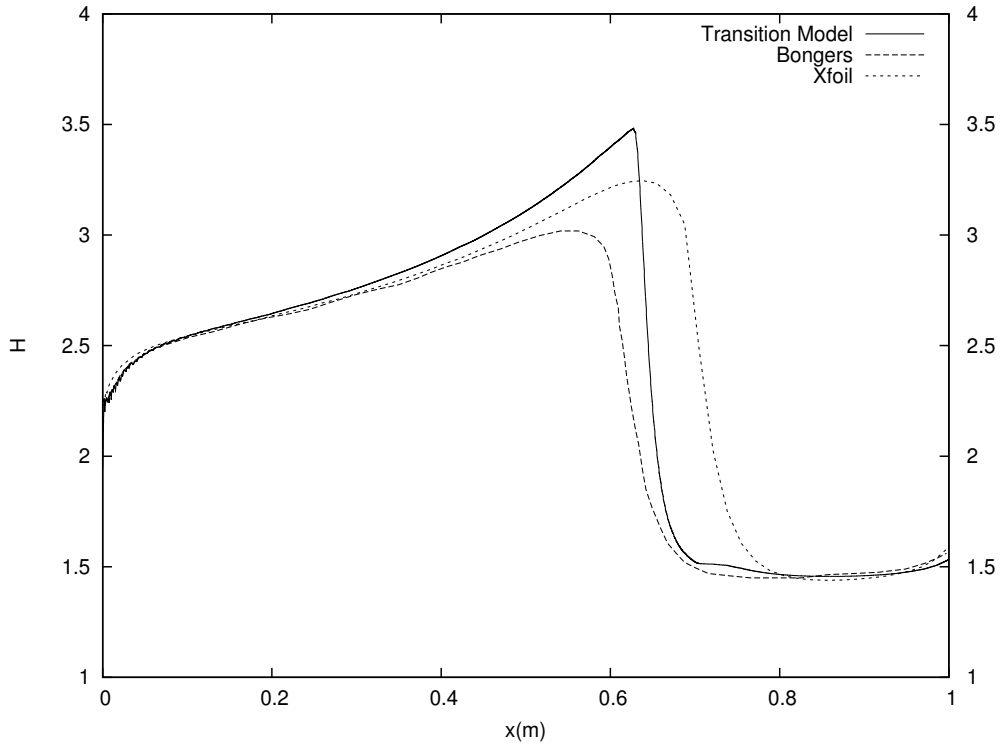

(b) Shape factor

Figure 5-11: Steady simulation of the NACA 0012 transition (1).

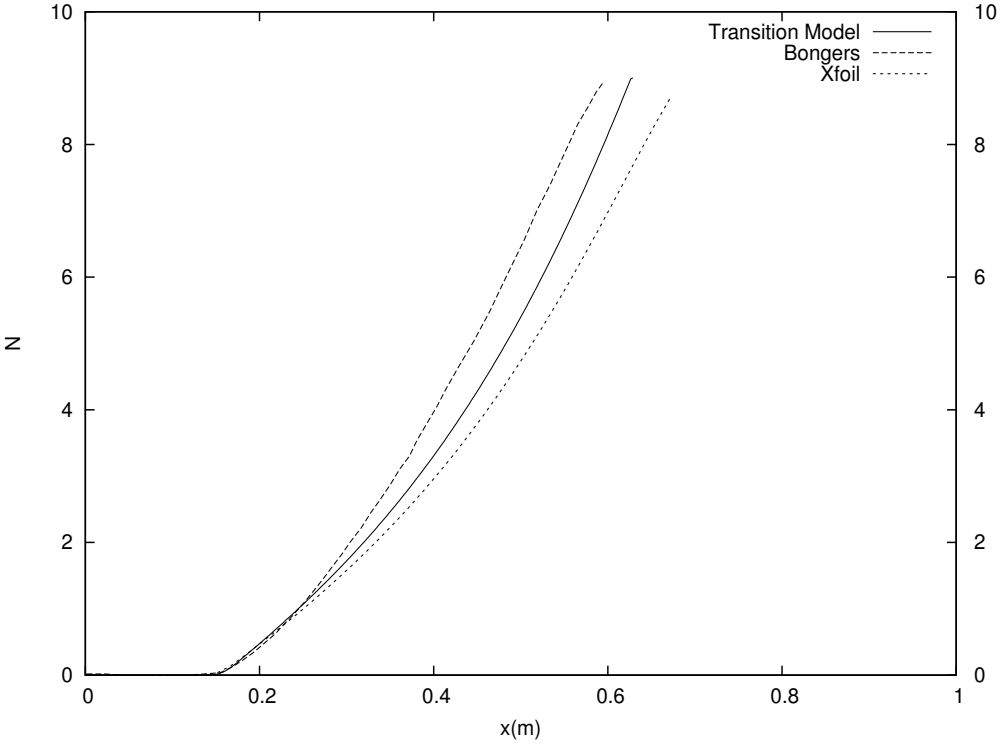

(c) Amplification factor

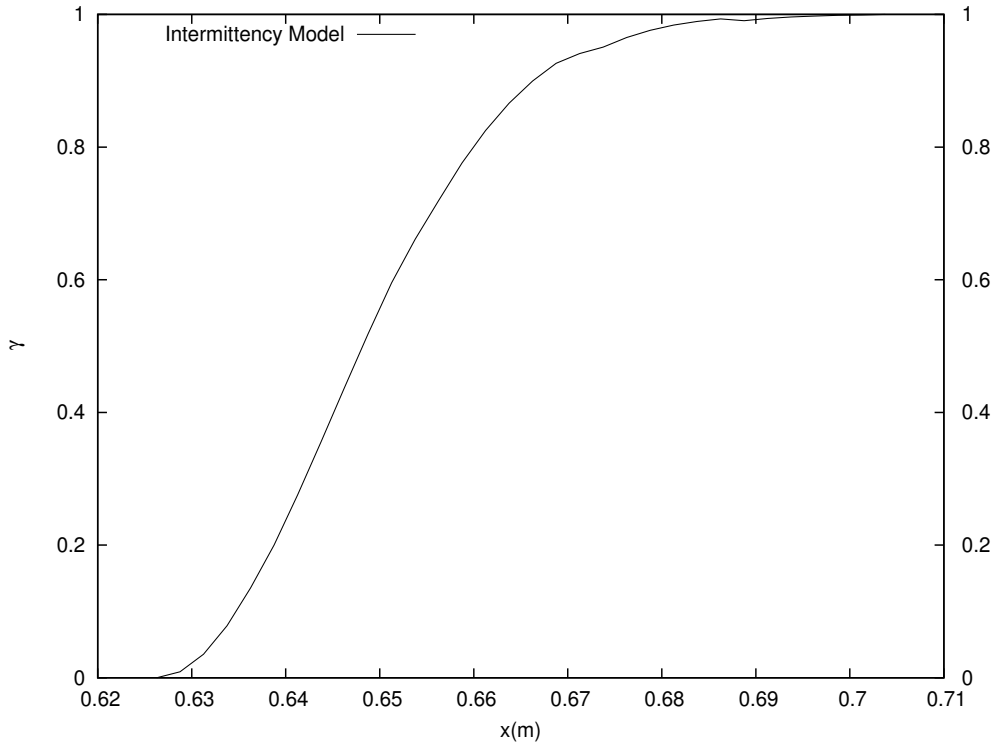

(d) Intermittency factor

Figure 5-11: Steady simulation of the NACA 0012 transition (2).

NLF(1)-046 airfoil

NLF(1)-046 is a (natural) laminar flow airfoil. It is not symmetric, but the upper surface can still be treated as a flat plate (see Figure 5-12 for the shape of the airfoil). The present transition model is used to predict the location of the onset of transition on the upper surface for a range of angles of attack from $-4°$ to $8°$. For angles of attack outside this range, separation will happen and the present model is not applicable. Table 5.8 gives the input parameters for the test case and Figure 5-13 presents the results and a comparison with the results from XFOIL and the AHD criterion from Heister et al.[25].

The edge velocity distribution that is required as input for the transition model is again obtained from running a steady simulation of the test case with different angles of attack in XFOIL. In order to get a very accurate result, the number of panels for the XFOIL simulation is set to 354. From Figure 5-13, we can see that if $N_{crit} = 9$, both XFOIL and the present model predict the transition onset quite downstream, but if N_{crit} is set to 7, it gives results closer to experimental data. This is not surprising because the free-stream turbulence level for this test case is $0.03\% < 0.1\%$ for which an effective free-stream turbulence level needs to be determined and it is normally less than 8 from Figure 3-4.

Airfoil	NLF(1)-046
Polynomial Order(P)	3
Amount of Cells(N)	400
Re_L	4×10^6
H_{bound}	2.2
θ_{bound}	1×10^{-4}
$C_{\tau_{bound}}$	1×10^{-3}
Length(L)	1

Table 5.8: Input for NLF(1)-046 transition onset prediction.

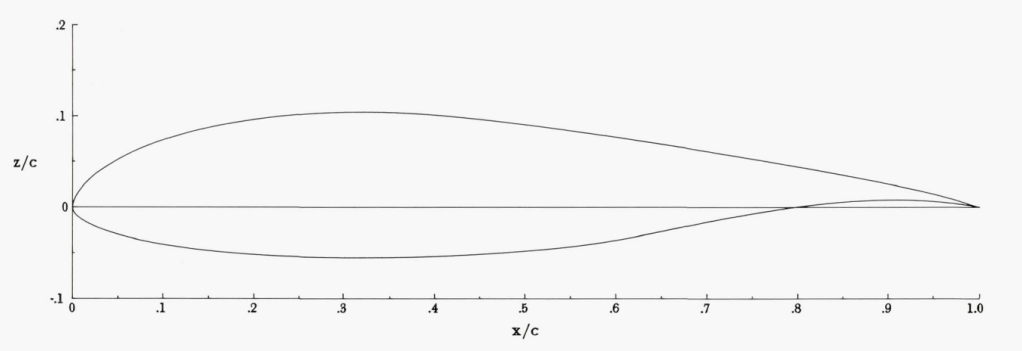

Figure 5-12: NLF(1)-046 airfoil shape.

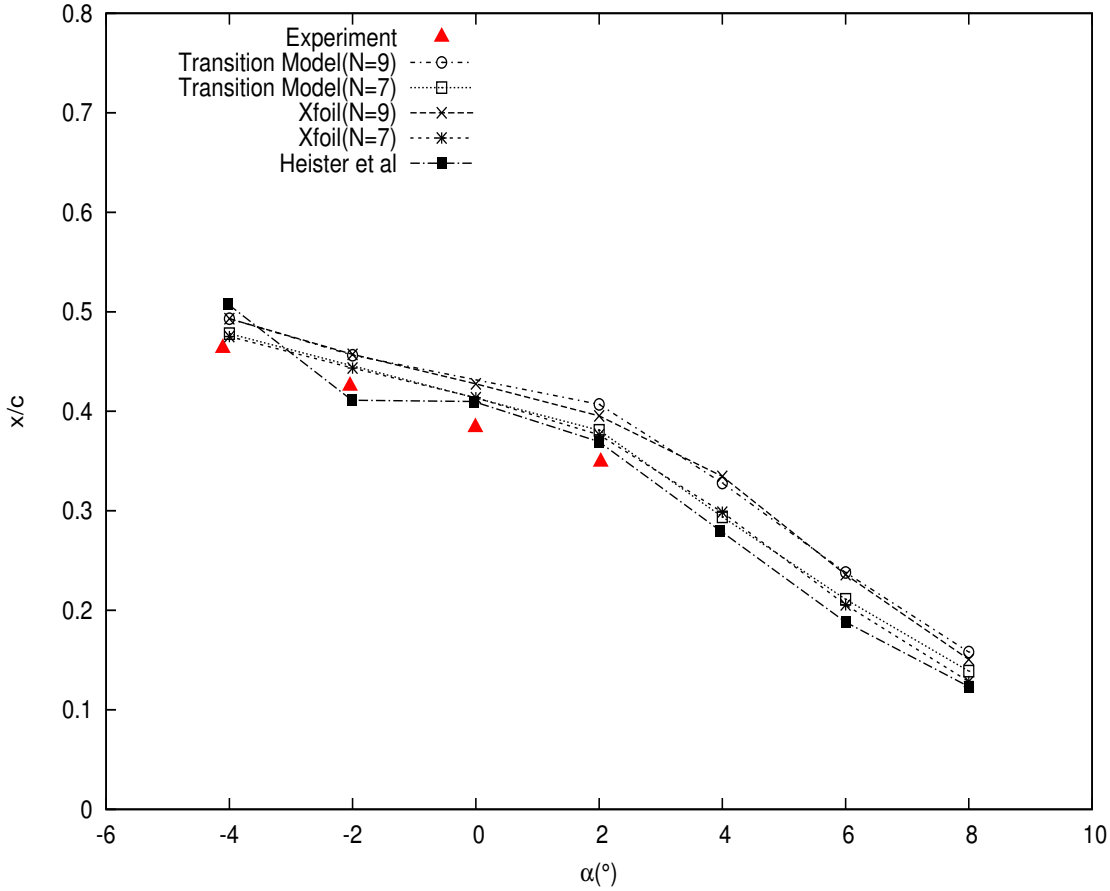

Figure 5-13: Transition onset prediction for NLF(1)-046 airfoil with different angles of attack.

Flat plate cases

Several flat plate test cases are simulated using the present transition model for a range of flow conditions. Experimental data are obtained from Schubauer and Klebanoff[41] and the T3 series test cases[1]. Table 5.9 gives the settings for the test cases and the input parameters are given based on the conditions of different test cases. For test cases with a pressure gradient and varying free-stream turbulence level, the edge velocity u_e and the free-stream turbulence level Tu over the whole flow region are given by high order data fit based on experimental data. Results obtained with the present method are compared with results of simulations from Abu-Ghannam and Shaw[2], Johnson and Ercan[26] and Langtry[30] as well as experimental data.

Test case	S & K	T3A-	T3C3	T3C5
Length(L)	3.6576	1.7	1.7	1.7
Re_L	5.949696×10^6	2.244×10^6	3.94667×10^5	9.52×10^5
Pressure gradient	Zero	Zero	Adverse	Favorable
Free-stream turbulence level	Zero	Varying	Varying	Varying
Transition type	Natural	Natural	Bypass	Bypass

Table 5.9: Flat plate test cases for transition models.

The Schubauer and Klebanoff's flat plate test case is actually a Blasius boundary layer, with constant edge velocity and shape factor in the laminar region. The free-stream turbulence level at the leading edge is given by $Tu = 0.1$ and remains unchanged in the stream-wise direction. The skin friction coefficient C_f over the whole flow region is given in Figure 5-17. It is clear that the present transition model predicts the position of the transition onset and the length of the transition region pretty well.

The T3 series flat plate cases are a set of test cases which are widely used for validating transition models. Among them, T3A- is the only case of natural transition with zero pressure gradient. The free-stream turbulence level at the leading edge is 0.9% and over the whole flow region it is given based on the experimental data (also see Figure 5-14):

$$Tu = 0.205983x^2 - 0.589167x + 0.9. \tag{5.1}$$

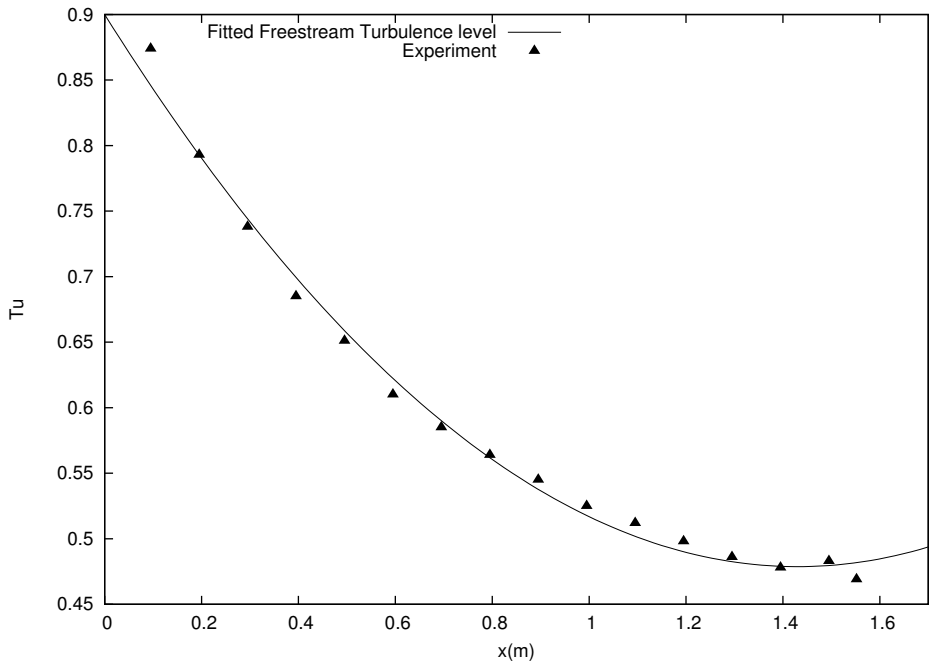

Figure 5-14: Free-stream turbulence level of T3A-.

Results of T3A- are given in Figure 5-18. If Drela's original simplified e^N method is used (see Figure 5-18a), it predicts the transition onset way too early, but the present transition model (Figure 5-18b) can accurately predict the transition onset as well as the flow in the transition region. The fully laminar solution and the fully turbulent solution are also given for comparison.
The T3C3 case is a case of bypass transition. The free-stream turbulence level and the edge velocity distribution are given by:

$$u_e = -1.82345x^6 + 14.5603x^5 - 39.1975x^4 + 46.8672x^3 - 27.8752x^2 + 9.67068x + 3.7, \tag{5.2}$$

$$Tu = -3.75122x^6 + 12.6619x^5 - 9.8453x^4 - 8.9939x^3 + 17.6025x^2 - 9.84006x + 3.0. \tag{5.3}$$

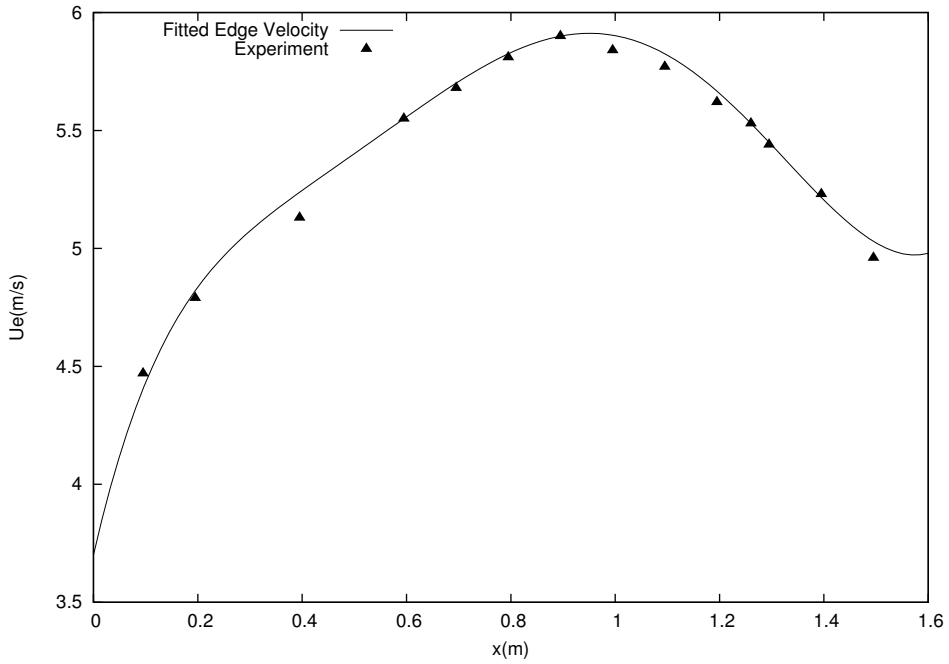

(a) Edge velocity

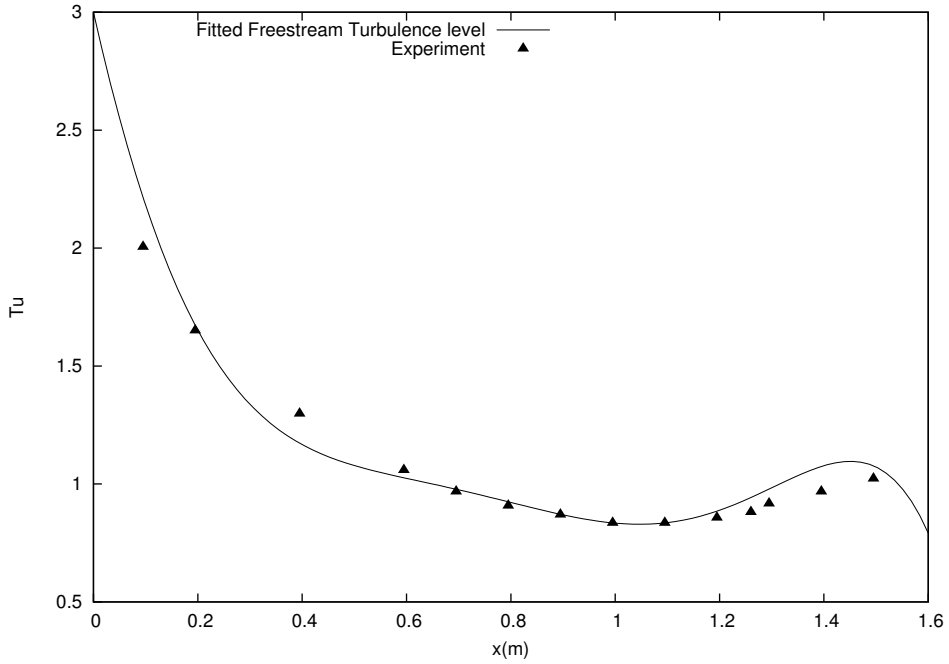

(b) Free-stream turbulence level

Figure 5-15: Edge velocity and free-stream turbulence level of T3C3.

Results are presented in Figure 5-19. The Reynolds number for the T3C3 case is very low. As a result, the start and the end of transition occur in an adverse pressure gradient. The present model predicts the position of the onset of transition a bit

early probably because the boundary layer is very close to separation when the point of transition onset is reached.
The T3C5 case is also a case of bypass transition. The free-stream turbulence level and the edge velocity distribution are given by (also see Figure 5-16):

$$u_e = -24.741x^6 + 126.944x^5 - 250.8x^4 + 236.115x^3 - 110.244x^2 + 27.6798x + 8.4, \tag{5.4}$$

$$Tu = -6.95085x^6 + 29.02x^5 - 42.8964x^4 + 23.5227x^3 + 2.26616x^2 - 7.03931x + 3.0. \tag{5.5}$$

For the T3C5 test case, the Reynolds number is high enough that the transition occurs in a favorable pressure gradient ($\frac{du_e}{dx} > 0$) near the beginning of the flat plate. From Figure 5-20 we can see that the present transition model predicts the transition onset slightly downstream but the intermittency model almost fails to predict the flow in the transition region. The reason is that the transition onset is very early and at that location, the momentum thickness θ is still very small. On top of that the favorable pressure gradient makes the spot propagation parameter δ as well as the spreading angle α comparatively small (see Figure 3-10 and 3-11). This slows down the growth of the intermittency factor γ to a great extent and makes the laminar part in the intermittency model dominant, delaying the change of the laminar boundary layer into a fully turbulent boundary layer. The present engineering approach is to modify γ by multiplying it with a factor of 10 and to make the boundary layer turn to fully turbulent one more quickly (see Figure 5-21). Further improvement of the method to handle this case is left for further research.

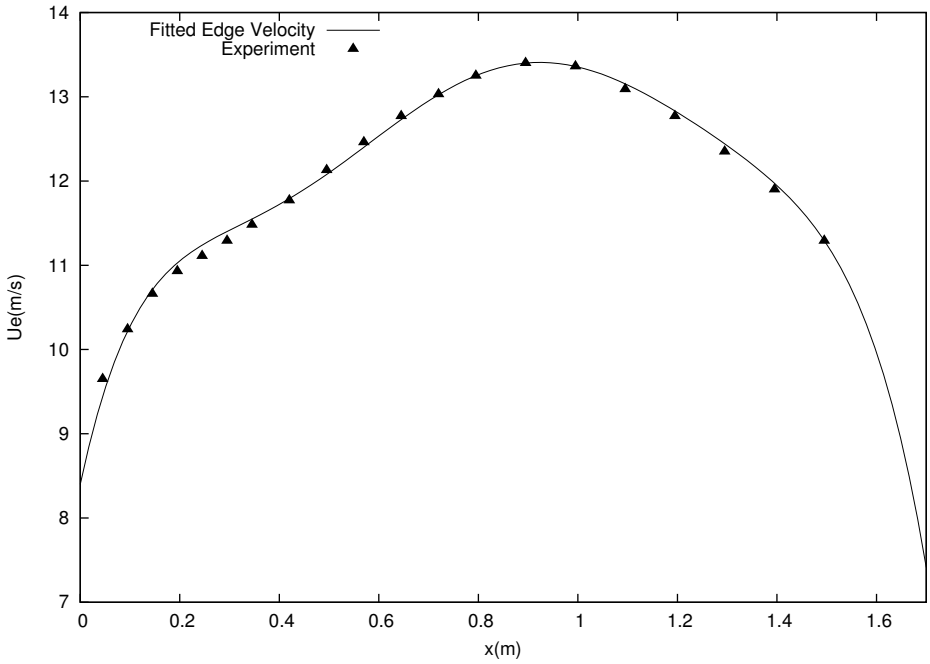

(a) Edge velocity

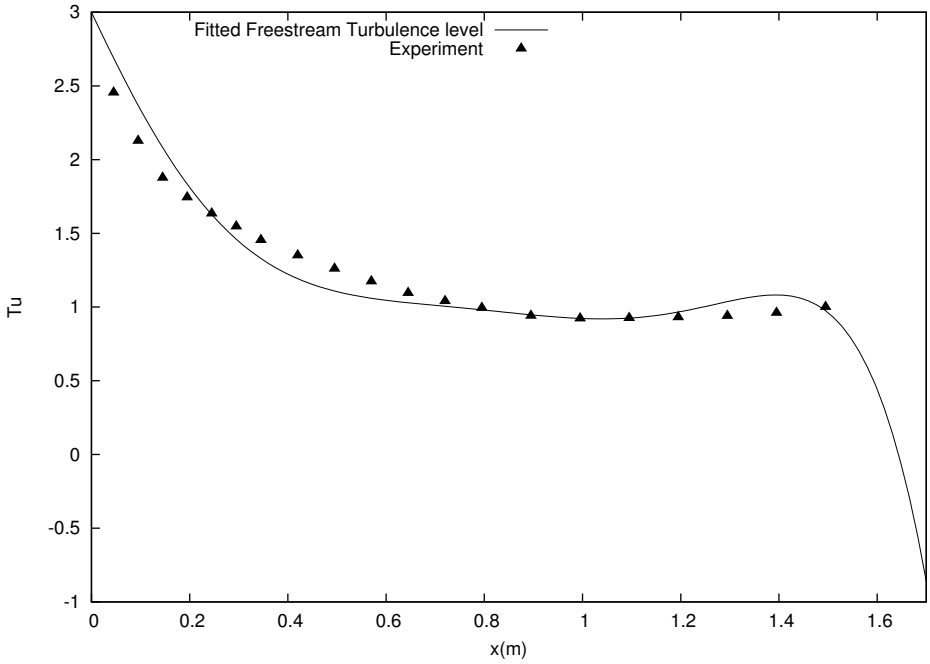

(b) Free-stream turbulence level

Figure 5-16: Edge velocity and free-stream turbulence level of T3C5.

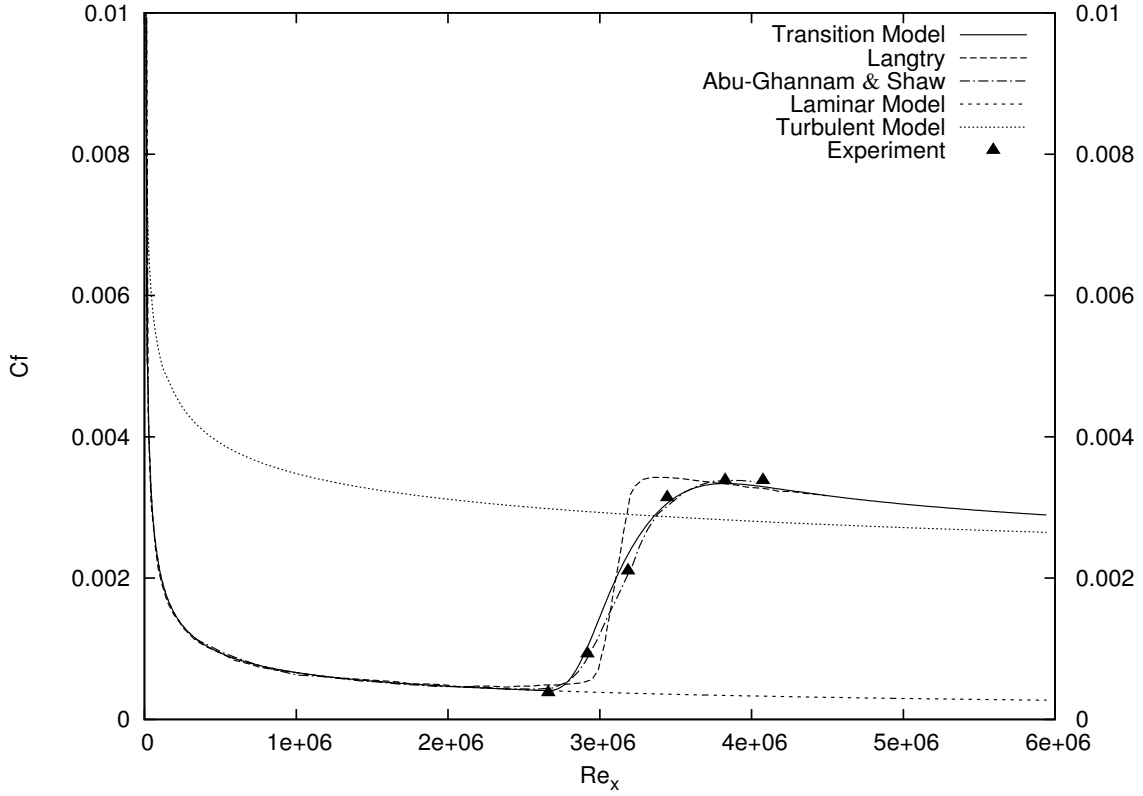

Figure 5-17: Steady simulation of Schubauer and Klebanoff's flat plate test case (skin friction coefficient).

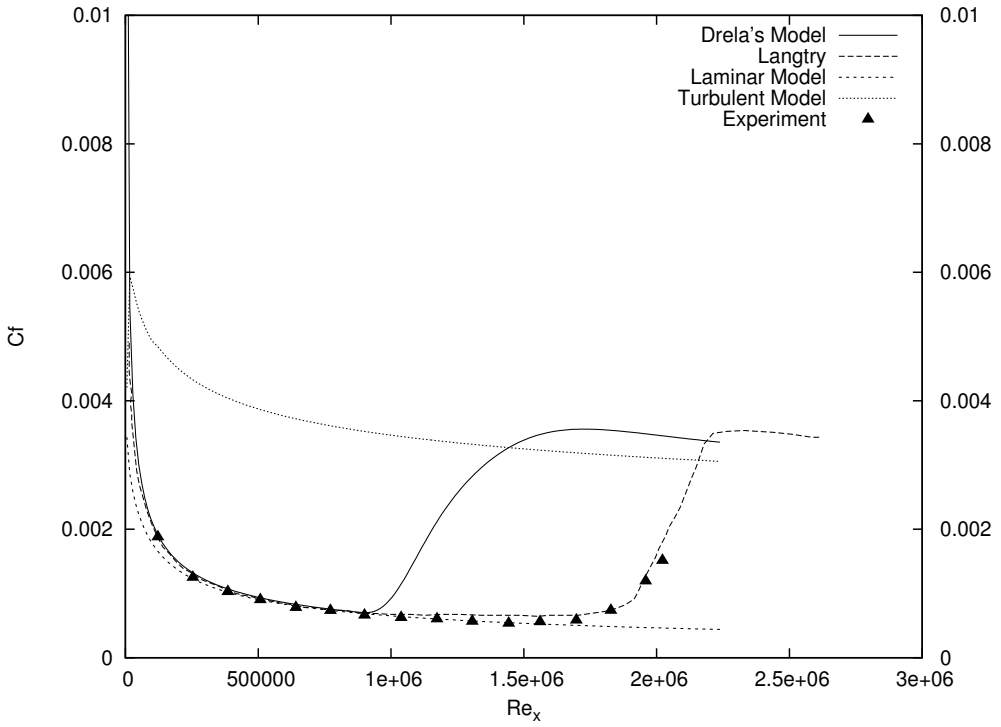

(a) Skin friction coefficient (Drela's model)

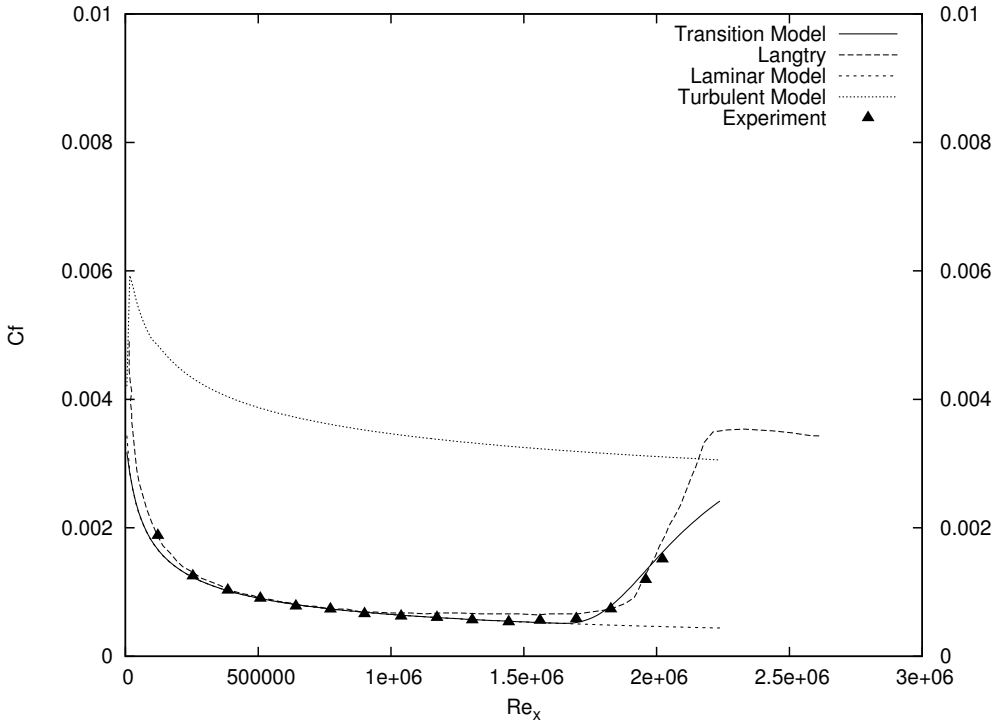

(b) Skin friction coefficient (present model)

Figure 5-18: Steady simulation of T3A- (skin friction coefficient).

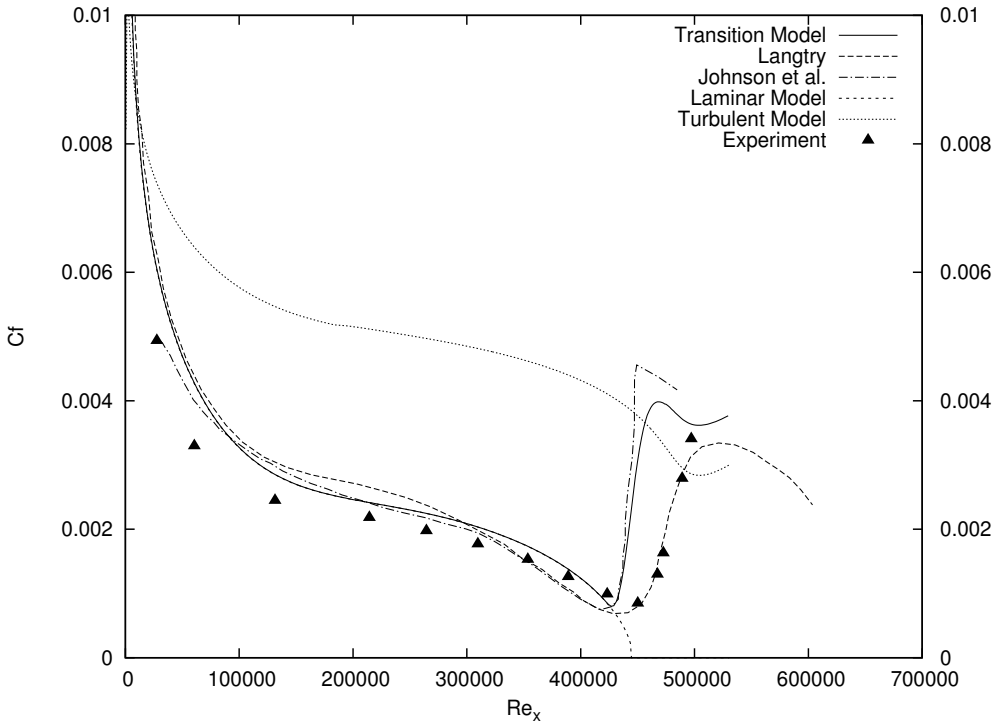

(a) Skin friction coefficient

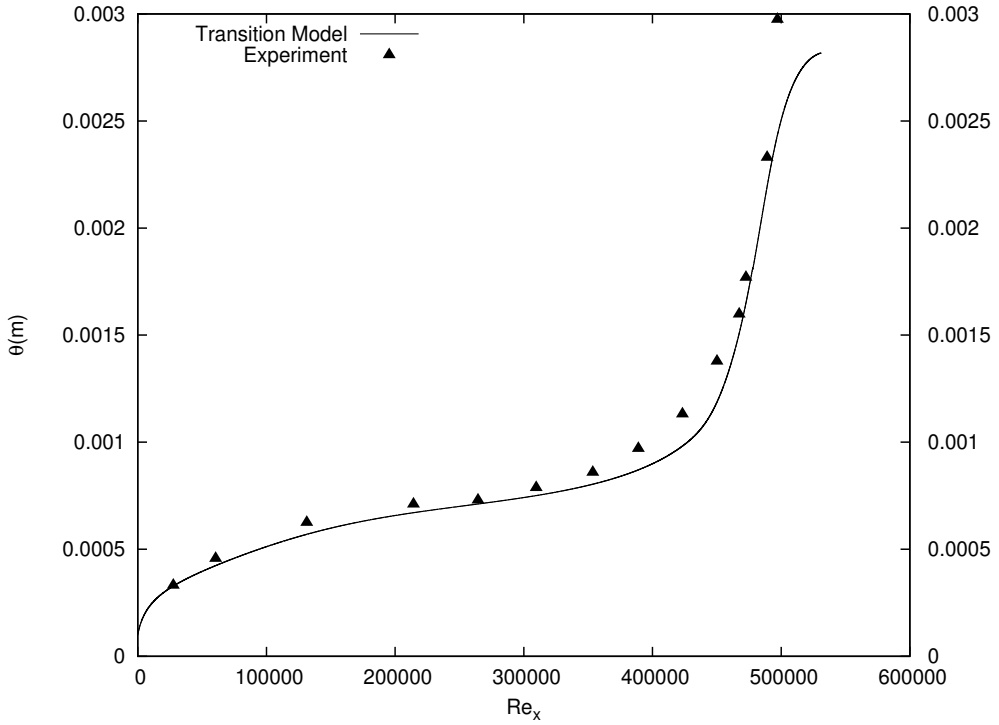

(b) Momentum thickness

Figure 5-19: Steady simulation of T3C3.

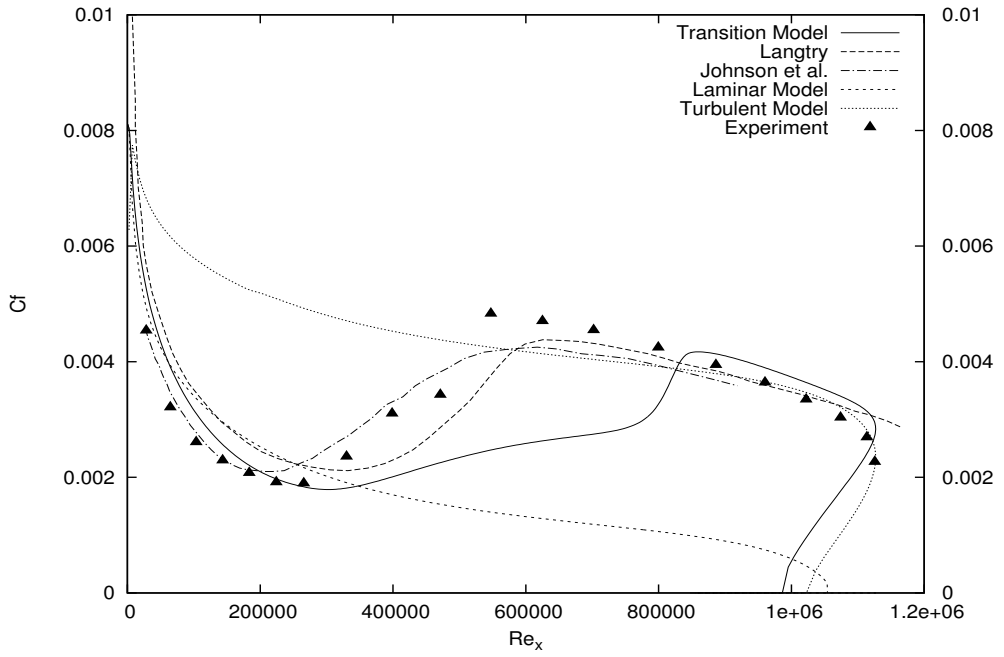

Figure 5-20: Steady simulation of T3C5 (skin friction coefficient) (without modification).

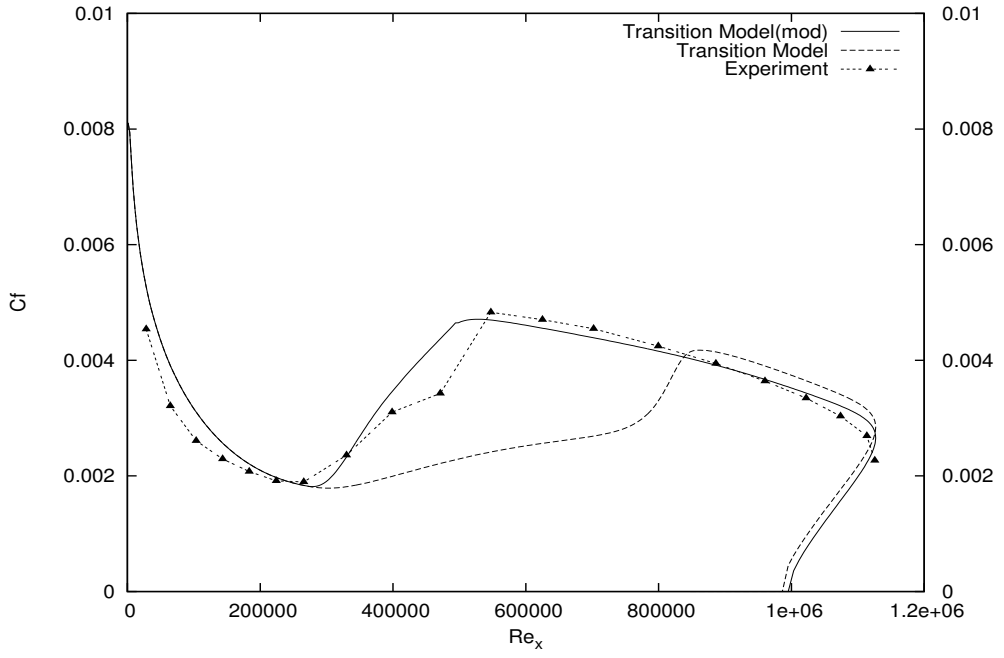

Figure 5-21: Steady simulation of T3C5 (skin friction coefficient) (with modification).

5.2.2 Unsteady models

First, two cases of a transitional boundary layer over a flat plate are considered, where the time-dependence of the edge velocity distribution is taken as a Heaviside function. The new unsteady transition model is used to resolve the transient solution. Both of them can be considered as impulsively started flat plates and in both cases the solution is expected to converge to a steady state corresponding to the solution of the steady formulation of the algorithm. Next, a 'real' time dependent edge velocity distribution is considered. Due to the fact that the current algorithm does not take into account surface curvature and can not solve a solution corresponding to a separating boundary layer, suitable unsteady test cases are very hard to find. Therefore, only simple unsteady cases are considered, aiming to show some qualitatively unsteady patterns in the solution. A full assessment of the capabilities of the unsteady algorithm has been left for future research.

Impulsively Moved Flat Plate

Two test cases in the previous section, the Schubauer and Klebanoff's flat plate and T3A- flat plate are simulated using the unsteady transition model. The simulation time is chosen to be long enough to make sure that the solution can converge to steady state. Results are presented in Figures 5-22 and 5-23, Note that the non-dimensional parameter $Re_x = \frac{u_e x}{\nu}$ is used to indicate the location of the onset of transition.
In both experiments the solution converges to the correct steady state. However, there is a sudden change in the location of the transition onset during the simulation time in both of the cases. This is because in unsteady flow, the wave number of the mode in the disturbances that is amplified most severely is not constant. This means that the individual modes in the disturbances do not grow at a constant rate and maybe even damp at some point. As stated in Section 3.2.3, the simplified e^N method cannot resolve disturbance damping very well and for that reason it is advised to use the full e^N method in further research.

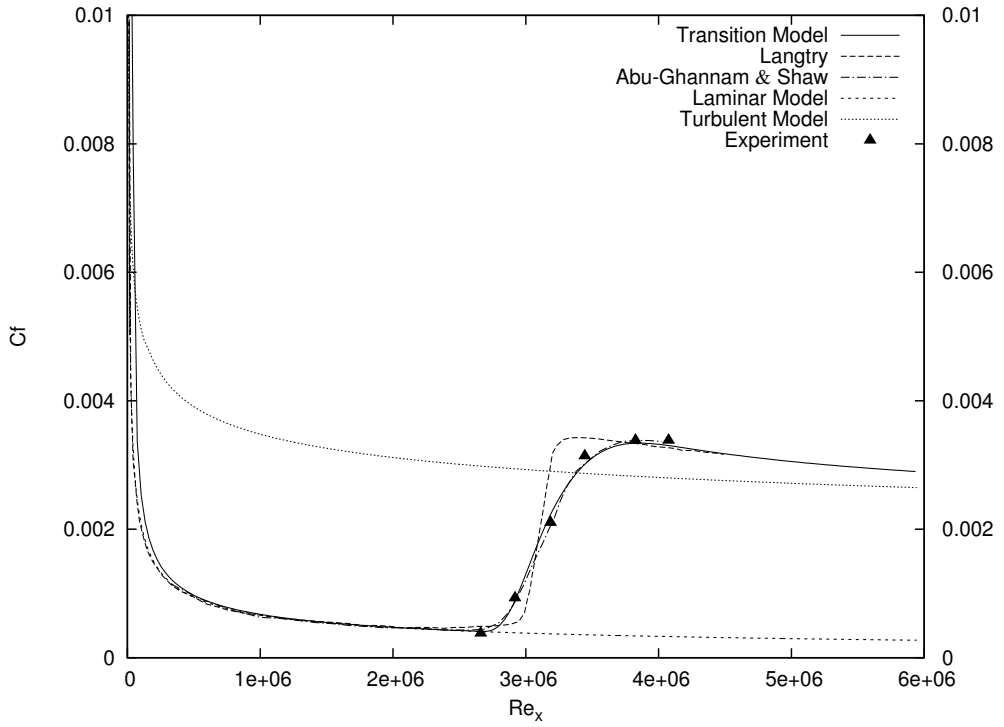

(a) Skin friction coefficient

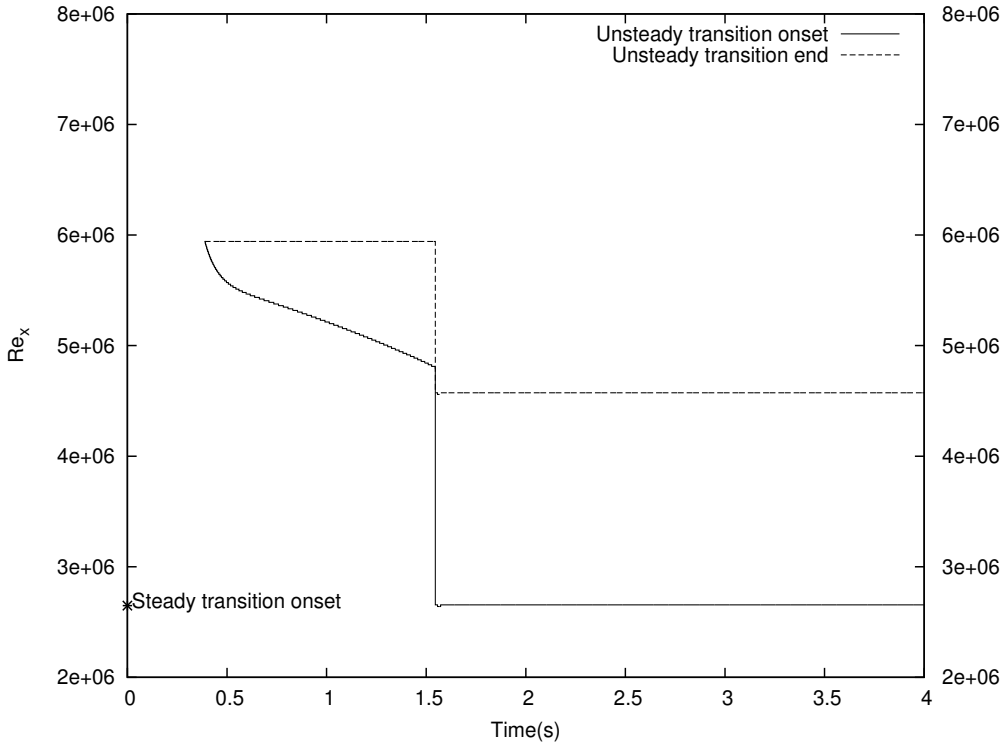

(b) Transition onset and transition end

Figure 5-22: Unsteady simulation of Schubauer and Klebanoff's flat plate test case.

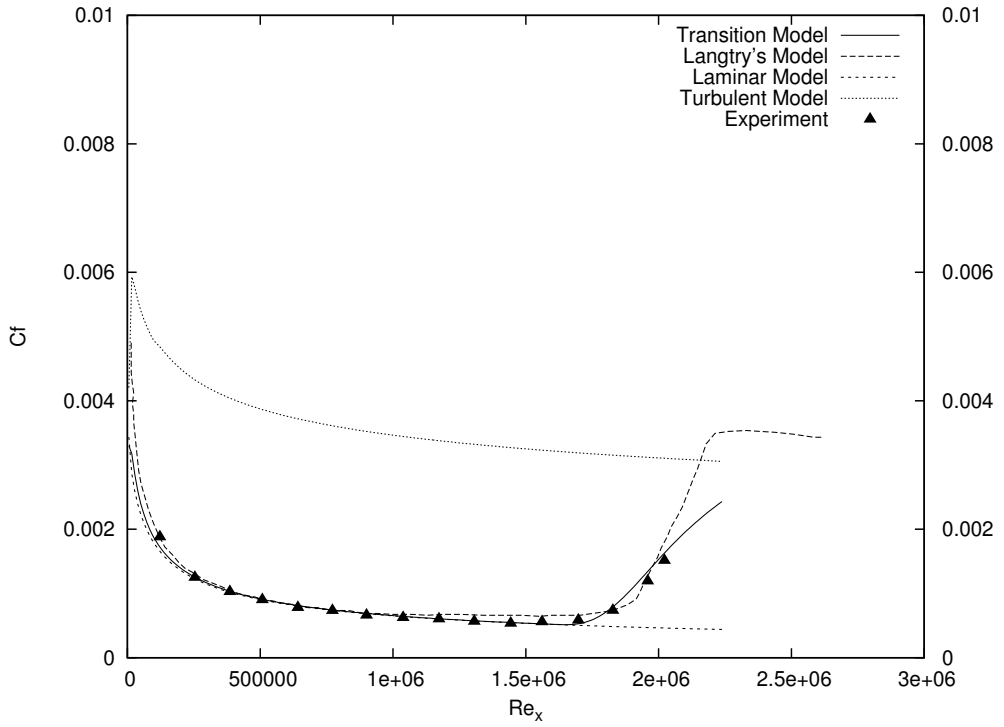

(a) Skin friction coefficient

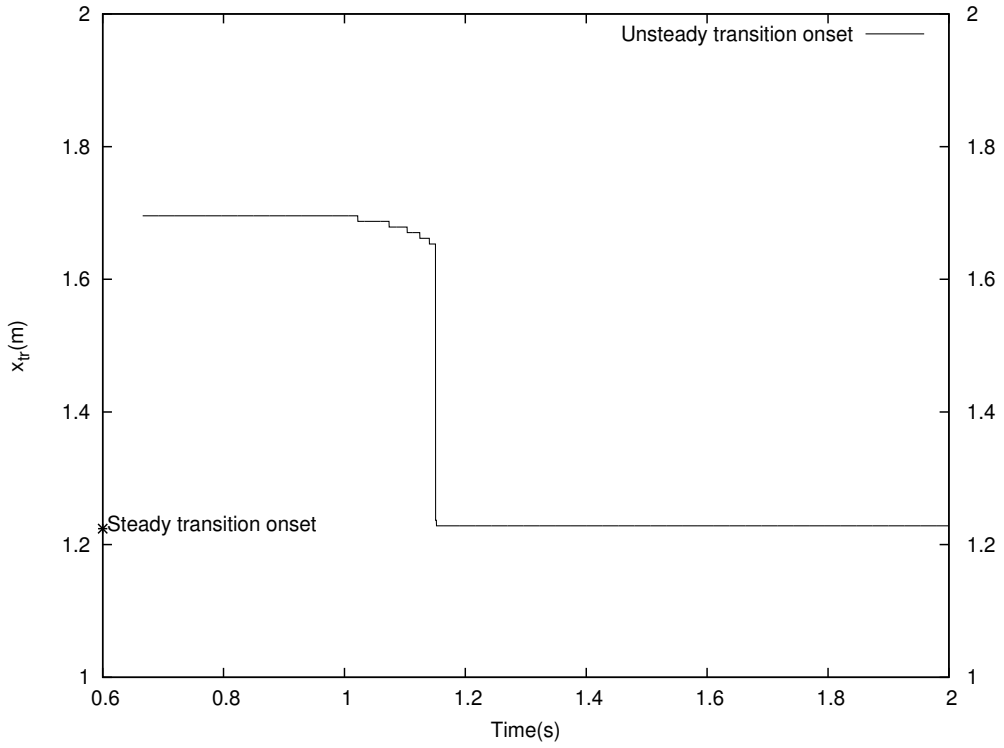

(b) Transition onset

Figure 5-23: Unsteady simulation of T3A-.

Flat plate with periodic edge velocity

The edge velocity for this series of test cases is dependent on time and given by:

$$u_e = U_\infty + \Delta U \sin(2\pi\omega t), \tag{5.6}$$

where U_∞ is the free-stream velocity at the leading edge of the flat plate, ΔU is the amplitude of the periodic part of the edge velocity and ω is the frequency of the oscillation with the unit of c/s. The input is given in Table 5.10.

Input	Case 1
Polynomial Order(P)	1
Amount of Cells(N)	400
H_{bound}	2.6
θ_{bound}	1×10^{-4}
$C_{\tau_{bound}}$	1×10^{-3}
Length(L)	3.6576
$U_\infty(m/s)$	17.8308
Re_L	3.813022×10^6
Tu	0.15
ΔU	varing
$\omega(c/s)$	varing

Table 5.10: Input for unsteady flat plate simulation.

Results of the simulations are shown in Figures 5-24 to 5-25. The simulation results of cases with constant edge velocity U_∞ are also presented for comparison. It can be seen that once the boundary layer is fully developed, the location of the onset of transition also moves periodically with the edge velocity, with a frequency equaling the frequency of the edge velocity oscillation ω. No straightforward conclusion can be drawn on the dependency of the location of transition onset on ΔU and ω, but if we look at the mean value of the transition onset location, it can be seen that as the amplitude ΔU increases, the mean transition location moves upstream which means that the transition onset is earlier. Concerning the frequency ω, we can see that if ω is very small which indicates that the mean flow changes very slowly in time, the mean transition onset location is very close to the steady state, which should not be surprising as $\omega = 0$, it will lead to location of the steady state. However, as the

frequency increases, the location of transition onset also moves upstream. Note that the mean value of the transition onset location is taken to be the average value of the maximal and minimal Re_x in one time period. It is also suggested to investigate the non-dimensional parameter introduced by Obremski and Fejer[34]:

$$Re_{NS} = \frac{U_\infty \Delta U}{2\pi\omega\nu}, \tag{5.7}$$

and a more formulated relation may be obtained.

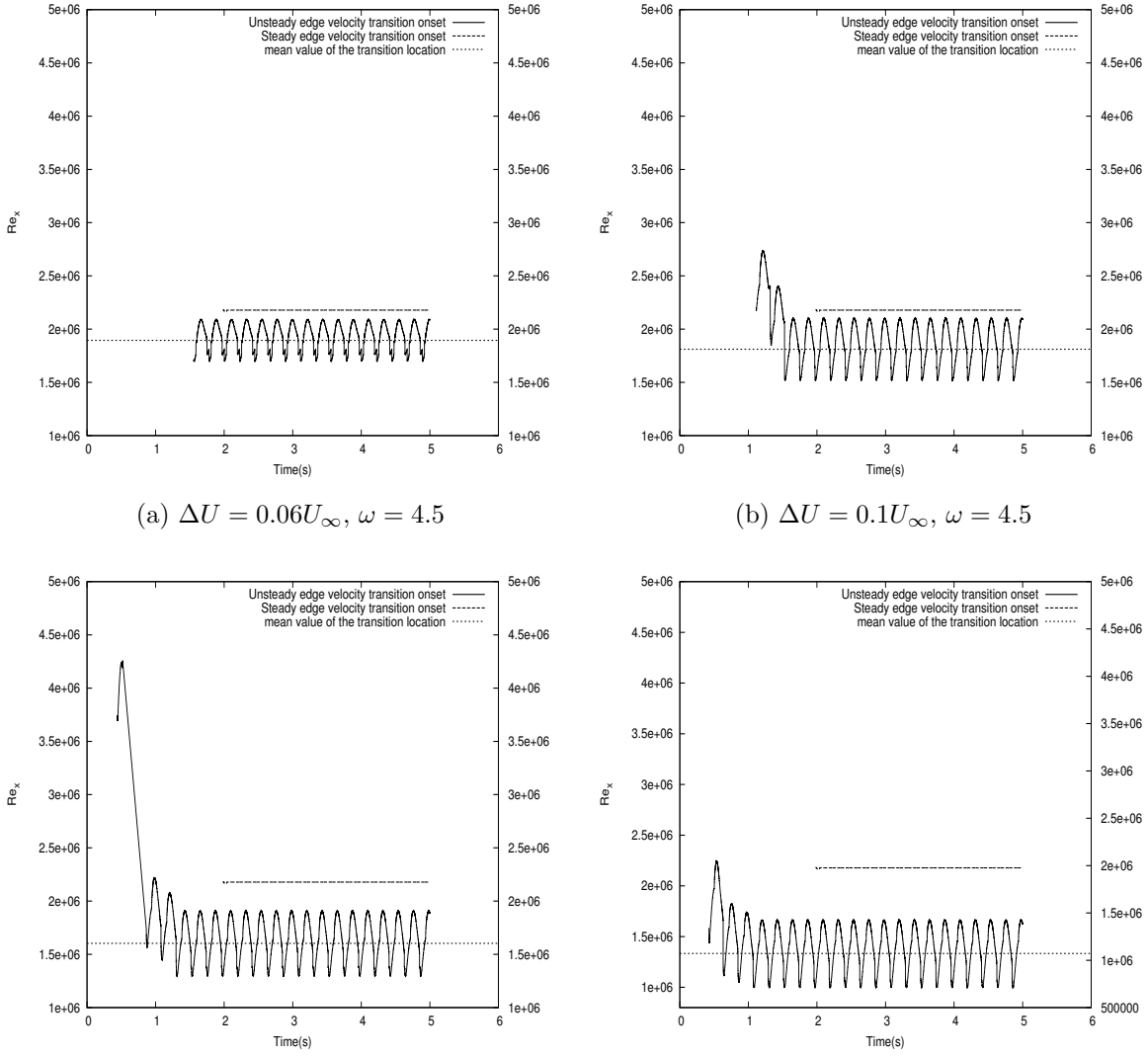

(a) $\Delta U = 0.06U_\infty$, $\omega = 4.5$

(b) $\Delta U = 0.1U_\infty$, $\omega = 4.5$

(c) $\Delta U = 0.137U_\infty$, $\omega = 4.5$

(d) $\Delta U = 0.2U_\infty$, $\omega = 4.5$

Figure 5-24: Comparison of the location of transition onset with different amplitude ΔU.

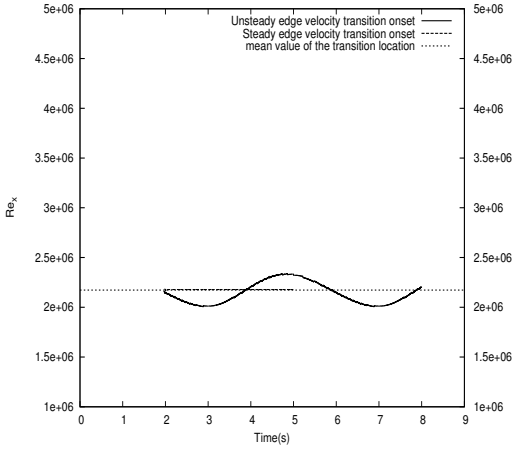

(a) $\Delta U = 0.1U_\infty$, $\omega = 0.25$

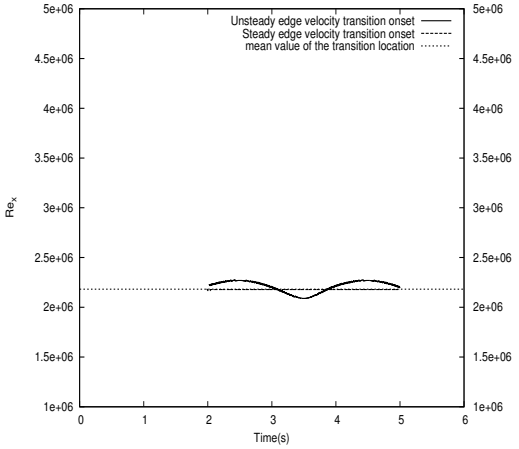

(b) $\Delta U = 0.1U_\infty$, $\omega = 0.5$

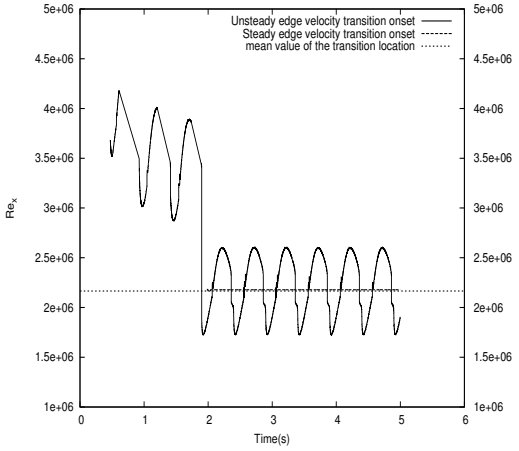

(c) $\Delta U = 0.1U_\infty$, $\omega = 2$

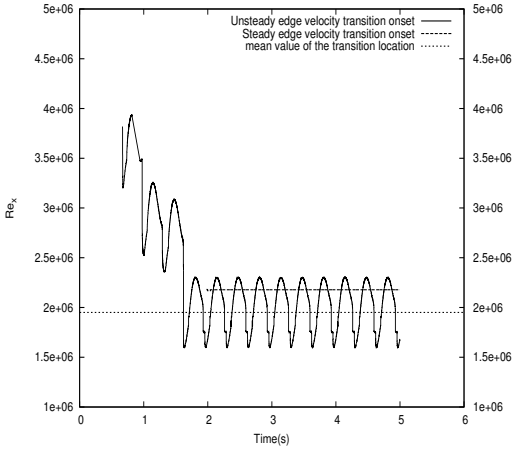

(d) $\Delta U = 0.1U_\infty$, $\omega = 3$

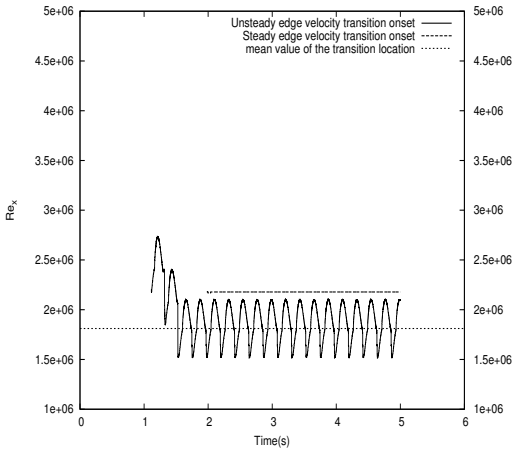

(e) $\Delta U = 0.1U_\infty$, $\omega = 4.5$

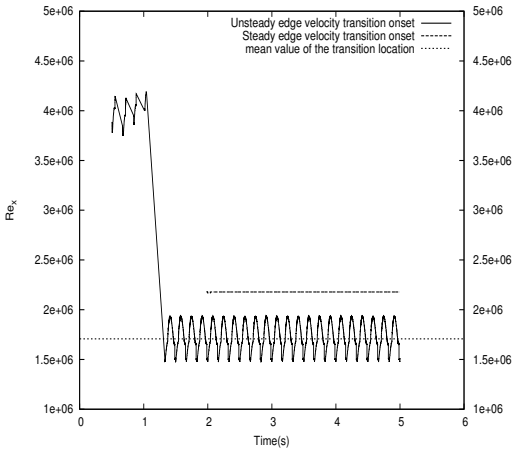

(f) $\Delta U = 0.1U_\infty$, $\omega = 6$

Figure 5-25: Comparison of the location of transition onset with different frequency ω.

5.3 Conclusions

In this chapter, the models for the turbulent and transitional boundary layers are tested for a variety of cases.

The present models for the turbulent boundary layer, both the dissipation integral method and the entrainment integral method, can predict the properties of a turbulent boundary layers with zero pressure gradient pretty well, for both steady and unsteady cases. However, for some cases with a pressure gradient, especially an adverse pressure gradient (i.e. Flow 1100), the present models fail to give very satisfactory results. This is probably because the present integral formulation has lost too much detail of the flow inside the boundary layer and the closure relations used in the present models are mainly based on cases with zero pressure gradient.

The original simplified e^N method is extended and improved to make it able to predict the onset of not only natural transition, but also bypass transition. The pressure gradient and the change in free-stream turbulence level are also taken into consideration. Therefore, a series of test cases with different flow conditions is analyzed. In general, the present model can predict the onset of transition well. More specifically, the prediction of the present model is comparable to the widely used design tool XFOIL but is more generally applicable. A separate algebraic intermittency model is used to predict the flow inside the transition region. For some cases with complex flow conditions (i.e. Test T3C5), it fails to give satisfactory results. Improvement can be expected from a more advanced formulation of the intermittency factor γ.

The unsteady transition model based on the simplified e^N method is also tested for a number of cases, but very little results are available for validation of the model. It is shown the solutions of the unsteady model for impulsively started flat plates converge to the correct steady state solution. For the case of a periodically excited flat plate, the model predicts a strong dependence of the point of transition on the frequency of the excitation. However, the full e^N method is still recommended in further investigation in order to get a more accurate insight of the transition process, because the simplified method is unable to describe dampening of the disturbances.

Chapter 6

Conclusions and outlooks

6.1 Conclusions

In this thesis, the modeling of turbulent boundary layers and laminar-to-turbulent transition using a formulation based on the unsteady integral boundary layer equations is investigated.

It has been shown that the two integral methods studied in the thesis, the *dissipation integral method* and the *entrainment integral method* lead to very similar results for the turbulent boundary layers simulated in the present work. For non-equilibrium flows which strongly depend on upstream history, an additional shear-lag equation needs to be added to the system of the turbulent integral boundary layer equations which models the lag of shear stress inside the boundary layer. However, it has been shown that for attached equilibrium flow, this equation does not improve the solution. That is why a switch criterion is set so that equilibrium flow and non-equilibrium flow can be simulated by different models and more realistic results can be obtained.

The simplified e^N envelop method has been shown to predict the onset of natural transition pretty well as long as the critical amplification factor N_{crit} is chosen properly. The method has been extended with an additional term based on empirical relations for the momentum thickness Reynolds number at the location of transition onset $Re_{\theta onset}$ in order to predict the onset of bypass transition. As the free-stream turbulence level is high and the growth of Tollmien-Schlichting (T-S) waves is bypassed, the additional term becomes dominant in the model and thus the onset of bypass transition can be predicted well. In order to model transition onset under varying free-stream turbulence level Tu, an effective free-stream turbulence level is defined and the growth of the T-S waves becomes also dependent on Tu. A separate and simplified intermittency model is included in the system to predict the flow in the transition region. For incompressible flow around wind turbines under low

free-stream turbulence level the transition region is narrow and does not affect the development of the flow significantly. The unsteady model for the prediction of transition onset is also derived, but due to the limitations of the current model (neither surface curvature nor separation can be taken into account), only simple test cases can be simulated and further investigation needs to be conducted.

6.2 Outlooks

Future work should focus on the development of a suitable viscous-inviscid interaction scheme for the coupling of the current boundary layer models and the boundary element method for solving the potential flow which has already been developed at ECN[51]. Some work on the interaction scheme has been done by Haciahmetoglu[23] at ECN but further investigation is necessary. Once the viscous-inviscid interaction scheme is applied, the main change to the present boundary layer models is that the additional equation will make the system non-conservative. The non-conservative formulation has several advantages, including the ability of resolving separation and the usage of zero initial conditions, basically, avoiding singularity problems. In order to solve the non-conservative system, an implicit space-time path-consistent Discontinuous Galerkin (DG) framework for solving nonlinear, non-conservative hyperbolic systems is under development. Furthermore, a quadrature-free approach instead of the Gaussian quadrature rule can be used for the numerical integration to reduce discretisation errors. Seubers has made significant contributions to this new DG framework and more details can be found in [43]. Details on quadrature-free approaches can also be found in Özdemir[37].

Once the DG framework is developed, the present boundary layer models can be incorporated. Some assumptions made in Section 3.2.2 and 3.2.3 can be further investigated to see if more realistic empirical relations for the intermittency factor γ and $\frac{\partial \tilde{Re}}{\partial t}$ can be formulated. The unsteady transition model itself can be tested for more general test cases. The effect of incorporating the full e^N method has to be assessed as well and results should be compared to see if the accuracy of the current simplified e^N method is satisfactory.

The next step will be the extension of the current model to a three-dimensional formulation. The adaption of the current boundary layer models as well as the DG framework to a three-dimensional still requires to be further investigated.

Appendix A

The derivation of the unsteady shear-lag equation

The unsteady shear-lag equation is rederived here and modifications are made based on Özdemir's derivation[36].

The unsteady turbulent kinetic energy equation for a 2D imcompressible flow can be written as:

$$\frac{1}{2}\frac{\partial\overline{q^2}}{\partial t}+\frac{1}{2}\underbrace{\left(u\frac{\partial\overline{q^2}}{\partial x}+v\frac{\partial\overline{q^2}}{\partial y}\right)}_{\text{advection}}-\underbrace{\frac{\tau}{\rho}\frac{\partial u}{\partial y}}_{\text{production}}+\underbrace{\frac{\partial}{\partial y}\left(\frac{\overline{pv}}{\rho}+\frac{1}{2}\overline{q^2v}\right)}_{\text{diffusion}}+\underbrace{\varepsilon}_{\text{dissipation}}=0, \quad \text{(A.1)}$$

with

$$q^2=u^2+v^2, \quad \tau=-\rho\overline{uv}, \quad \varepsilon\simeq v\overline{(\frac{\partial u_i}{\partial x_j})^2}. \quad \text{(A.2)}$$

Equation (A.1) can be regarded as an equation for the advection or rate of change of turbulent kinetic energy along a mean streamline through a point if all the other

terms are known at that point. Bradshaw et al.[6] makes the following definitions:

$$a_1 \equiv \frac{\tau}{\rho\overline{q^2}}, \tag{A.3}$$

$$L \equiv \frac{(\tau/\rho)^{\frac{1}{2}}}{\varepsilon}, \tag{A.4}$$

$$G = \frac{\left(\frac{\overline{pv}}{\rho} + \frac{1}{2}\overline{q^2 v}\right)}{\left(\frac{\tau_{\max}}{\rho}\right)^{\frac{1}{2}} \frac{\tau}{\rho}}, \tag{A.5}$$

and equation (A.1) becomes:

$$\frac{\partial}{\partial t}\left(\frac{\tau}{2a_1\rho}\right) + u\frac{\partial}{\partial x}\left(\frac{\tau}{2a_1\rho}\right) + v\frac{\partial}{\partial y}\left(\frac{\tau}{2a_1\rho}\right) - \frac{\tau}{\rho}\frac{\partial u}{\partial y} + \left(\frac{\tau_{\max}}{\rho}\right)^{\frac{1}{2}}\frac{\partial}{\partial y}\left(G\frac{\tau}{\rho}\right) + \frac{1}{L}\left(\frac{\tau}{\rho}\right)^{\frac{1}{2}} = 0. \tag{A.6}$$

Here, a_1, L and G are functions of $\frac{y}{\delta}$ which depend only on the shape of the shear stress profile and L has the dimension of length while a_1 and G are non-dimensional. L can be regarded as *dissipation length scale* which is the most important one of the three functions because the dissipation is much larger than the advection and diffusion over the boundary layer. Dividing equation (A.6) by $\frac{\tau}{\rho}$ gives the *mixing-length* equation with advection and diffusion terms. If we define:

$$\zeta = \frac{G}{\left(\frac{\tau_{\max}}{\rho u_e^2}\right)} = f(\frac{y}{\delta}), \tag{A.7}$$

then at the maximum $\left(\frac{\tau}{\rho}\right)_{\max}$:

$$\left(\frac{\tau}{\rho}\right)_{\max}^{\frac{1}{2}}\frac{\partial}{\partial y}\left(G\frac{\tau}{\rho}\right) = \frac{1}{\delta u_e}\left(\frac{\tau}{\rho}\right)_{\max}^{2}\zeta', \tag{A.8}$$

where $\zeta' = \frac{d\zeta}{d(y/\delta)}$, and equation (A.6) becomes:

$$\frac{1}{2a_1}\frac{\partial}{\partial t}\left(\frac{\tau}{\rho}\right)_{\max} + \frac{u}{2a_1}\frac{\partial}{\partial x}\left(\frac{\tau}{\rho}\right)_{\max} - \frac{\partial u}{\partial y}\left(\frac{\tau}{\rho}\right)_{\max} + \frac{1}{u_e\delta}\left(\frac{\tau}{\rho}\right)_{\max}^{2}\zeta' + \frac{1}{L}\left(\frac{\tau}{\rho}\right)_{\max}^{\frac{3}{2}} = 0. \tag{A.9}$$

Recall the definition of C_τ and for the present work, we consider ρ as constant, thus $\left(\frac{\tau}{\rho}\right)_{\max} = \left(\frac{\tau_{\max}}{\rho}\right)$, it becomes:

$$\frac{1}{2a_1}\frac{\partial}{\partial t}(C_\tau u_e^2) + \frac{u}{2a_1}\frac{\partial}{\partial x}(C_\tau u_e^2) - \frac{\partial u}{\partial y}(C_\tau u_e^2) + \frac{1}{u_e\delta}(C_\tau u_e^2)^2\zeta' + \frac{1}{L}(C_\tau u_e^2)^{\frac{3}{2}} = 0. \quad \text{(A.10)}$$

Muliplying by $\frac{2a_1\delta}{uu_e^2C_\tau}$ gives:

$$\frac{\delta}{uu_e^2C_\tau}\frac{\partial}{\partial t}(C_\tau u_e^2) + \frac{\delta}{u_e^2C_\tau}\frac{\partial}{\partial x}(C_\tau u_e^2) - \frac{2a_1\delta}{u}\frac{\partial u}{\partial y} + \frac{2a_1u_eC_\tau}{u}\zeta' + \frac{2a_1\delta u_e}{uL}C_\tau^{\frac{1}{2}} = 0. \quad \text{(A.11)}$$

Rearranging the above equation gives:

$$\frac{\delta}{uu_e^2C_\tau}\frac{\partial}{\partial t}(C_\tau u_e^2) + \frac{\delta}{u_e^2C_\tau}\frac{\partial}{\partial x}(C_\tau u_e^2) = \frac{2a_1u_e}{u}\left(\frac{\delta}{u_e}\frac{\partial u}{\partial y} - C_\tau\zeta' - \frac{\delta}{L}C_\tau^{\frac{1}{2}}\right). \quad \text{(A.12)}$$

It can be assumed that the dissipation length scale L can be equal to the conventional mixing length $l = \sqrt{\frac{\tau}{\rho}}\frac{du}{dy}$ at the position of $\tau_{\max}$. Also assuming that the dissipation term, $C_\tau\zeta'$, is negligible compared to the other terms:

$$\frac{\delta}{uu_e^2C_\tau}\frac{\partial}{\partial t}(C_\tau u_e^2) + \frac{\delta}{u_e^2C_\tau}\frac{\partial}{\partial x}(C_\tau u_e^2) = 2a_1\frac{u_e}{u}\frac{\delta}{L}\left(C_{\tau EQ}^{\frac{1}{2}} - C_\tau^{\frac{1}{2}}\right), \quad \text{(A.13)}$$

where $C_{\tau EQ}^{\frac{1}{2}} = \frac{L}{u_e}\frac{\partial u}{\partial y}$. In Thomas[47] empirical relations for a_1, $\frac{u_e}{u}$ and $\frac{\delta}{L}$ are given by:

$$a_1 = 0.15, \quad \text{(A.14)}$$

$$\frac{u_e}{u} = \frac{3H}{H+2}, \quad \text{(A.15)}$$

$$\frac{\delta}{L} = 12.5, \quad \text{(A.16)}$$

Applying the chain rules to equation (A.9), it becomes:

$$\frac{\delta}{uu_e^2C_\tau}\left(u_e^2\frac{\partial C_\tau}{\partial t} + 2u_eC_\tau\frac{\partial u_e}{\partial t}\right) + \frac{\delta}{u_e^2C_\tau}\left(u_e^2\frac{\partial C_\tau}{\partial x} + 2u_eC_\tau\frac{\partial u_e}{\partial x}\right) = 2a_1\frac{u_e}{u}\frac{\delta}{L}\left(C_{\tau EQ}^{\frac{1}{2}} - C_\tau^{\frac{1}{2}}\right), \quad \text{(A.17)}$$

and then:

$$\frac{\delta}{uC_\tau}\frac{\partial C_\tau}{\partial t}+\frac{\delta}{C_\tau}\frac{\partial C_\tau}{\partial x}=2a_1\frac{u_e}{u}\frac{\delta}{L}\left(C_{\tau EQ}^{\frac{1}{2}}-C_\tau^{\frac{1}{2}}\right)-\frac{2\delta}{uu_e}\frac{\partial u_e}{\partial t}-\frac{2\delta}{u_e}\frac{\partial u_e}{\partial x}. \tag{A.18}$$

Muliplying it by $\frac{u_eC_\tau}{\delta}$ leads to:

$$\frac{u_e}{u}\frac{\partial C_\tau}{\partial t}+u_e\frac{\partial C_\tau}{\partial x}=\frac{u_eC_\tau}{\delta}2a_1\frac{u_e}{u}\frac{\delta}{L}\left(C_{\tau EQ}^{\frac{1}{2}}-C_\tau^{\frac{1}{2}}\right)-\frac{u_e}{u}\frac{2C_\tau}{u_e}\frac{\partial u_e}{\partial t}-2C_\tau\frac{\partial u_e}{\partial x}. \tag{A.19}$$

As $\frac{u_e}{u}$ is given by empirical relations and it is assumed to be locally constant. Therefore, it can be directly put into the derivatives, applying chain rule to the second term on the left hand side results in the final form of the unsteady shear-lag equation:

$$\frac{\partial(\frac{u_e}{u}C_\tau)}{\partial t}+\frac{\partial(u_eC_\tau)}{\partial x}=\frac{C_\tau u_e}{\delta}2a_1\frac{u_e}{u}\frac{\delta}{L}\left(C_{\tau_{EQ}}^{\frac{1}{2}}-C_\tau^{\frac{1}{2}}\right)-\frac{u_e}{u}\frac{2C_\tau}{u_e}\frac{\partial u_e}{\partial t}-C_\tau\frac{\partial u_e}{\partial x}. \tag{A.20}$$

Closure relations are already given in Section 2.4.2.

Appendix B

Additional results

Additional results are presented in this section.

B.1 Results of turbulent boundary layers

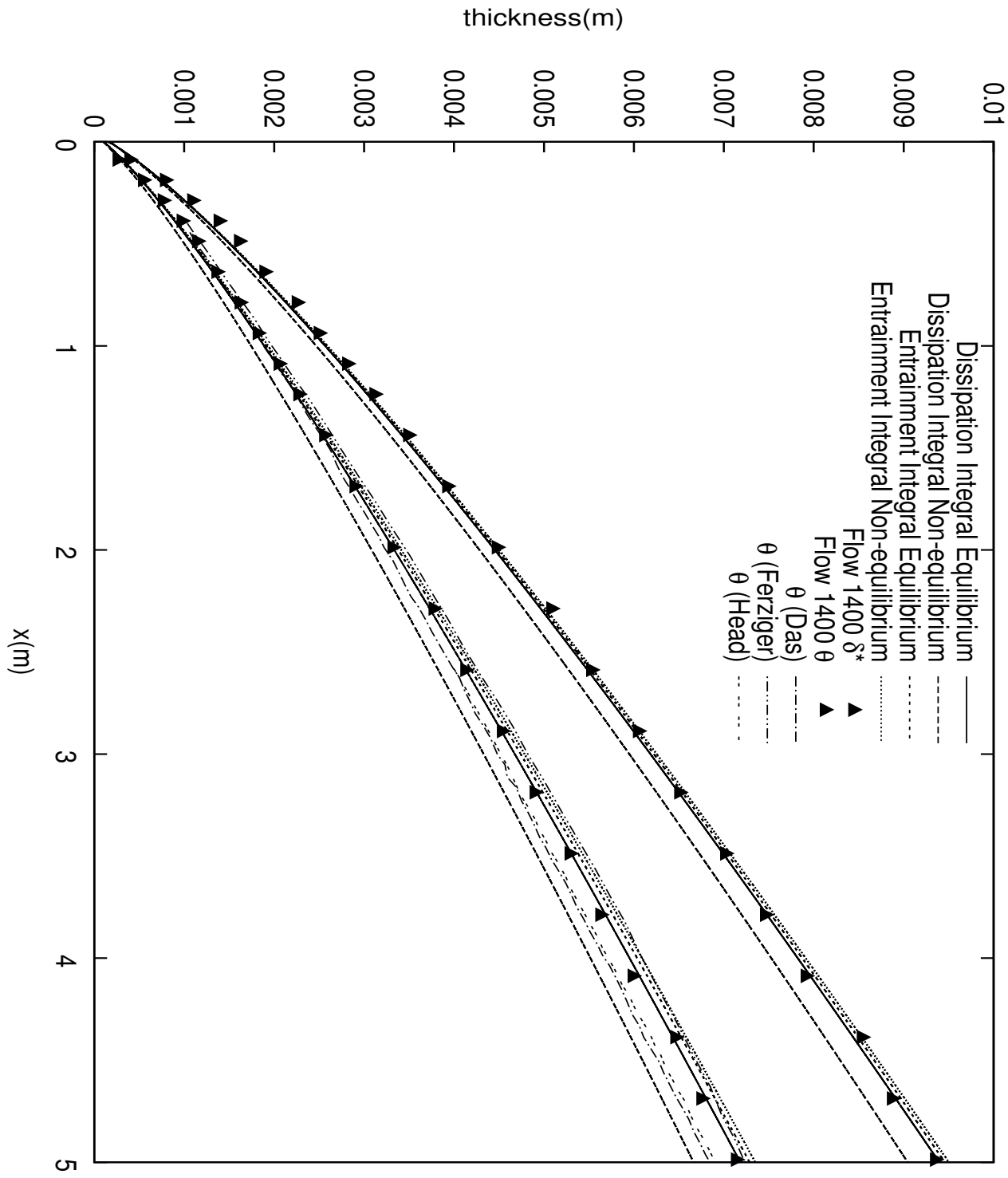

Figure B-1: Steady simulation of the Flow 1400 (momentum thickness and displacement thickness).

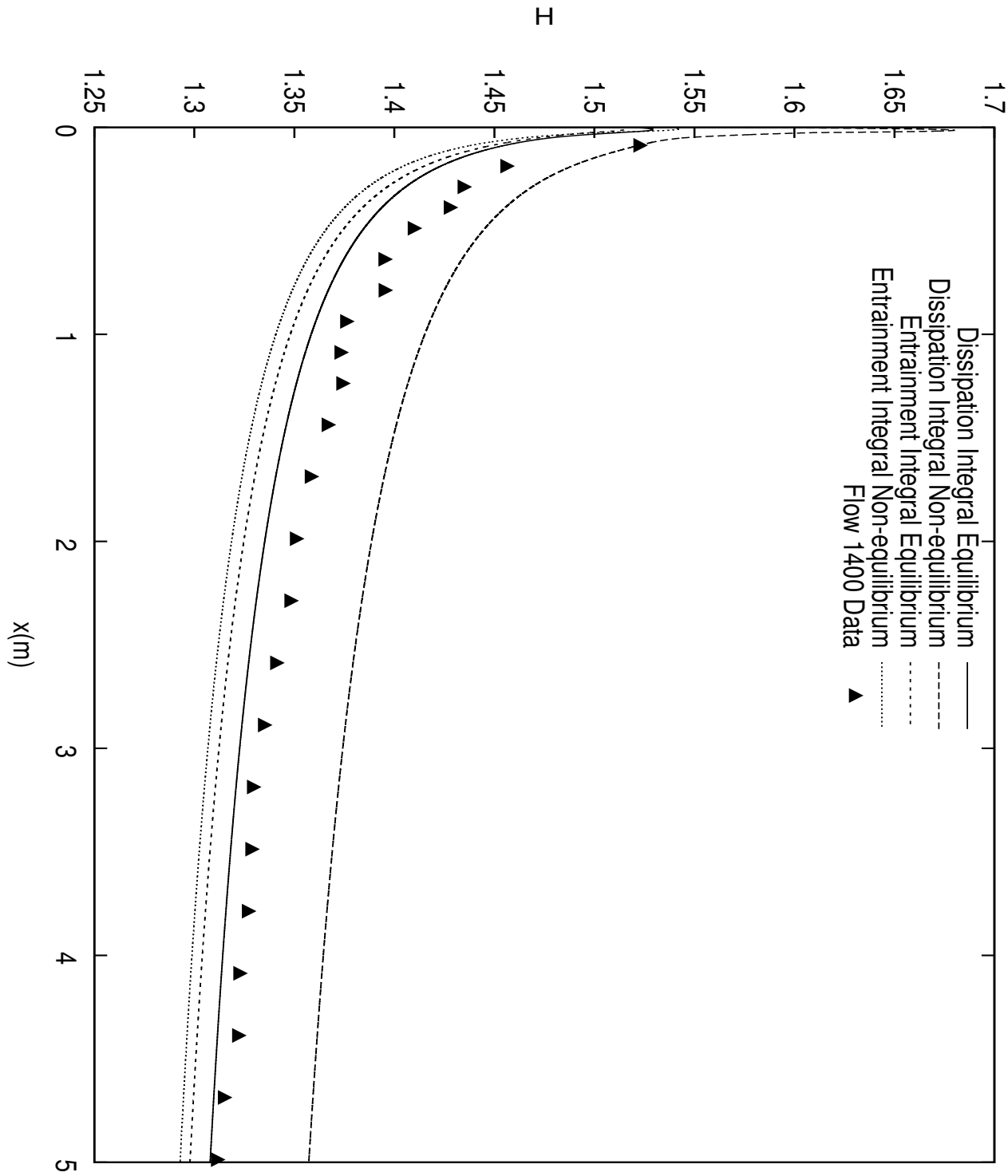

Figure B-2: Steady simulation of the Flow 1400 (shape factor).

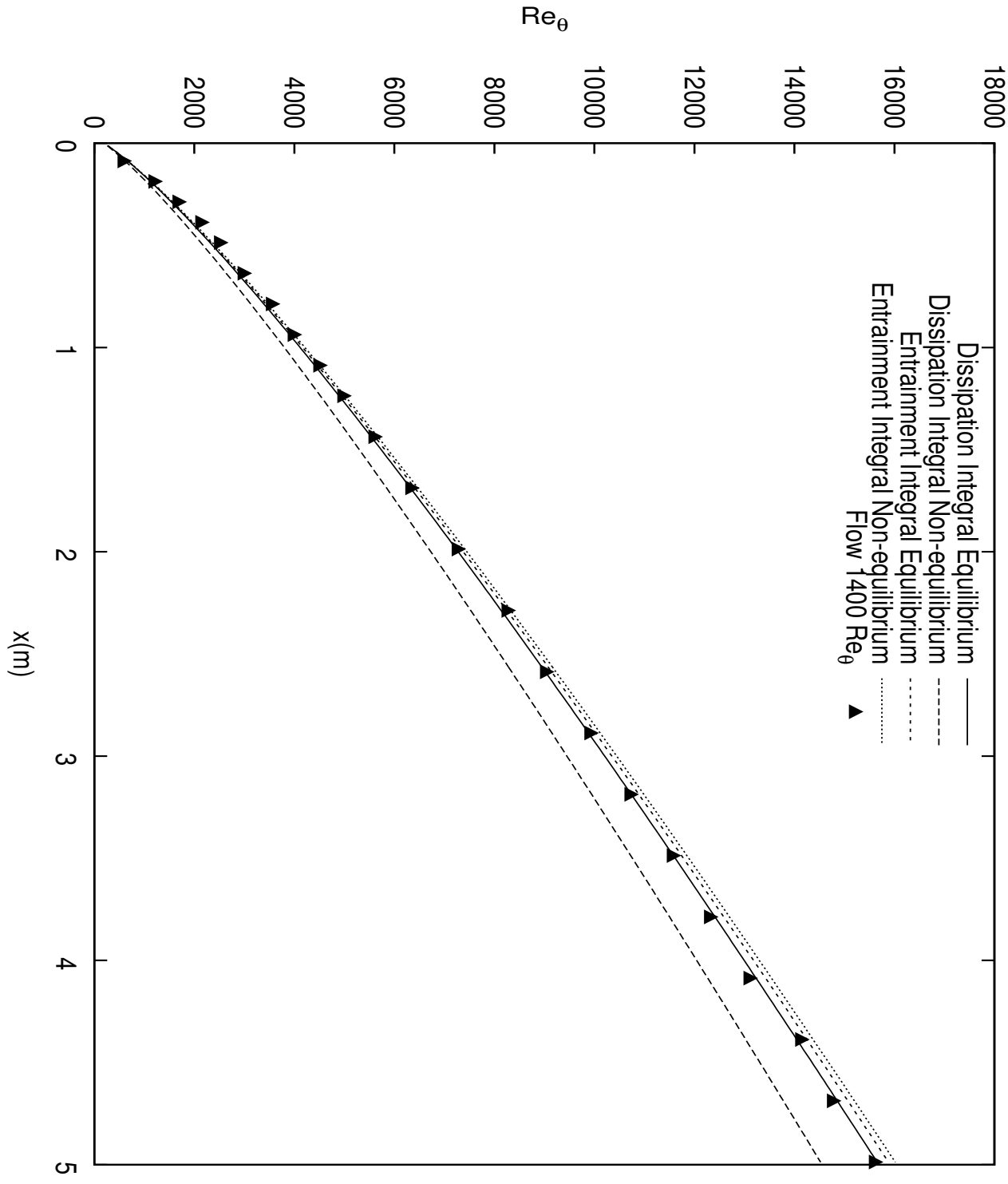

Figure B-3: Steady simulation of the Flow 1400 (momentum thickness Reynolds number).

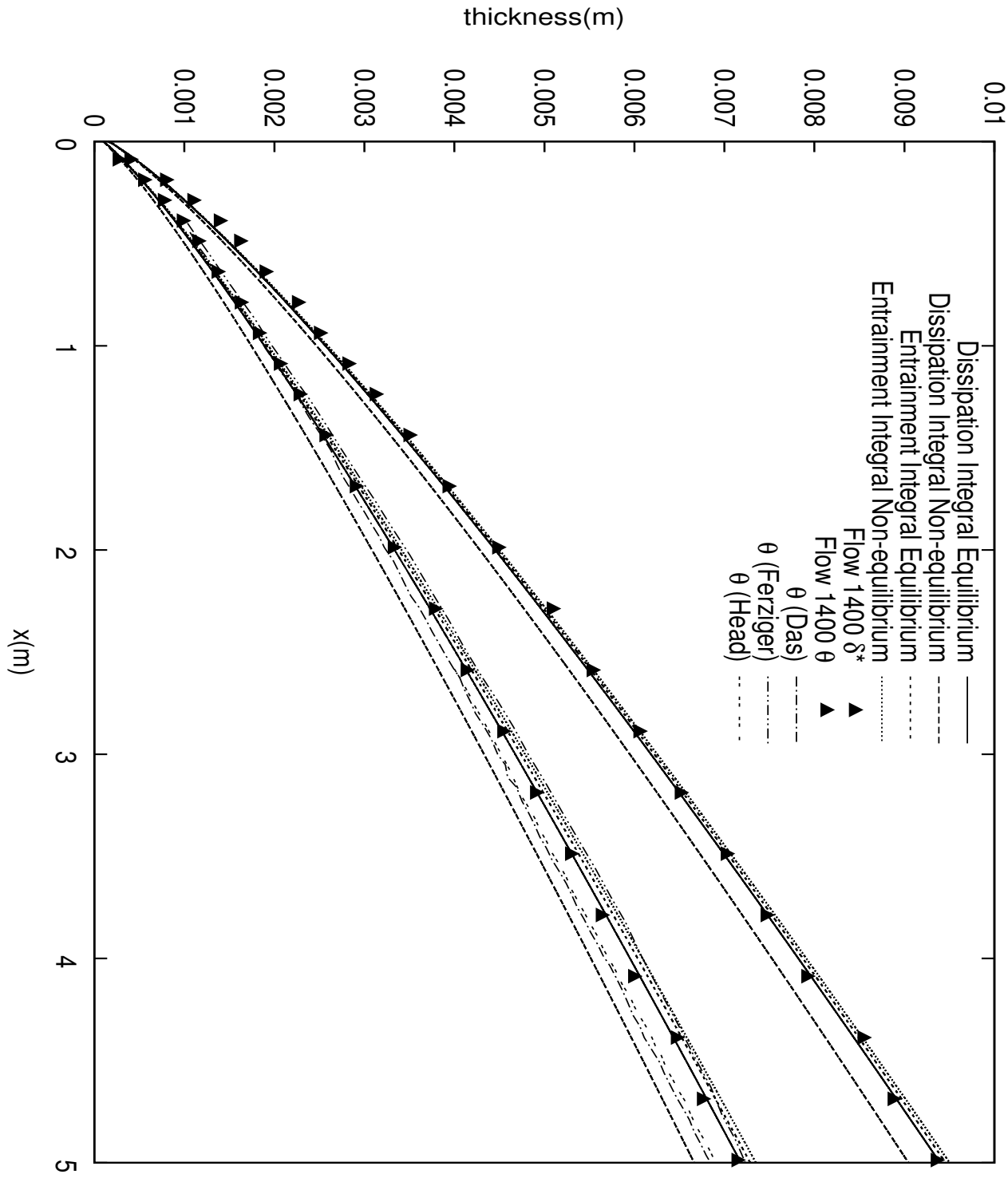

Figure B-4: Unsteady simulation of the Flow 1400 (momentum thickness and displacement thickness).

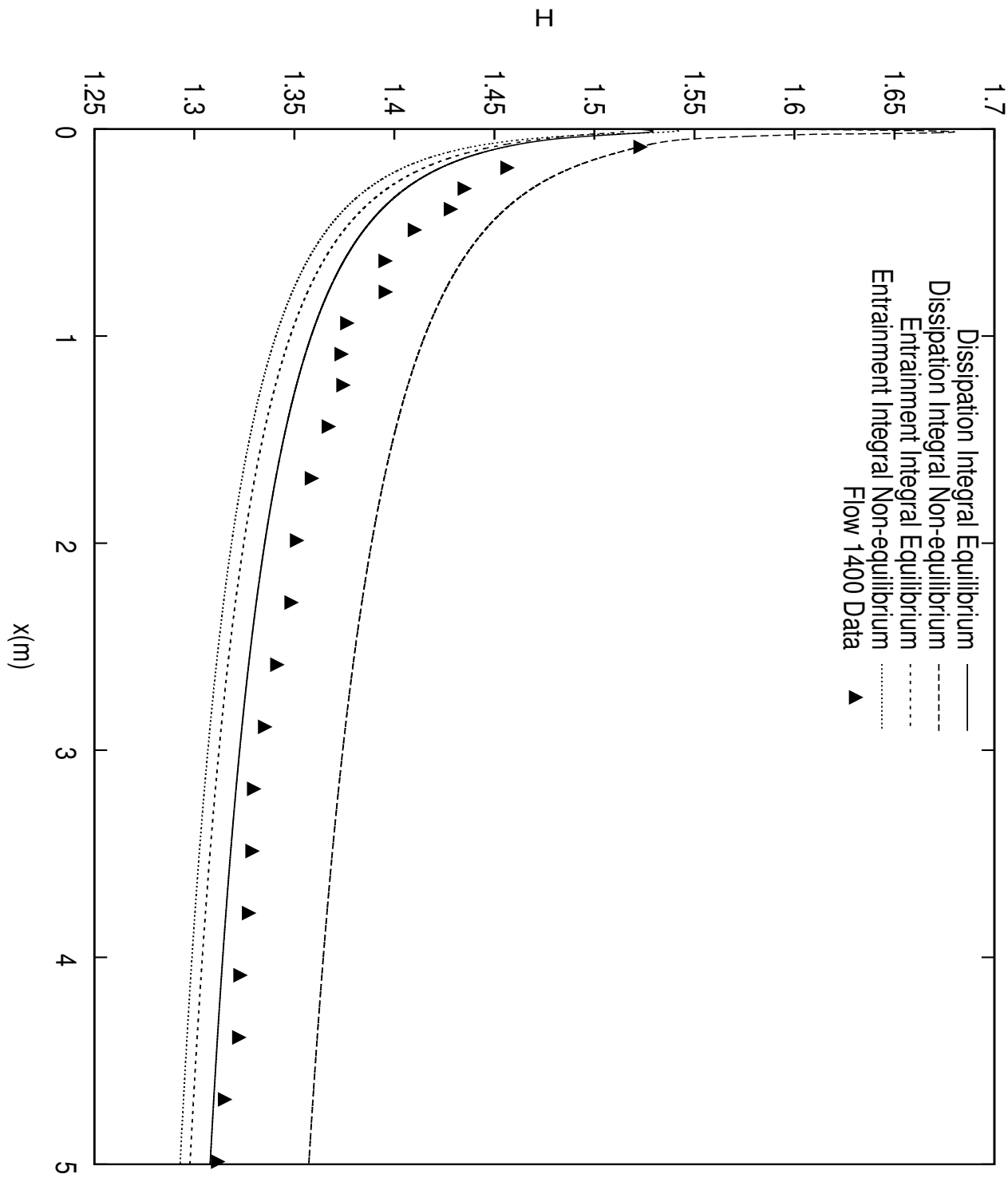

Figure B-5: Unsteady simulation of the Flow 1400 (shape factor).

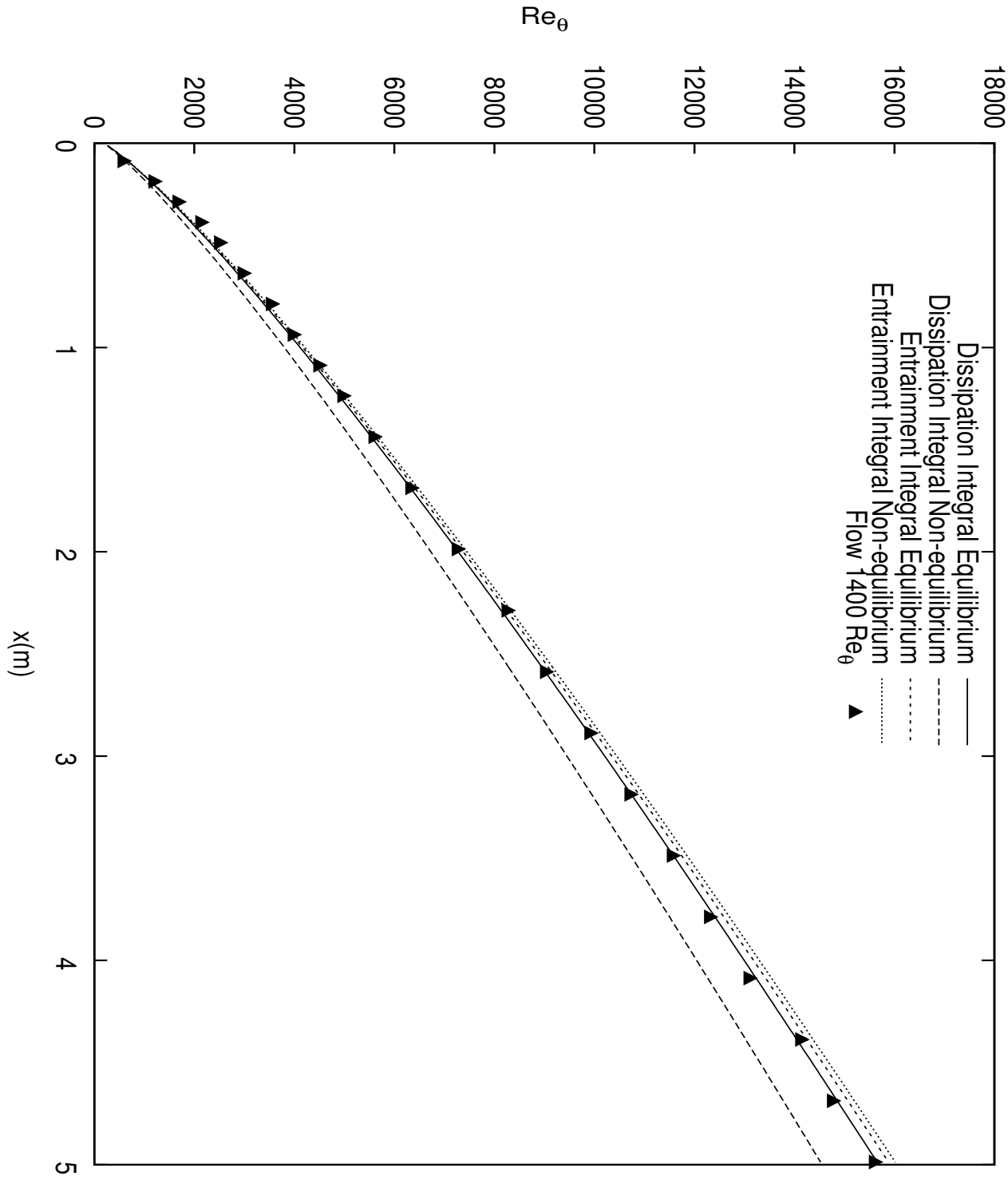

Figure B-6: Unsteady simulation of the Flow 1400 (momentum thickness Reynolds number).

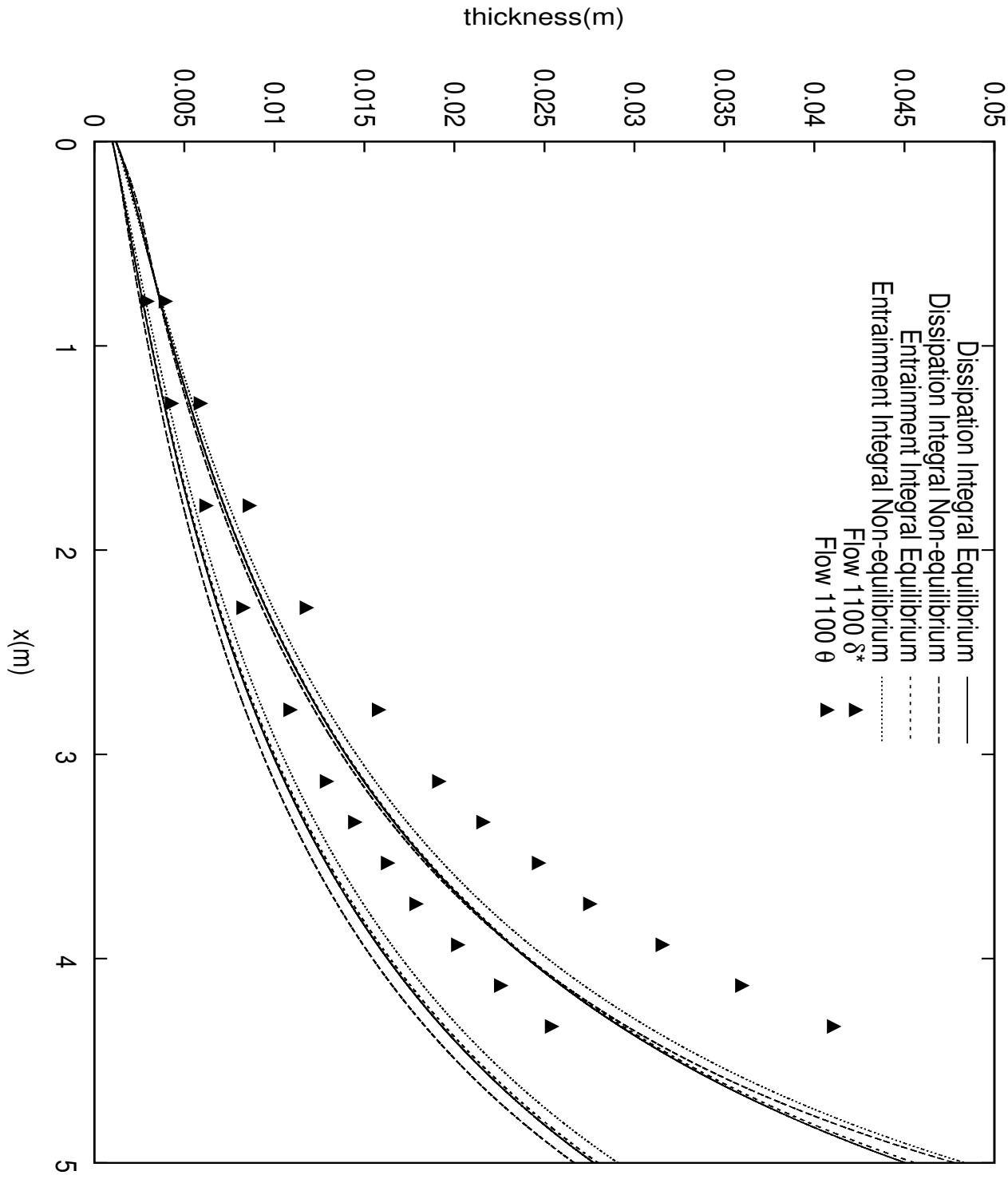

Figure B-7: Steady simulation of the Flow 1100 (momentum thickness and displacement thickness).

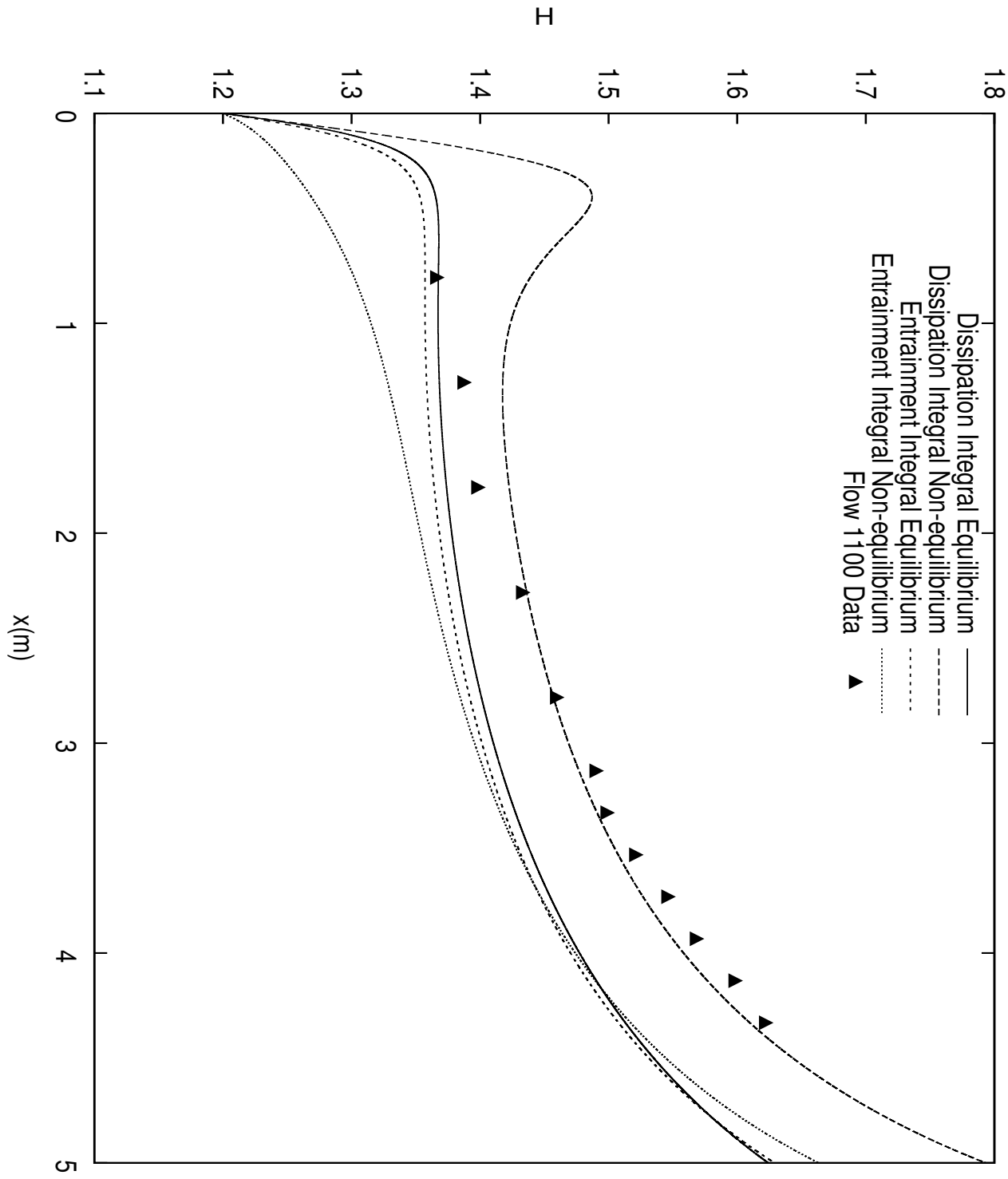

Figure B-8: Steady simulation of the Flow 1100 (shape factor).

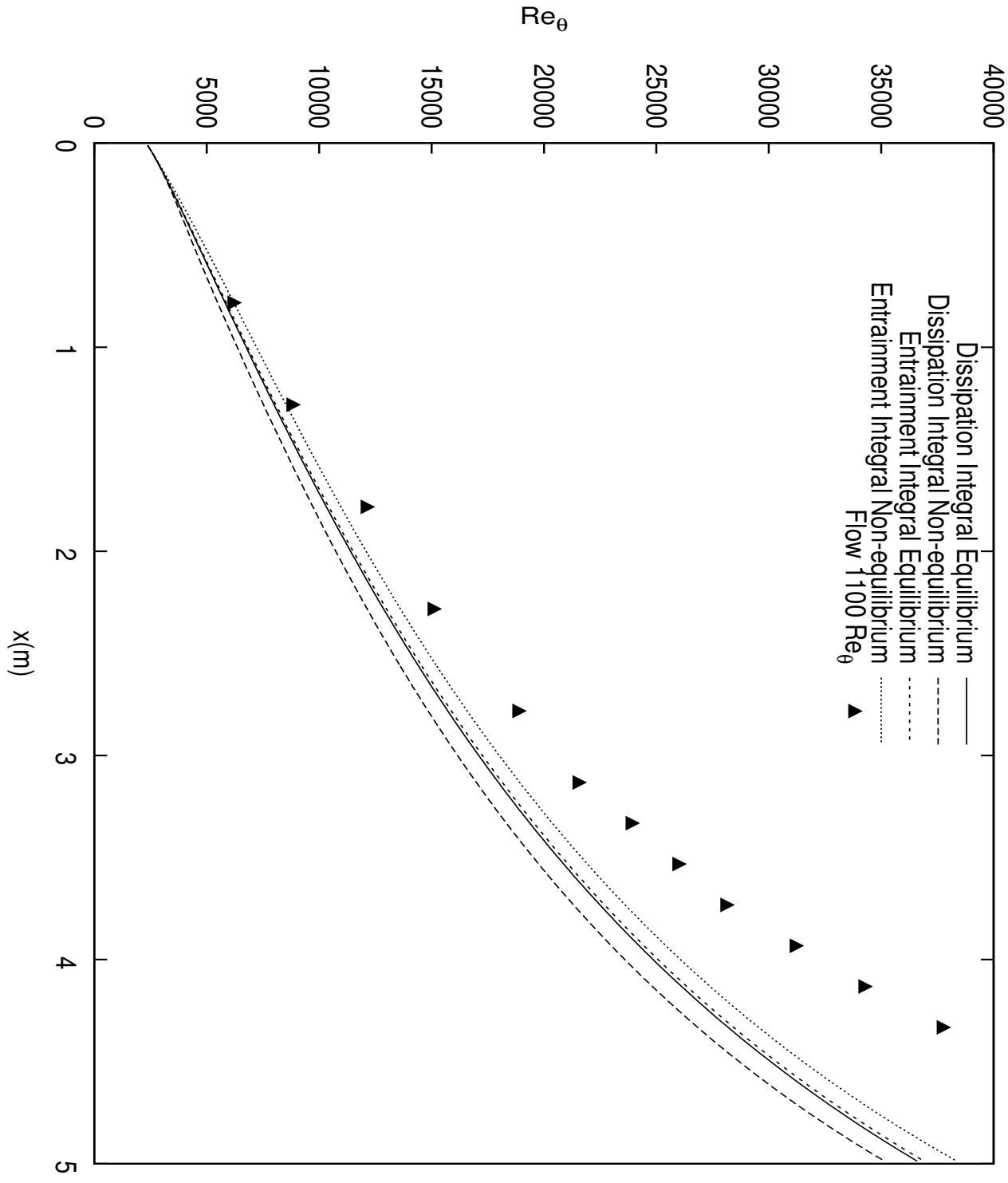

Figure B-9: Steady simulation of the Flow 1100 (momentum thickness Reynolds number).

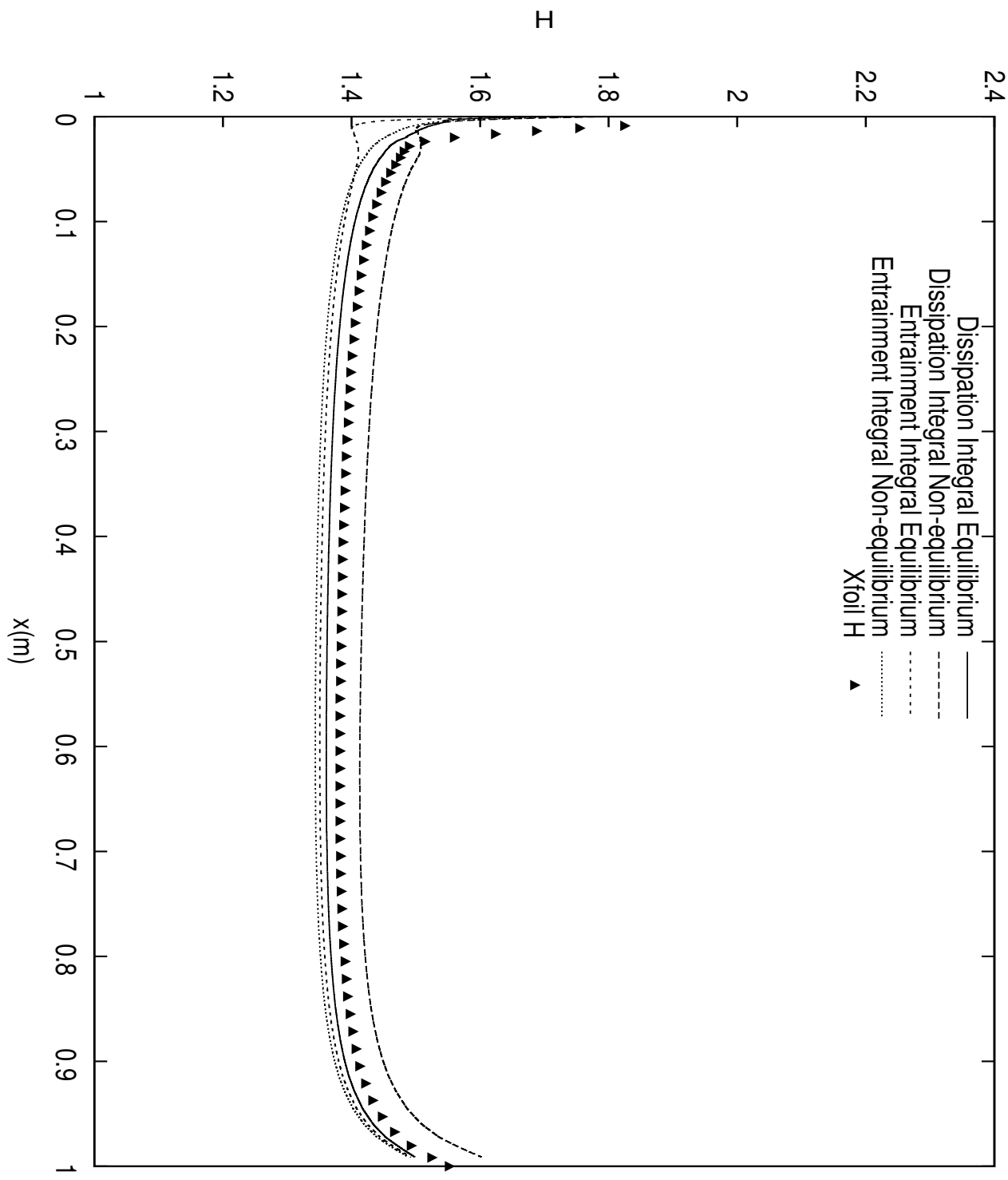

Figure B-10: Steady simulation of the NACA 0012 $\alpha = 0°$ (shape factor).

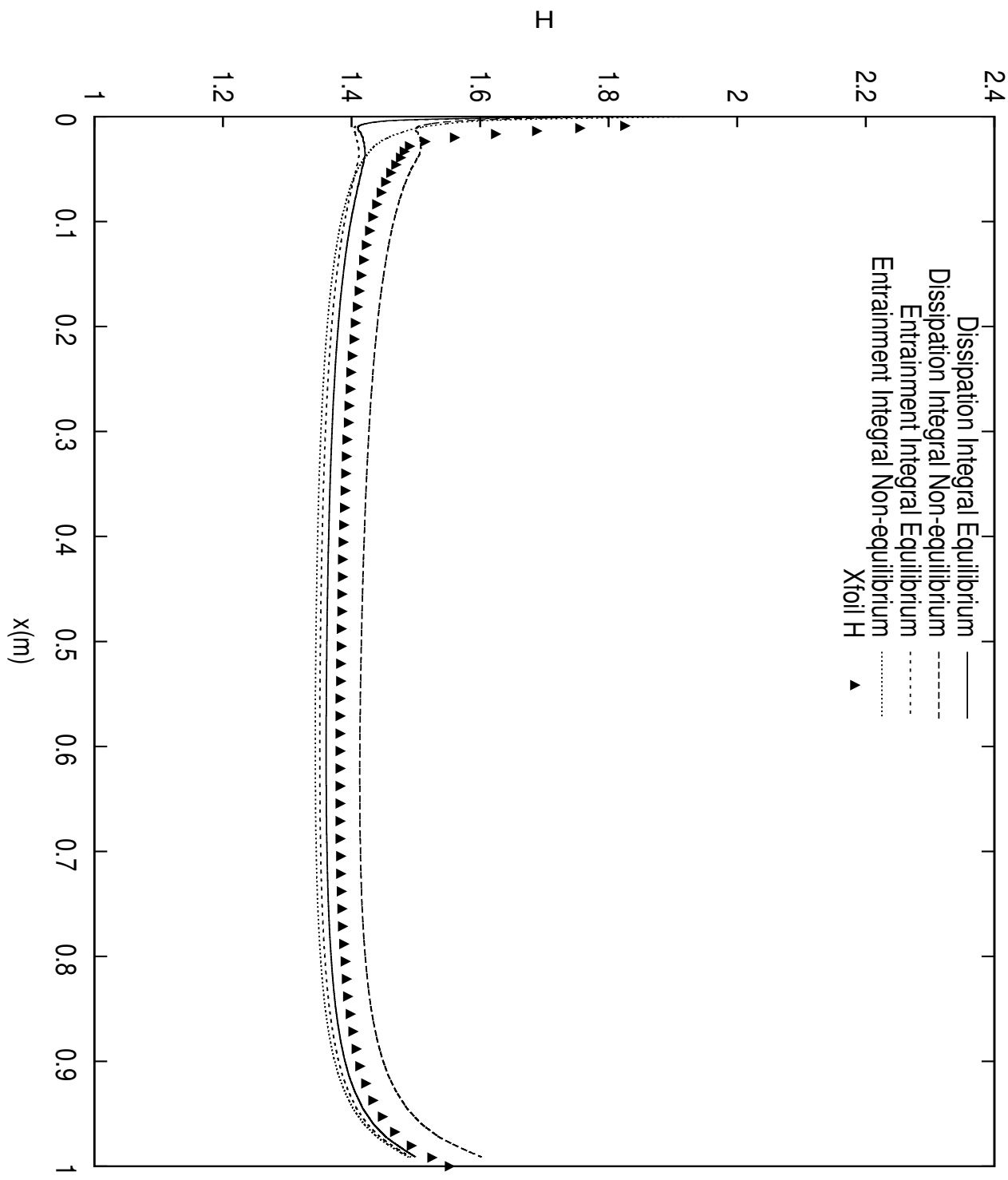

Figure B-11: Unsteady simulation of the NACA 0012 $\alpha = 0°$ (shape factor).

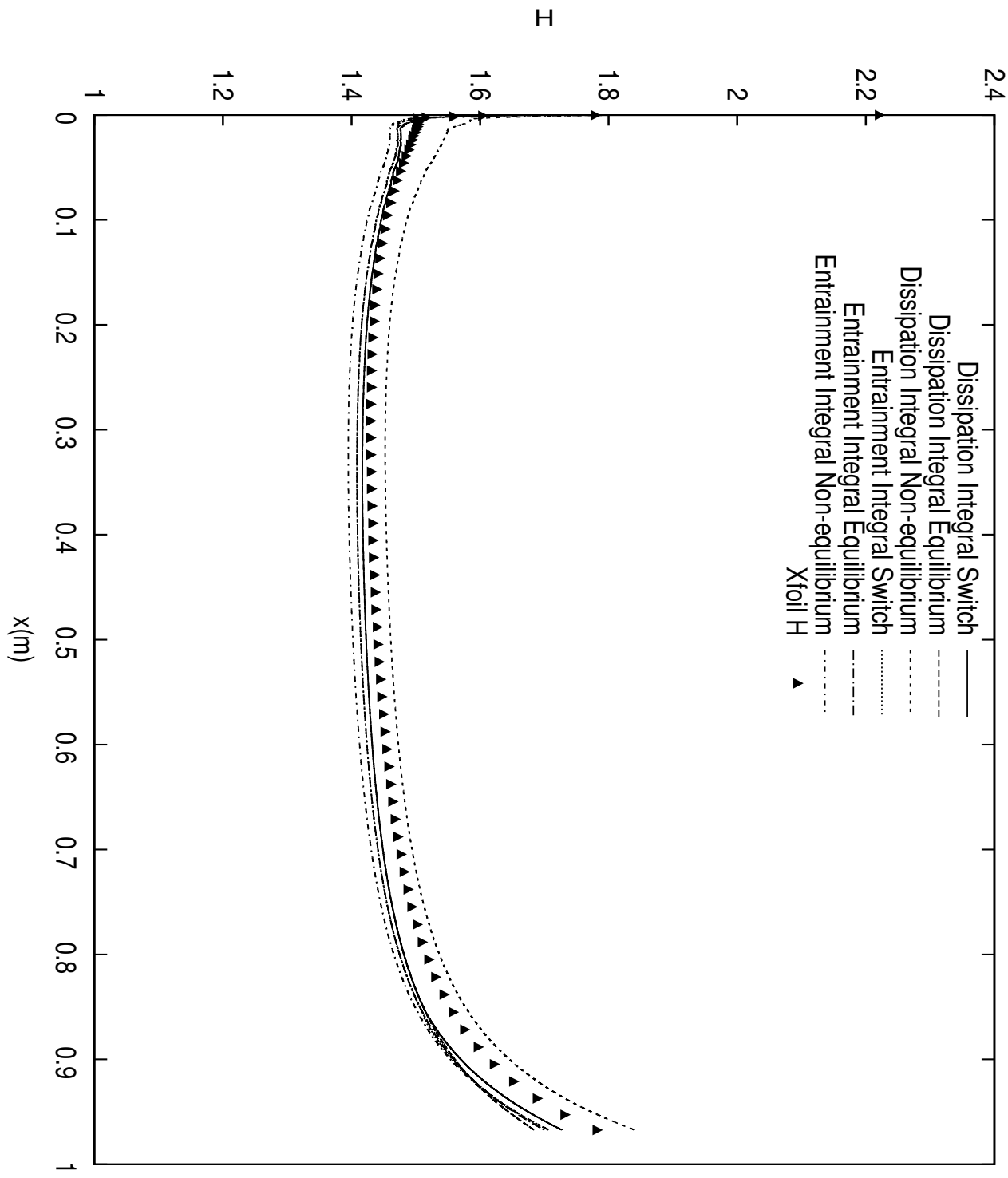

Figure B-12: Steady simulation of the NACA 0012 $\alpha = 10°$ (shape factor).

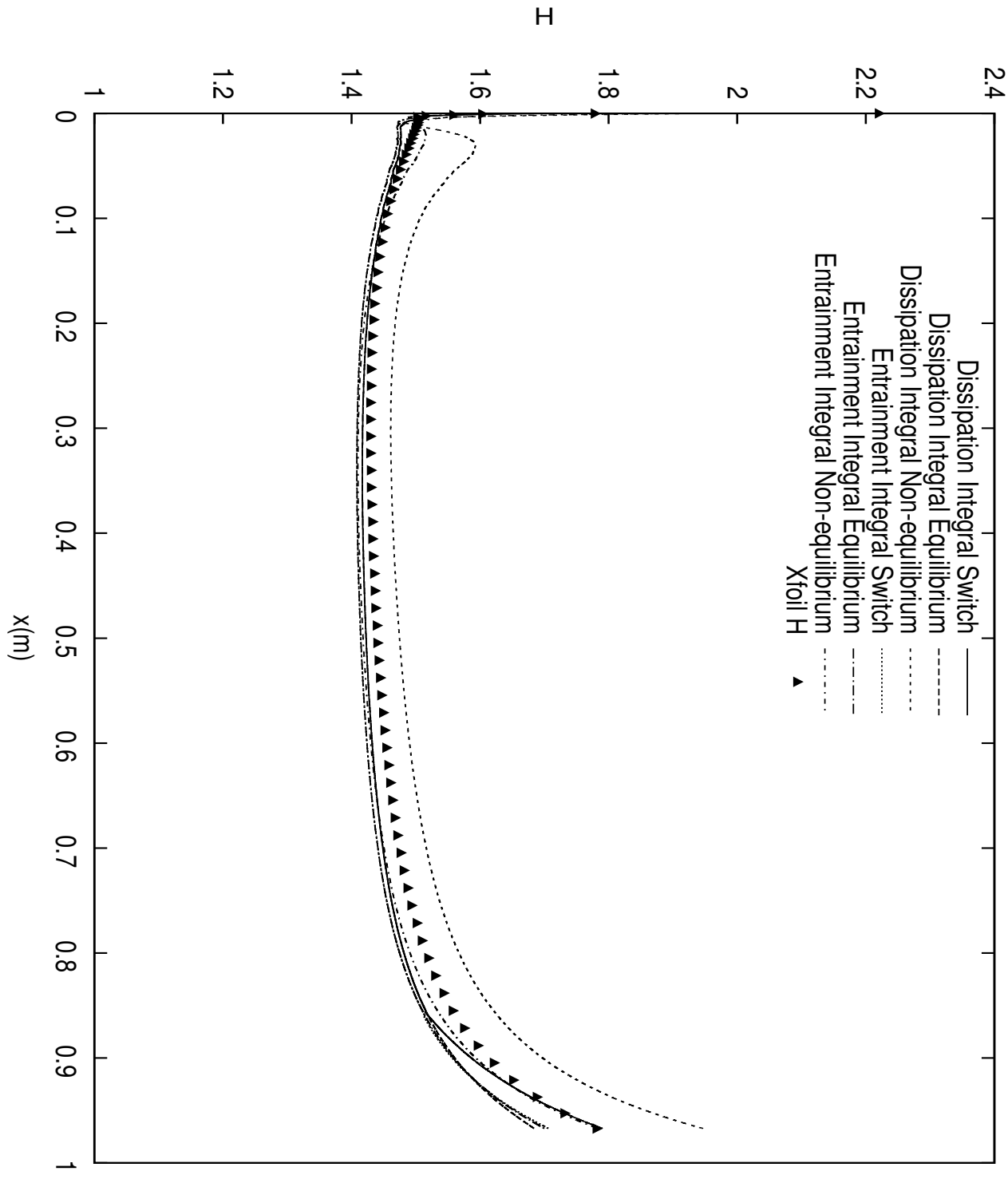

Figure B-13: Unsteady simulation of the NACA 0012 $\alpha = 10°$ (shape factor).

B.2 Results of transitional boundary layers

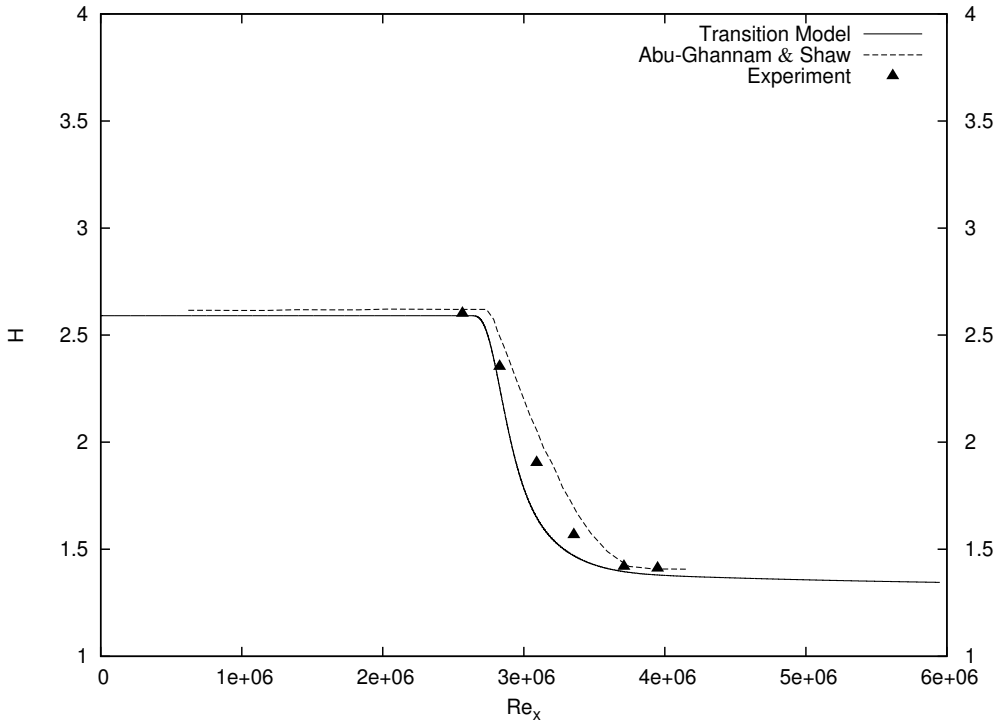

Figure B-14: Steady simulation of Schubauer and Klebanoff's flat plate (shape factor).

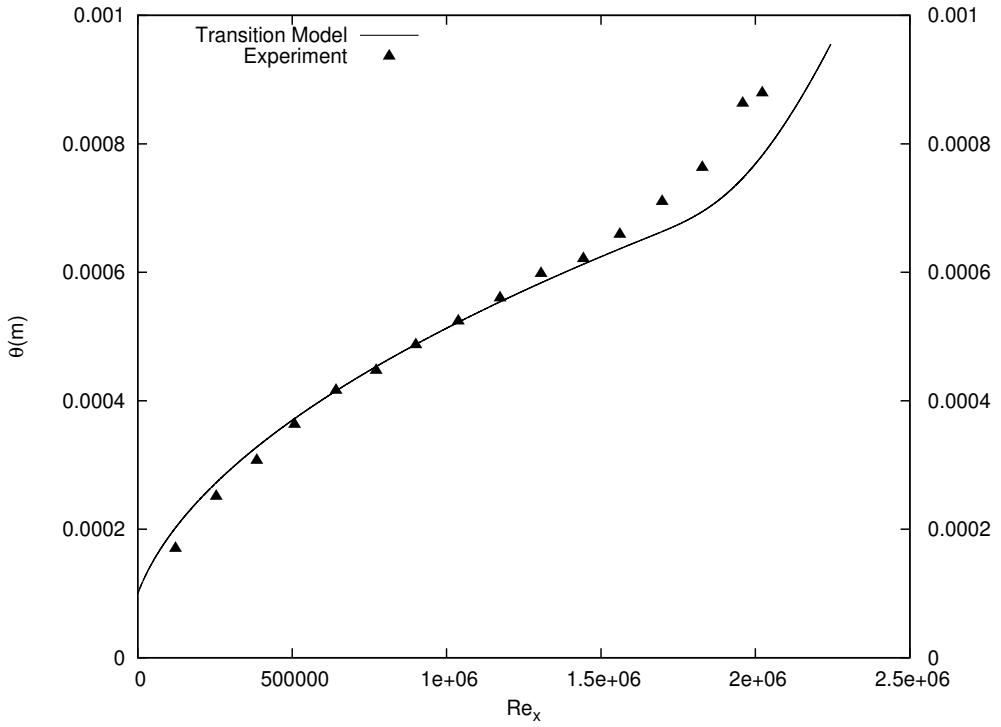

(a) Momentum and displacement thickness

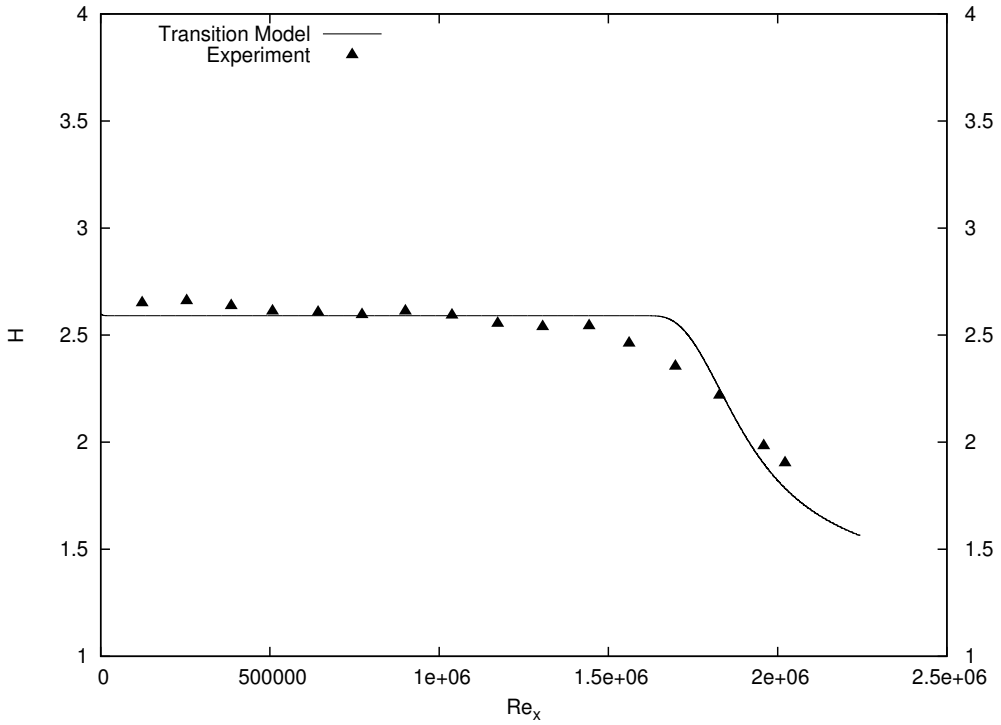

(b) Shape factor

Figure B-15: Steady simulation of T3A-.

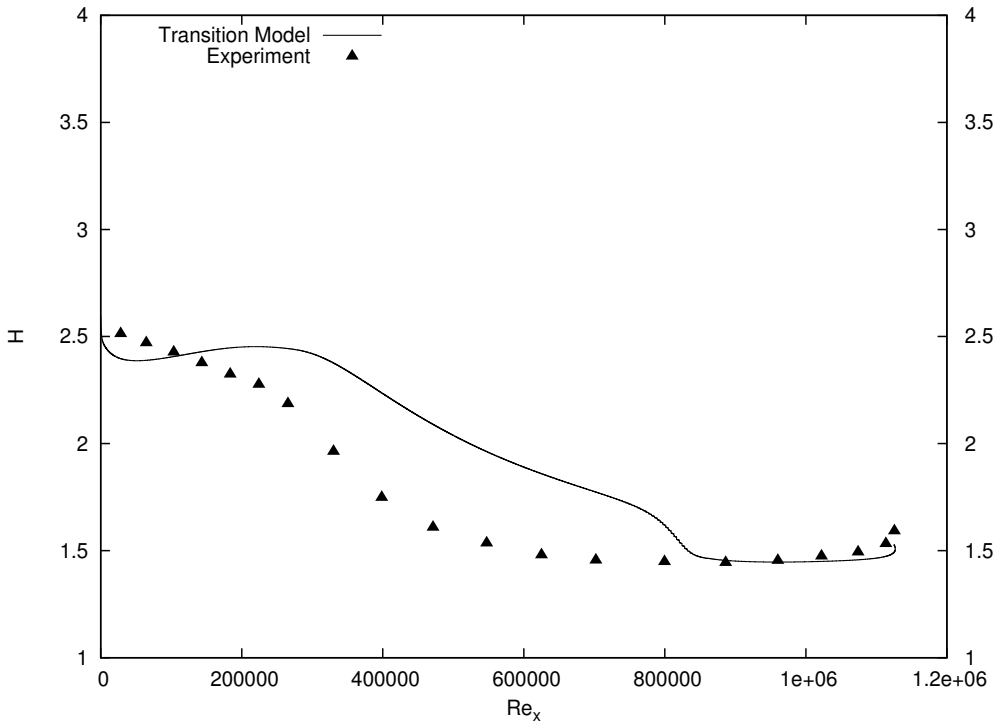

Figure B-16: Steady simulation of T3C5 (shape factor) (without modification).

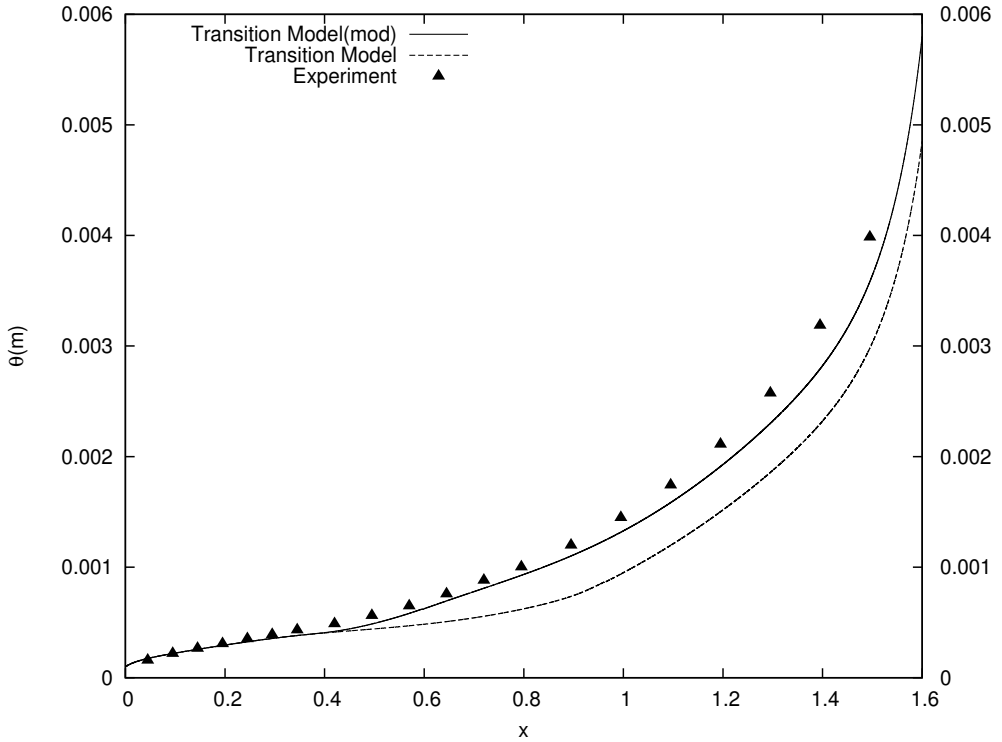

Figure B-17: Steady simulation of T3C5 (momentum thickness) (with modification).

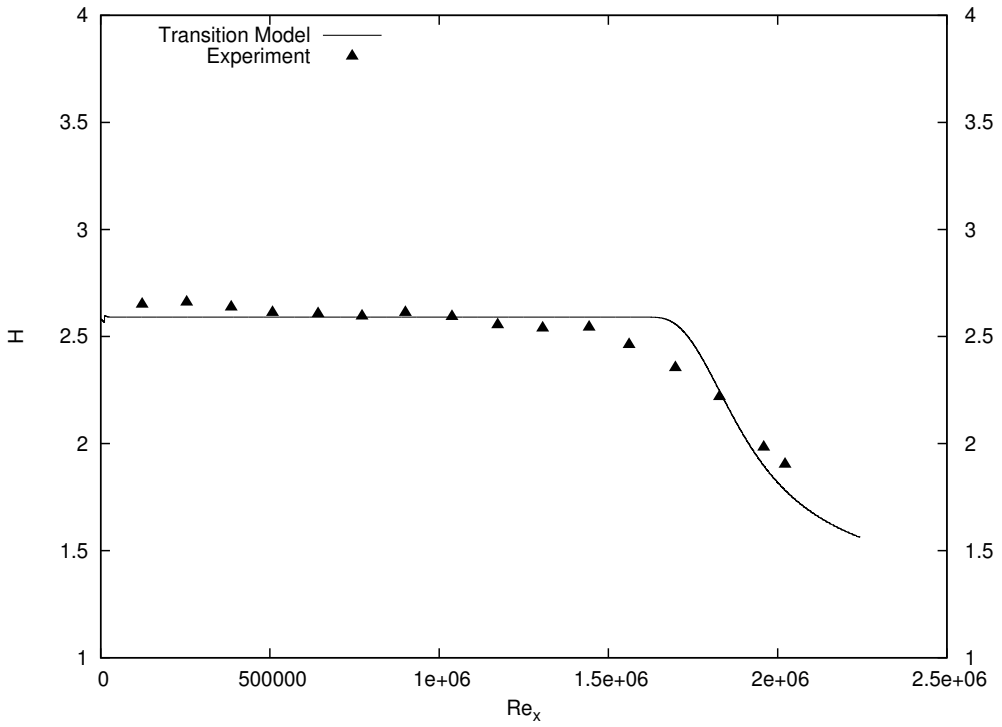

Figure B-18: Unsteady simulation of T3A- (shape factor).

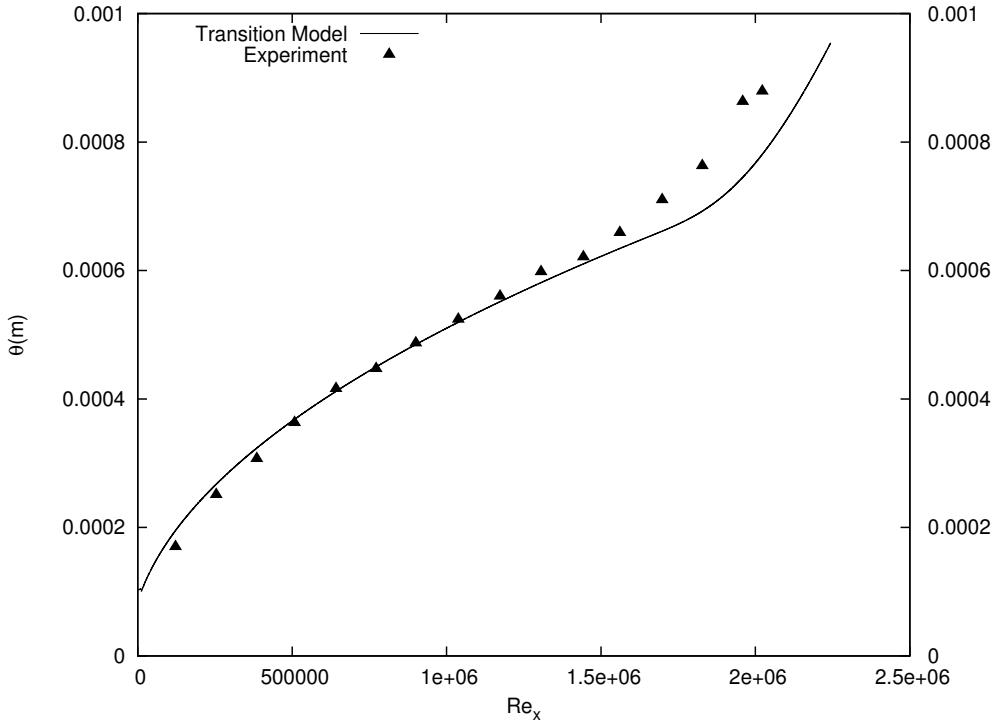

Figure B-19: Unsteady simulation of T3A- (momentum thickness).

Bibliography

[1] Flat plate transitional boundary layers. http://cfd.mace.manchester.ac.uk/cgi-bin/cfddb/prpage.cgi?20&EXP&database/cases/case20/Case_data&database/cases/case20&cas20_head.html&cas20_desc.html&cas20_meth.html&cas20_data.html&cas20_refs.html&cas20_rsol.html&1&1&1&1&1&unknown.

[2] B.J. Abu-Ghannam and R. Shaw. Natural transition of boundary layersthe effects of turbulence, pressure gradient, and flow history. *Journal of Mechanical Engineering Science*, 22(5):213–228, 1980.

[3] Harold L Atkins and Chi-Wang Shu. Quadrature-free implementation of discontinuous galerkin method for hyperbolic equations. *AIAA journal*, 36(5):775–782, 1998.

[4] A.V. Boiko, K.J.A. Westin, B.G.B. Klingmann, V.V. Kozlov, and P.H. Alfredsson. Experiments in a boundary layer subjected to free stream turbulence. part 2. the role of ts-waves in the transition process. *Journal of Fluid Mechanics*, 281:219–245, 1994.

[5] J. Bongers. Implementation of a new transition prediction method in xfoil. Master's thesis, Delft University of Technology, 2006.

[6] P. Bradshaw, D.H. Ferriss, and N.P. Atwell. Calculation of boundary-layer development using the turbulent energy equation. *Journal of Fluid Mechanics*, 28(03):593–616, 1967.

[7] W.L. Chen, F.S. Lien, and M.A. Leschziner. Non-linear eddy-viscosity modelling of transitional boundary layers pertinent to turbomachine aerodynamics. *International journal of heat and fluid flow*, 19(4):297–306, 1998.

[8] D.E. Coles. *Turbulent Boundary Layers in Pressure Gradients: A Survey Lecture Prepared for the 1968 AFOSR-IFP-Stanford Conference on Computation of Turbulent Boundary Layers*. 1969.

[9] D.K. Das. A simple theory for calculating turbulent boundary layers under arbitrary pressure gradients. *International Journal of Engineering and Fluid Mechanics Spring*, 1:83–99, 1988.

[10] S. Dhawan and R. Narasimha. Some properties of boundary layer flow during the transition from laminar to turbulent motion. *Journal of Fluid Mechanics*, 3:418–436, 1 1958.

[11] M. Drela. *Two-dimensional Transonic Aerodynamic Design and Analysis Using the Euler Equations*. GTL report. Gas Turbine Laboratory, Massachusetts Institute of Technology, 1986.

[12] M. Drela. Xfoil: An analysis and design system for low reynolds number airfoils. In *Low Reynolds number aerodynamics*, pages 1–12. Springer, 1989.

[13] M. Drela. Mises implementation of modified abu-ghannam/shaw transition criterion. *MISES Code Documentation, MIT*, 1998.

[14] M. Drela. Three-dimensional integral boundary layer formulation for general configurations. In *21st AIAA Computational Fluid Dynamics Conference*. American Institute of Aeronautics and Astronautics, 2013.

[15] H.W. Emmons. The laminar-turbulent transition in a boundary layer-part i. *Journal of the Aeronautical Sciences (Institute of the Aeronautical Sciences)*, 18(7), 2012.

[16] C.C. Fenno, H.A. Hassan, and P.A. Newman. Unsteady viscous-inviscid interaction procedures for transonic airfoils using cartesian grids. *Journal of Aircraft*, 26(8):723–730, 1989.

[17] J.H. Ferziger, A.A. Lyrio, and J.G. Bardina. New skin friction and entrainment correlations for turbulent boundary layers. *Journal of Fluids Engineering*, 104(4):537–540, 1982.

[18] M. Gaster. A note on the relation between temporally-increasing and spatially-increasing disturbances in hydrodynamic stability. *Journal of Fluid Mechanics*, 14(02):222–224, 1962.

[19] P. Goldberg. Upstream history and apparent stress in turbulent boundary layers. Technical report, DTIC Document, 1966.

[20] S. Goldstein. On laminar boundary-layer flow near a position of separation. *The Quarterly Journal of Mechanics and Applied Mathematics*, 1(1):43–69, 1948.

[21] J.P. Gostelow, N. Melwani, and G.J. Walker. Effects of streamwise pressure gradient on turbulent spot development. *Journal of turbomachinery*, 118(4):737–743, 1996.

[22] J.E. Green, D.J. Weeks, and J.W.F. Brooman. *Prediction of turbulent boundary layers and wakes in compressible flow by a lag-entrainment method*. 1973.

[23] F. Haciahmetoglu. Investigation of unsteady viscous-inviscid interaction schemes. Master's thesis, Delft University of Technology and Energy Research Centre of the Netherlands, 2013.

[24] M.R. Head. Entrainment in the turbulent boundary layer. Technical report, DTIC Document, 1958.

[25] C.C. Heister, A. Klein, and E. Krämer. Rans-based laminar-turbulent transition prediction for airfoil and rotary wing applications using semi-empirical criteria. In *New Results in Numerical and Experimental Fluid Mechanics VIII*, pages 313–320. Springer, 2013.

[26] M.W. Johnson and A.H. Ercan. A physical model for bypass transition. *International journal of heat and fluid flow*, 20(2):95–104, 1999.

[27] R. Jordinson. The flat plate boundary layer. part 1. numerical integration of the orr—sommerfeld equation. *Journal of Fluid Mechanics*, 43(04):801–811, 1970.

[28] A. Krumbein, N. Krimmelbein, and C. Seyfert. Automatic transition prediction in unsteady airfoil flows using an unstructured cfd code. *AIAA Paper*, 3365:2011, 2011.

[29] E. Kulunk. Aerodynamics of wind turbines. *Fundamental and Advanced Topics in Wind Power*, 1970.

[30] R.B. Langtry. A correlation-based transition model using local variables for unstructured parallelized cfd codes. 2006.

[31] S. Lardeau, N. Li, and M.A. Leschziner. Large eddy simulation of transitional boundary layers at high free-stream turbulence intensity and implications for rans modeling. *Journal of turbomachinery*, 129(2):311–317, 2007.

[32] H. Ludwieg and W. Tillmann. Untersuchungen über die wandschubspannung in turbulenten reibungsschichten. *Archive of Applied Mechanics*, 17(4):288–299, 1949.

[33] B.A. Nishida. *Fully simultaneous coupling of the full potential equation and the integral boundary layer equations in three dimensions*. PhD thesis, Massachusetts Institute of Technology, 1996.

[34] H.J. Obremski and A.A. Fejer. Transition in oscillating boundary layer flows. *Journal of Fluid Mechanics*, 29(01):93–111, 1967.

[35] S.A. Orszag. Accurate solution of the orr–sommerfeld stability equation. *Journal of Fluid Mechanics*, 50(04):689–703, 1971.

[36] H. Özdemir. Derivation of 2d unsteady integral boundary layer equations in strong interaction. Technical report, Technical Report ECN-X-10-107, ECN.

[37] H. Özdemir. *High-order discontinuous Galerkin method on hexahedral elements for aeroacoustics*. University of Twente, 2006.

[38] H. Özdemir. Development of a discontinuous galerkin method for the unsteady integral boundary layer equations. 2010.

[39] T.J. Praisner and J.P. Clark. Predicting transition in turbomachinery-part i: A review and new model development. *Journal of Turbomachinery*, 129(1):1–13, 2007.

[40] H. Schlichting and K. Gersten. *Boundary Layer Theory*. Springer, 8th edition, 2000.

[41] G.B. Schubauer and P.S. Klebanoff. Contributions on the mechanics of boundary-layer transition. 1956.

[42] G.B. Schubauer and H.K. Skramstad. Laminar-boundary-layer oscillations and transition on a flat plate. 1948.

[43] H. Seubers. Path-consistent schemes for interacting boundary - a discontinuous galerkin approach. Master's thesis, Delft University of Technology and Energy Research Centre of the Netherlands, 2014.

[44] A.M.O. Smith and N. Gamberoni. *Transition, pressure gradient and stability theory*. Douglas Aircraft Company, El Segundo Division, 1956.

[45] W.J. Solomon, J.P. Gostelow, and G.J. Walker. Transition length prediction for flows with rapidly changing pressure gradients. *Journal of turbomachinery*, 118(4):744–751, 1996.

[46] Y.B. Suzen and P.G. Huang. Modeling of flow transition using an intermittency transport equation. *Journal of fluids engineering*, 122(2):273–284, 2000.

[47] J.L. Thomas. Integral boundary-layer models for turbulent separated flows. In *17th Fluid Dynamics, Plasma Dynamics, and Lasers Conference*, volume 1, 1984.

[48] E.F. van den Boogaard. High-order discontinuous galerkin method for unsteady integral boundary layer equations. Master's thesis, Delft University of Technology and Energy Research Centre of the Netherlands, 2010.

[49] B. van Es. Copmarison and application of unsteady integral boundary layer methods, using various mumerical schemes. Master's thesis, Delft University of Technology and Energy Research Centre of the Netherlands, 2009.

[50] A. van Garrel. Development of a wind turbine aerodynamics simulation module. Technical report, Technical Report ECN-C-03-079, ECN, 2003.

[51] A. van Garrel. Development of a wind turbine rotor flow panel method. Technical report, Technical Report ECN-E11-071, ECN, 2011.

[52] J.L. van Ingen. *Theoretical and Experimental Investigations of Incompressible Laminar Boundary Layers with and Without Suction*. 1965.

[53] J.L. van Ingen. A new e^N database method for transition prediction. Technical report, Delft University of Technology, 2006.

[54] J.L. van Ingen. The e^N method for transition prediction. historical review of work at tu delft. *AIAA paper*, 3830:2008, 2008.

[55] D. K. Walters and J.H. Leylek. A new model for boundary-layer transition using a single-point rans approach. In *ASME 2002 International Mechanical Engineering Congress and Exposition*, pages 67–79. American Society of Mechanical Engineers, 2002.

[56] D.K. Walters and D. Cokljat. A three-equation eddy-viscosity model for reynolds-averaged navier–stokes simulations of transitional flow. *Journal of fluids engineering*, 130(12):121401, 2008.

[57] F.M. White. *Viscous fluid flow*. McGraw Hill Series in Mechanical Engineering. McGraw-Hill Professional Publishing, 1991.

[58] K. Wieghardt and W. Tillmann. *On the Turbulent Friction Layer for Rising Pressure*. Technical memorandum. National Advisory Commitee for Aeronautics, 1951.

[59] J. Windte, R. Radespiel, U. Scholz, and B. Eisfeld. Rans simulation of the transitional flow around airfoils at low reynolds numbers for steady and unsteady onset conditions. Technical report, DTIC Document, 2004.

[60] X. Wu and P. Moin. Direct numerical simulation of turbulence in a nominally zero-pressure-gradient flat-plate boundary layer. *Journal of Fluid Mechanics*, 630:5–41, 2009.

[61] B. Ye. Investigation of unsteady transition methods. Technical report, Delft University of Technology and Energy Research Centre of the Netherlands, 2014.